



저작자표시-비영리-변경금지 2.0 대한민국

이용자는 아래의 조건을 따르는 경우에 한하여 자유롭게

- 이 저작물을 복제, 배포, 전송, 전시, 공연 및 방송할 수 있습니다.

다음과 같은 조건을 따라야 합니다:



저작자표시. 귀하는 원저작자를 표시하여야 합니다.



비영리. 귀하는 이 저작물을 영리 목적으로 이용할 수 없습니다.



변경금지. 귀하는 이 저작물을 개작, 변형 또는 가공할 수 없습니다.

- 귀하는, 이 저작물의 재이용이나 배포의 경우, 이 저작물에 적용된 이용허락조건을 명확하게 나타내어야 합니다.
- 저작권자로부터 별도의 허가를 받으면 이러한 조건들은 적용되지 않습니다.

저작권법에 따른 이용자의 권리는 위의 내용에 의하여 영향을 받지 않습니다.

이것은 [이용허락규약\(Legal Code\)](#)을 이해하기 쉽게 요약한 것입니다.

[Disclaimer](#)

공학박사학위논문

실리콘 치환 도핑이
그래핀의 열물성에 미치는 영향

Effect of Substitutional Silicon Dopants
on Thermal Properties of Graphene

2018 년 8 월

서울대학교 대학원

기계항공공학부

이 우 림

Effect of Substitutional Silicon Dopants on Thermal Properties of Graphene

Woorim Lee
Mechanical Engineering
School of Mechanical and Aerospace Engineering
Seoul National University

Abstract

One-atom-thick layer graphene has superlative thermal conductivity $k = 2000 \sim 5000 \text{ W/mK}$ but it is significantly suppressed by the presence of lattice defects. Among the different types of lattice defects, substitutional defects efficiently reduce the in-plane thermal conductivity but maintain the unique hexagonal structures of graphene, which possibly enables to preserve other novel properties like high electrical mobility and optical transparency. According to the second-order perturbation theory, the phonon scattering rate by the substitutional dopants is known to be proportional to the square of the mass different with the host C atoms (ΔM). Previous studies have only demonstrated the thermal conductivity reduction of graphene by the

substitutional dopants of small mass difference, including N, ^{13}C , B, and ^{24}C . In addition, they mostly facilitated the case of small mass perturbation and thermally and atomically isolated suspended graphene. The heavy dopants of larger mass difference will possibly provide more interesting and significant thermal properties alteration in graphene, including by over one order-of-magnitude further reduction in k .

In this point, the selection of our experimental investigation on the thermal properties alteration by substitutional dopants is the silicon atoms, which provides the largest mass difference compared to previous works, in our knowledge. We have successfully synthesized Si-doped graphene (SiG) by using liquid precursor and facilitating the low pressure chemical vapor deposition (LPCVD) synthesis, which suppresses the lattice defects in synthesized graphene samples and thus allows the exclusive understandings on the effects of Si dopants. In addition, the Si doping concentrations indicated by I(D)/I(G) Raman peak ratio are controlled by manipulating the synthesis temperature and pressure. Correlation between the I(D)/I(G) and Si doping concentration enables to measure the in-plane thermal conductivities with the Si doping concentration variation.

The in-plane thermal conductivity (k_{SiG}) of the supported SiG was probed using optothermal Raman thermometry after being transferred on an ultra-thin 8 nm SiO_2 substrate. The measurement results show that k_{SiG}

gradually decreases with the increase of Si dopant mass concentration from 1.41 % to 3.13 %, exhibiting more than one order-of-magnitude reduction from the supported pristine graphene of $k = 645.6 \sim 900.2$ W/m·K down to $k_{SiG} = 46.7 \sim 79.5$ W/m·K for the present supported SiG. When compared to the suspended pristine graphene (PG) case ($k = 2662.5$ W/m·K), the reduction is accounted for being nearly two order-of-magnitudes. We attribute the observed substantial reduction of k_{SiG} to the exceptionally large phonon scattering strength of Si dopants, which can be explained by the large mass difference between the doped Si atoms and the C atoms. We have also found that enhancing graphene-substrate conformity through thermal annealing in vacuum further lowers k_{SiG} from that of the ambient annealing case, due to the increasing phonon scattering rate by underlying substrate. Further aspects in our findings include reduced temperature dependence of k_{SiG} and negligibly small non-equilibrium effect in Si-doped graphene, both of which are believed to attribute to the enhanced phonon scattering (reduced phonon mean free path) by Si dopants as well as by the presence of the graphene-substrate interface.

Finally, we found that substitutional silicon dopants do not violently destruct the electrical properties of graphene when compared to previously measured thermal conductivities. The measured thermal conductivities show

the maximum 8 times further reduction than that of electrical conductivities at about 2.6 % Si doping concentration. This results can be attributable to the resemblance of silicon and carbon atoms in terms of their number of valence electrons. We note that substitutional doping of graphene with heavy Si atoms can be a novel strategy to independently control the thermal properties and thus possibly enhance the thermoelectric efficiency of graphene.

Keyword : Graphene, Supported Graphene, Doped Graphene, Si-doped Graphene, Thermal Conductivity, Optothermal Raman Thermometry, Electrical conductivity, Electrical mobility, Thermoelectric efficiency, Figure of merit, ZT

Student Number : 2016-33514

Contents

| | |
|--|-------------|
| Abstract | i |
| Contents | v |
| List of Figures | viii |
| List of Tables | xvi |
| | |
| Chapter 1. Introduction | 1 |
| 1.1. Background and motivation | 1 |
| 1.2. Objective of the study | 7 |
| | |
| Chapter 2. Synthesis of graphene..... | 13 |
| 2.1. Methods for graphene synthesis | 13 |
| 2.1.1. Pristine graphene | 13 |
| 2.1.2. Substitutionally doped graphene | 16 |
| 2.2. Synthesis of Si-doped graphene | 19 |
| 2.2.1. Review of previous studies..... | 19 |
| 2.2.2. Improvement of synthesis recipe..... | 21 |
| 2.3. Details in synthesis recipes..... | 23 |
| 2.3.1. Recipe for pristine graphene..... | 23 |
| 2.3.2. Recipe for Si-doped synthesis | 24 |
| 2.4. Si doping concentration & homogeneity control | 25 |
| 2.4.1. Doping concentration | 25 |
| 2.4.2. Doping homogeneity | 27 |
| 2.5. Sample characterization | 28 |
| 2.5.1. Raman spectroscopy..... | 28 |

| | |
|---|-----------|
| 2.5.2. X-Ray Photoemission Spectroscopy (XPS) | 29 |
| 2.5.3. Scanning Electron Microscopy (SEM) | 30 |
| 2.5.4. Grain size visualization | 30 |
| 2.6. Summary..... | 31 |
| Chapter 3. Thermal conductivity measurement | 46 |
| 3.1. Measurement scheme | 46 |
| 3.2. Sample preparation | 48 |
| 3.2.1. Why supported graphene? | 48 |
| 3.2.2. Graphene transfer | 49 |
| 3.2.3. Thermal annealing | 51 |
| 3.3. Thermal conductivity measurement | 53 |
| 3.3.1. Detailed procedure | 53 |
| 3.3.2. Temperature calibration result | 59 |
| 3.3.3. Temperature enhancement under heat flux..... | 60 |
| 3.4. Summary..... | 61 |
| Chapter 4. Thermal properties of Si-doped graphene | 75 |
| 4.1. Thermal conductivity reduction | 75 |
| 4.1.1. Si dopants concentration effect | 75 |
| 4.1.2. Graphene-substrate conformity effect..... | 81 |
| 4.1.3. Grain size effect..... | 83 |
| 4.1.4. Doping inhomogeneity effect..... | 84 |
| 4.2. Temperature independence of thermal conductivity | 86 |
| 4.2.1. Si dopants effect | 86 |
| 4.2.2. Graphene-substrate conformity effect..... | 87 |
| 4.3. Non-equilibrium errors in measurement data..... | 88 |

| | |
|---|------------|
| 4.3.1. Why non-equilibrium problems arises? | 88 |
| 4.3.2. Non-equilibrium error in Si-doped graphene | 92 |
| 4.4. Summary..... | 94 |
| Chapter 5. Thermoelectric properties of Si-doped graphene... | 112 |
| 5.1. Thermoelectric properties of graphene | 112 |
| 5.2. Electrical properties of Si-doped graphene | 116 |
| 5.3. Possibility of ZT enhancement..... | 122 |
| 5.4. Summary..... | 126 |
| Chapter 6. Summary and conclusion..... | 135 |
| Reference | 139 |
| Abstract in Korean | 154 |

List of Figures

Figure 1.1. Schematic descriptions on the defected graphene with vacancy, substitutional dopants, edge roughness, and grain boundary. All of the defects inherently reside in the graphene hexagonal lattices, which suppresses the transport characteristics of energy carriers.

Figure 1.2. Simple description on the principle of thermoelectricity, which indicates the induced thermoelectric voltage in response to the temperature gradient across the materials, and vice versa.

Figure 1.3. (a) Perfect hexagonal structure of pristine graphene, and (b) graphene with substitutional Si dopants of our interest.

Figure 1.4. A description for the Optothermal Raman thermometry to derive the in-plane thermal conductivity of Si-doped graphene as supported on extremely thin (8 nm) SiO₂ TEM grid. Note the significant phonon scattering induced by Si dopants.

Figure 2.1. Schematics for the synthesis of (a) Si-doped graphene (from Wang et al, 2015, *J. Mater. Chem. C*) and (b) pristine graphene (from Li et al, 2011, *ACS NANO*) using solid precursors. Both system require the heating tape to sublimate the solid precursors after the annealing process. In addition, the furnace can be contaminated by placed solid precursors during the ventilation.

Figure 2.2. (From Zhang et al, 2016, *Nanoscale*) XPS spectrums of Si-doped graphene samples synthesized by gas precursors (methane and silane). Samples with different doping concentration represent the inconsistent XPS spectra with unknown peak of more than 103 eV. This obstructs the exclusive study on the pure Si dopants effects.

Figure 2.3. Descriptions on the kinetics in (a) APCVD and (b) LPCVD near copper substrates. Non-uniform precursors distribution near catalytic copper substrate can be attributed to the mass-transport limited kinetics in APCVD. On the other hand, surface reaction limited kinetics in LPCVD can synthesize uniform graphene as long as the temperature of the substrate is uniformly maintained.

Figure 2.4. Si dopants concentration as functions of I(D)/I(G) Raman peak ratio for SiG samples with available synthesis methods using solid, liquid, and gas precursors. Lowered I(D)/I(G) with comparable Si doping concentration indicates the negligible defects in graphene lattices other than Si dopants.

Figure 2.5. (a) CVD systems for graphene synthesis. (b) Descriptions on the pristine graphene synthesis procedures with time and temperature variation. Two-step method enables to grow the large domain graphene.

Figure 2.6. (a) Modified CVD system to accommodate the liquid precursors for the Si-doped graphene synthesis. (b) Descriptions on the Si-doped graphene synthesis procedures with time and temperature variation.

Figure 2.7. I(D)/I(G) Raman peak ratio mapping for the Si-doped graphene samples with different pressure and temperature conditions. Note that decreasing temperature and increasing precursors pressure enhance the doping concentration and homogeneity.

Figure 2.8. Statistical distribution of I(D)/I(G) peak ratio obtained from the Raman mapping in Figure 2.7. for the precursor pressure of **(a)** 0.02 Torr, and **(b)** 0.08 Torr.

Figure 2.9. Distribution of G and 2D Raman peak position in Si-doped graphene synthesized with varied temperature at 0.08 Torr precursor pressure. More homogeneous distributions with lowered temperature indicates the homogenous Si doping distributions in Si-doped graphene. Randomly selected 50 positions data are represented.

Figure 2.10. **(a)** Representative Raman spectrum of pristine graphene and Si-doped graphene. Inset figure shows the deconvoluted spectra, which indicates the boundary-like defects (lattice distortion) of Si dopants. **(b)** XPS spectra of near Si binding energy for both pristine graphene and Si-doped graphene.

Figure 2.11. SEM image of **(a)** incompletely grown graphene and **(b)** fully-grown graphene. Some wrinkles in fully-grown graphene are observed.

Figure 2.12. Grain size visualization of synthesized pristine graphene and Si-doped graphene. MDA enables to optically observe the grain boundaries of graphene. Lowered synthesis temperature in Si-doped graphene can be attributable to the decreased grain size.

Figure 3.1. Description of the heat dissipation of incident heat flux for the (a) suspended graphene and (b) supported graphene. Additional out-of-plane conduction in supported graphene increases the ambiguity in exclusively deriving the in-plane conduction, which results in the increased measurement uncertainty.

Figure 3.2. Description of the heat dissipation of incident heat flux for the graphene supported onto (a) thick substrate and (b) thin substrate. Decreased out-of-plane conduction enhances the measurement reliability to derive the in-plane thermal conductivity of supported graphene.

Figure 3.3. Transfer procedure of CVD-synthesized graphene. Both pristine and Si-doped graphene samples were transferred onto 8-nm thin SiO₂ substrate by facilitating the described “PMMA-transfer method”.

Figure 3.4. Picture of loop for picking up the PMMA/graphene film during the transfer process. About the area of 1mm × 1mm graphene can be transferred.

Figure 3.5. Pictures of graphene as transferred onto SiO₂ TEM grid. Red arrows indicate the interfaces of graphene showing the mild optical contrast. Blue box represents the below zoomed-area, which describes well-transferred graphene with minimum wrinkles or chemical residues.

Figure 3.6. The schematic view of the “effective optical absorption” of supported graphene. Both direct absorption and indirect absorption from the reflected laser from underlying substrate are considered. The reduced optical

absorption can be attributable to the decreased optical conductivity by the Si dopants

Figure 3.7. Schematic description for the heat diffusion equation considering the optical absorption from incident heat flux, air convection, and conduction through the substrate.

Figure 3.8. Typical Raman spectrum of pristine graphene with different distinct peaks. Each peaks reflect the scattering of optical electrons with corresponding phonons, which enables to probe the temperature of different heat carriers.

Figure 3.9. Experimental results for the Raman peak shift calibration with the graphene temperature and $I(D)/I(G)$ variation, dw/dT . All of the results indicate that the slope of G peak calibration is lower than that of 2D peak, representing the temperature-sensitivity and measurement reliability of 2D peak calibration.

Figure 3.10. Experimental results for the graphene temperature vs. incident heat flux with the facilitation of 2D peak. Ambient-annealed samples and vacuum-annealed samples exhibit the different temperature with the same incident heat flux, indicating the dissimilar graphene-substrate conformity between samples.

Figure 3.11. Experimental results for the graphene temperature vs. incident heat flux with the facilitation of G peak. Similar difference between ambient-annealed samples and vacuum-annealed samples can be observed when

compared to 2D peak calibration results.

Figure 4.1. Thermal conductivities of SiG with the increase of I(D)/I(G) intensity ratio based on 2D peak calibration. More than 2% Si dopants concentration provides the order-of-magnitude reduction compared to supported pristine graphene.

Figure 4.2. Thermal conductivities of SiG with the increase of I(D)/I(G) intensity ratio based on G peak calibration. Similar order-of-magnitude reduction can be observed.

Figure 4.3. (From Y. Serov et al, 2013, *APL*) Theoretical predictions on thermal conductivity of supported graphene with the grain sizes (GB) and line defects (LD). The effects of grain boundaries on thermal conductivity reduction can be negligible when the grain sizes are longer than average phonon MFPs of supported graphene (~90 nm).

Figure 4.4. A schematic description of the thermal activation boundary (TAB). Dopants distribution within the TAB determines the possible uncertainties induced by doping inhomogeneity, attributing to the large temperature gradient inside the TAB. Yellow atoms indicate the Si dopants.

Figure 4.5. Estimated TAB size for the each measurement spots with different I(D)/I(G) ratio. Relatively uniform distribution of I(D)/I(G) (Si dopants) possibly ensures the negligible uncertainties from doping inhomogeneity.

Figure 4.6. Thermal conductivities of SiG with the I(D)/I(G) variation as a function of temperature, which indicates the negligible temperature dependence in Si-doped graphene.

Figure 4.7. (From Kim et al, 2017, *Carbon*) Thermal conductivities of pristine supported graphene with the increasing number of thermal annealing. Enhanced graphene-substrate conformity by thermal annealing in vacuum suppresses the long-wavelength phonons in graphene, reducing the temperature dependence.

Figure 4.8. Non-equilibrium error in Si-doped graphene with a function of I(D)/I(G) intensity ratio. Temperature discrepancy exhibits less than 6% of non-equilibrium error and gradually decreases with the increase of I(D)/I(G).

Figure 4.9. A schematic illustration for the non-equilibrium effects for PG and SiG. The effects decrease with the increase in Si doping concentrations, attributing to the reduced phonon MFPs and breakdown of reflection symmetry, both by the presence of Si dopant atoms.

Figure 4.10. Thermal conductivities of ambient-annealed SiG derived both by 2D peak calibration ($k_{2D.amb}$) and G peak calibration ($k_{G.amb}$). Both values become similar with the increase of I(D)/I(G) ratio.

Figure 4.11. Thermal conductivities of vacuum-annealed SiG derived both by 2D peak calibration ($k_{2D.amb}$) and G peak calibration ($k_{G.amb}$). Siimilar with ambient case, both values become closer with the increase of I(D)/I(G) ratio.

Figure 5.1. Schematic description on the 4-point measurement method for electrical conductivity. Gate voltage variation allows to derive the electrical mobility under the manipulation of majority charge carrier.

Figure 5.2. Design of the FET graphene/electrodes for the measurement of electrical properties using 4-point probe method.

Figure 5.3. Electrical conductivity of both PG and SiG samples with (a) the gate voltage variation (from -36 V to +36 V), and (b) the gate voltage difference variation (ΔV_g) (from -28 V to +28 V).

Figure 5.4. The reduction ratio (σ/σ_0) of SiG electrical conductivity (σ) compared to that of PG (σ_0) with the gate voltage variation. Larger reduction ratio for hole as a majority charge carrier can be attributable to the increased hole concentration in SiG, and noticeable decreasing reduction ratio with the increase of I(D)/I(G) can be observed.

Figure 5.5. The average reduction ratio (σ/σ_0) of hole and electron electrical conductivity (σ), and thermal conductivity reduction ratio (k/k_0) compared to those of PG (k_0 and σ_0) with the I(D)/I(G) variation. Observed lower k/k_0 compared to σ/σ_0 indicates the possibility of ZT enhancement in SiG.

Figure 5.6. Reduction ratio comparison ($(\sigma/\sigma_0)/(k/k_0)$) which shows the possibility of ZT enhancement in SiG with different I(D)/I(G) peak ratio (Si dopants concentration). Maximum more than 8 times enhancement can be achieved by substituting about 2.6% Si dopants into graphene lattices.

List of Tables

Table 3.1. Summarized results for the temperature calibration and temperature vs. incident heat flux with the I(D)/I(G) variation.

Table 4.1. Summary for the thermal conductivities with the I(D)/I(G) variation of Si-doped graphene. Note the order-of-magnitude reduction and two order-of-magnitude reduction of Si-doped graphene, compared to supported pristine graphene and suspended pristine graphene, respectively.

Table 4.2. Thermal conductivity reduction ratio (k/k_0) of substitutionally doped graphene at room temperature. The dopants concentration is 2% unless specified otherwise. Note that present work firstly demonstrates the thermal conductivity reduction of doped graphene as supported on the substrate.

Table 4.3. Comparison of critical defects concentration (N_c), average phonon MFP to inter-defect distance ratio (λ/d) with previous works showing the saturated thermal conductivity reduction.

Table 4.4. Maximum temperature of graphene for thermal conductivity measurement spots (T_m) and corresponding temperature for thermal activation boundary (T_{TAB}), and its radius (r_{TAB}).

Table 4.5. Temperature-dependent thermal conductivities of Si-doped graphene with the variation of I(D)/I(G). Note the negligible temperature dependence regardless of the I(D)/I(G) ratio.

Table 5.1. Electrical mobilities of PG and SiG samples with I(D)/I(G) variation. We found the minor decrease in electrical mobilities of SiG compared to thermal conductivity reduction, indicating the relative independent decrease in thermal conductivity under Si incorporation.

Chapter 1

Introduction

1.1. Background and motivation

Pristine graphene (PG) with perfect hexagonal carbon lattices exhibits outstanding phonon transport, which results in superlative thermal conductivities.[1-6] The observed outstanding in-plane thermal conductivity (k) of graphene can be attributed to the strongest bonding nature of sp² configuration with relatively light mass of carbon, and strict momentum conservation requirement of 2D materials which reduces initial and final states available for the scattering of heat carriers in the phase space. Those exceptional aspects give the large ballistic thermal conductance per unit area and long average phonon mean free path (MFP) of $\lambda \sim 775$ nm. However, the long phonon mean free path of graphene indicates that thermal conductivity can be significantly affected by the extrinsic scattering factors with intentionally introduced lattice defects. Defected graphene structures show considerably reduced in-plane thermal conductivities (k) when affiliated with edge roughness,[7] grain boundaries,[8,9] point defects,[10-14] carbon

^{13}C isotopes,[15] substitutional dopants to graphene,[14-19] or patterned nanoholes[20] (**Figure 1.1**). The reduced k can be attributable to the enhancing phonon scattering rate induced by these imposed defects. Such increases of phonon scattering are known to strongly influence the dependence of k on the sample size and temperature, in case of point defects, for instance.[14,21] In addition, it was found that thermal conductivity reduction with the increase of defects concentration can be self-limited by the additional defects, exhibiting the saturated reduction behavior.[13] Theoretical studies also showed a notable reduction of k when point defects were present that would alter the spectral phonon mean free paths (MFPs).[12]

The importance of defected graphene arises when further applications of graphene are needed to use it as potential future materials. One of the most disadvantageous property of graphene is the zero bandgap electronic bandstructure, which makes it hard to independently control the electron/hole charge carriers as semiconductors. Many previous studies experimentally showed that substitutional doping with foreign atoms can open the bandgap and increase the intrinsic charge carrier concentration.[22-24] However, these introduced defects can essentially degrade the thermal properties of graphene, mostly attributing to the inherent long phonon MFPs as mentioned above. Therefore, quantitative verification of thermal conductivity dependence on

the types of introduced defects or concentration should be preceded by the practical application of defected graphene.

However, most experimental previous studies regarding thermal properties alteration by defects examined the “extrinsic” effects of imposed defects. The intensive plasma radiation or high power e-beam, one of the simplest way to induce those extrinsic defects, can result in permanent damage to graphene and often convert the surrounding graphene to amorphous carbon-like structures. Those irradiation possibly deteriorates other novel properties of graphene such as its electrical properties or optical transparency.

In contrast, the “intrinsic” effects of substitutional dopant atoms need more attention for practical benefits since doped atoms do not violently destruct the hexagonal lattice structure and could quite possibly maintain the properties of graphene. Especially, substitutional dopants as defects for intentional properties control can lead to the graphene’s enhanced thermoelectric conversion efficiency (ZT).[4,20,25] Thermoelectricity is the direct conversion of energies between temperature and voltage gradient, which attributed to the asymmetric propagation of charge carriers under temperature gradient (**Figure 1.2**). Highly efficient thermoelectric materials have attracted many researchers because of their significant applications in terms of energy harvesting, electricity generation from the wasted heat, for example.

Thermoelectric conversion efficiency ZT is generally described as

$$ZT = \frac{\sigma S^2 T}{k}$$

where σ is the electrical conductivity, S is the Seebeck coefficient, T is the temperature, respectively. This thermoelectric efficiency of pristine graphene is generally known to be order of $10^{-4} \sim 10^{-2}$, attributing to its high thermal conductivity.[26,27] Henceforth, the lowered k through substitutional doping can lead to graphene's enhanced thermoelectric conversion efficiency.[4,20,25] This possibility is further supported by the fact that doped silicon atoms were reported to maintain the considerable electric charge carrier mobility of graphene.[28]

In this point, the substitutional dopant atom of our interest is silicon (Si) from the same group as C, both have two electrons in the outermost p -subshell (**Figure 1.3**). In 2012, unintentionally doped Si impurities in graphene lattices were found from STM images in spite of their large size difference.[29] In this case, Si/SiO₂ wafer or quartz tubes can be the source of Si impurities during the high-temperature (i.e. 1000°C) growth. Since 2014, some experimental synthesis of Si-doped graphene have been reported to be

successful with the solid, liquid and gas precursors.[28,30,31] Previously theoretical studies have also investigated the effect of Si dopants on the graphene properties alteration such as enhanced molecular sensing[30], opening of the bandgap[31], enhanced hydrogen storage capacity[32], and the role as a metal-free catalyst[33].

In terms of thermal conductivity reduction by substitutional dopants, Si-doped graphene (SiG) can be one of the most interesting platform because of their large mass difference with host C atoms, since the second-order perturbation analysis[34] showed that the carrier scattering rates increase with an increase of point defects concentration and proportionally to the square of the perturbed mass difference $(\Delta M)^2$. This large mass difference between Si and C could provide a significantly larger reduction in k , by over one order-of-magnitude further reduction when compared to the previously studied dopants with smaller ΔM , including ^{13}C ($\Delta M = 1$)[14,15], B ($\Delta M = 1.2$)[16], N ($\Delta M = 2$)[17-19], and ^{24}C ($\Delta M = 12$)[14]. In addition, previous report demonstrated the maintained considerable electrical properties of Si-doped graphene, justifying the investigation on thermal conductivity reduction by Si dopants for the thermoelectric efficiency enhancement of graphene.[28]

In spite of the presence of previous studies on the thermal properties of

substitutionally doped graphene, our extensive literature survey have found that previously published studies (**Table 1.1**) provided mostly theoretical predictions of k with an exception for the case of ^{13}C isotope[15] dopant for the experiment. Moreover, both theoretical and experimental published studies favored the thermally and atomically isolated configurations of suspended graphene when examining the effects of substitutionally doped foreign atoms on the quantitative thermal conductivity reduction. Considering that graphene itself is virtually impossible to be structurally self-standing, determination of the thermal properties of supported graphene justifies a more practical necessity. However, underlying solid substrate in the system of supported graphene is known to suppress the vibrational modes of flexural (ZA) phonons and reduce the phonon life times. This additional graphene-substrate interfacial phonon scattering reduces the $k = 2000 \sim 5000 \text{ W/m}\cdot\text{K}$ for the suspended PG to $k = 300 \sim 1000 \text{ W/m}\cdot\text{K}$ for the supported PG.[35-41] In spite of this significant effect of the substrate, the rareness of the previous studies on the defected supported graphene can be attributable to the complexities in affiliation with the inevitable out-of-plane heat transport through the substrate, worsening the measurement uncertainties to derive the in-plane thermal conductivity.[35,39] However, it was demonstrated that the use of extremely thin substrate could suppress the out-of-plane heat

dissipation and thus enhance the measurement reliability.

1.2. Objective of the study

The objective and scope of the study can be classified into three categories; **(1) To improve the synthesis method for the high-quality Si-doped graphene and understand how to control the doping properties, (2) To understand the thermal properties alteration of supported graphene induced by substitutionally doped Si atoms, and (3) To show the possibility of thermoelectric efficiency of graphene through substitutional Si doping.**

In chapter 2, we first compare the different synthesis methods available for the Si-doped graphene and improve them to obtain the high-quality Si-doped graphene. This may provide the exclusive understandings on the thermal properties alteration by Si dopants. By manipulating the synthesis parameters, we also understand how to control the doping characteristics such as doping concentrations or homogeneity. The controlled doping concentration enables to measure the thermal conductivities with doping concentration variation. Various characterization tools show successful synthesis of high-quality Si-doped graphene with full growth on copper catalyst.

In chapter 3, we firstly experimentally measure the in-plane thermal conductivity of Si-doped graphene with the increase of doping concentration, as supported on SiO₂ substrate using optothermal Raman thermometry (**Figure 1.4**). By facilitating the commercially available ultrathin 8-nm SiO₂ TEM grid, we enhance the measurement reliability for the derived the in-plane thermal conductivity. In addition, we conduct the thermal annealing after transferring graphene onto substrate to allow the precise reflection of substrate scattering on our measurement thermal properties.

In chapter 4, thermal properties of Si-doped graphene are discussed. The measurement results shows the significant reduction induced by Si dopants when compared with those of suspended and supported graphene. Other extrinsic scattering factors for phonon propagation such as grain boundaries and conformity with the substrate are also examined to exclusively understand the effects of substitutional Si dopants. Temperature dependence of thermal conductivity and possible thermal non-equilibrium between different heat carriers are investigated for the case of Si-doped graphene.

Finally, in chapter 5, we measured the electrical properties using the 4-point probe measurement with gate voltage variation. The reduction ratio of electrical conductivities are compared with those of thermal conductivities and we discuss the possibility of ZT enhancement by Si dopants.

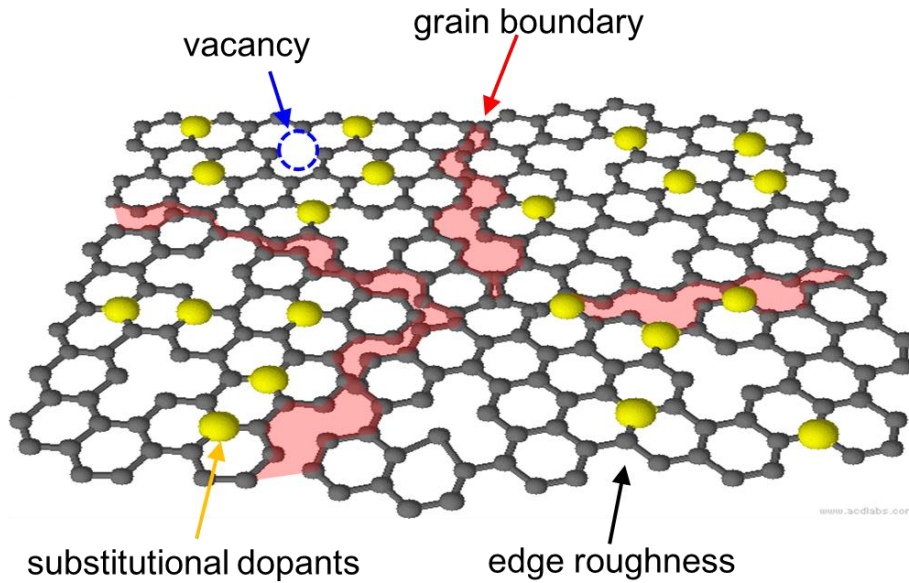


Figure 1.1. Schematic descriptions on the defected graphene with vacancy, substitutional dopants, edge roughness, and grain boundary. All of the defects inherently reside in the graphene hexagonal lattices, which suppresses the transport characteristics of energy carriers.

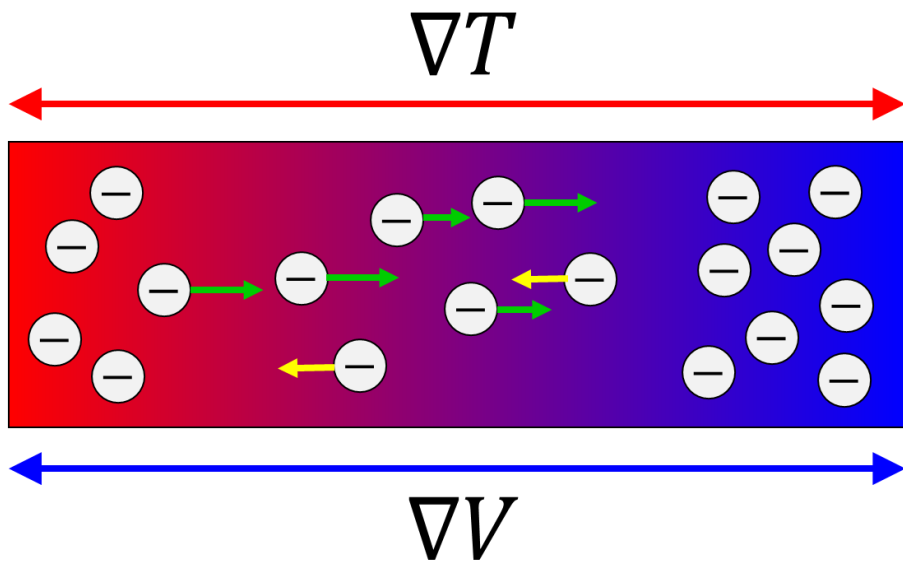


Figure 1.2. Simple description on the principle of thermoelectricity, which indicates the induced thermoelectric voltage in response to the temperature gradient across the materials, and vice versa.

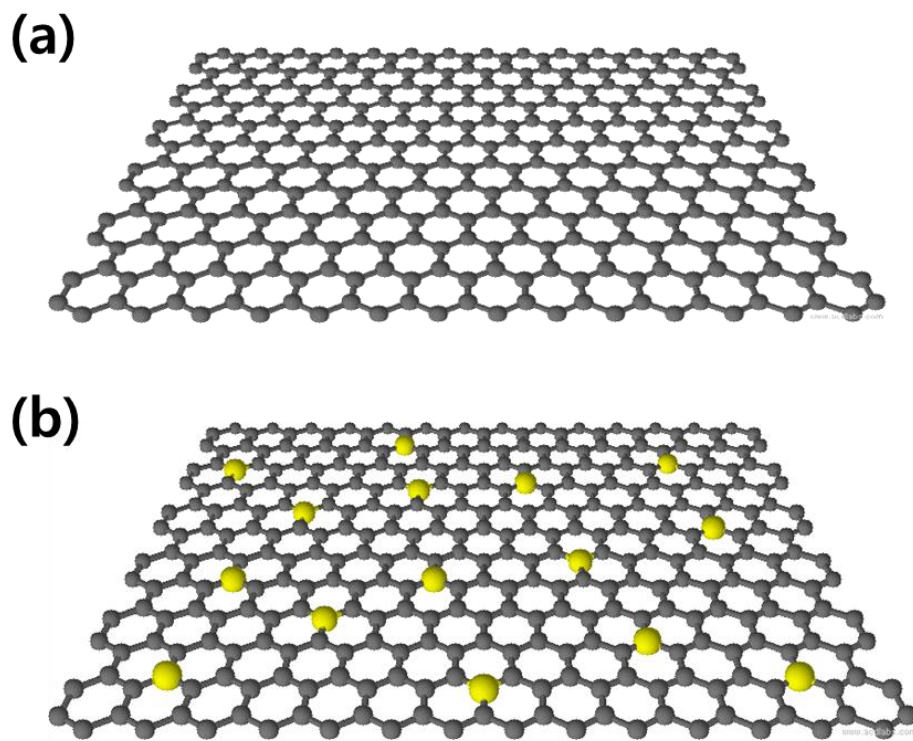


Figure 1.3. (a) Perfect hexagonal structure of pristine graphene, and (b) graphene with substitutional Si dopants of our interest.

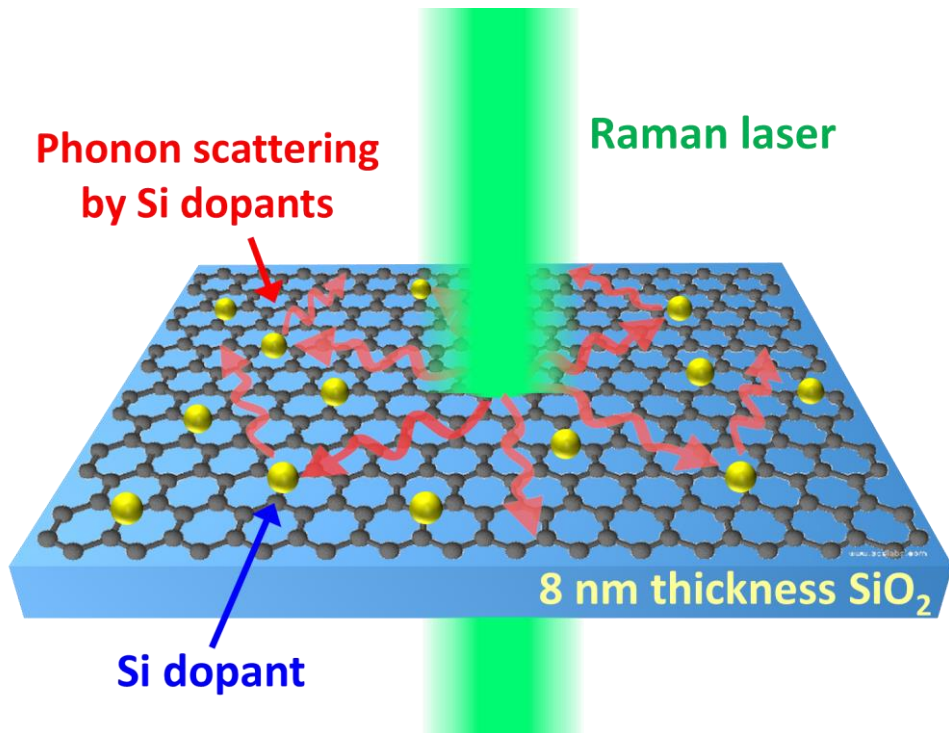


Figure 1.4. A description for the optothermal Raman thermometry to derive the in-plane thermal conductivity of Si-doped graphene as supported on extremely thin (8 nm) SiO₂ TEM grid. Note the significant phonon scattering induced by Si dopants.

Chapter 2

Synthesis of graphene

2.1. Methods for graphene synthesis

2.1.1. Pristine graphene

Since the first experimental preparation of atomically thin graphene layers by mechanical exfoliation so called ‘scotch tape method,[42] a few of available methods for the graphene synthesis have been established. Mechanical exfoliation is the method to peel the atomically thin graphitic layer from the HOPG (Highly Ordered Pyrolytic Graphite) and is known to provide the high-quality (i.e. single crystalline) graphene. However, it is hard to control the thickness, size, and area of samples for the practical application (i.e. scalability problem) and also suffers from the poor sample preparation repeatability.

Epitaxial growth of graphene is generally facilitate the commercially available SiC sample to directly grow the graphene layers.[43] By annealing the SiC at the high temperature (more than 1100°C) in vacuum, silicon atoms in SiC are sublimated and remaining carbon atoms are rearranged on the

surface to form the graphitic layers. The most advantageous aspects of epitaxial graphene growth is that no transfer process is needed to obtain the supported samples for the electronic devices. This possibly maintains its outstanding properties because inevitable crack or wrinkles during the transfer is one of the most attributable reasons for the conductivity degradation.[\(ref\)](#) Instead, graphene can be directly synthesized on the commercially available semiconducting substrates. But this promising synthesis method essentially requires the expensive synthesis conditions like high temperature and vacuum.

The third method we want to introduce is the reduced graphene oxide (rGO),[\[44\]](#) which is literally produced by the reduction process of the graphene oxide. In order to obtain the graphene oxide, three mechanical/chemical transformation processes of graphite should be needed; from graphite to graphite oxide, from graphite oxide to graphene oxide, and from graphene oxide to rGO. The most common methods to synthesize the graphite oxide is to intentionally oxidize it with the strong oxidizer like sulphuric acid. Then, it should be mechanically exfoliated as atomically thin layer sheets by ultrasonication as suspended in water. Therefore, rGO samples are generally synthesized as a colloidal sheets in liquid. Various reduction process can be successively to synthesize rGO. It is known that the properties

of rGO are affected by which the reduction processes are used, such as thermal annealing, microwave and photoreduction, or chemical methods. Note that graphene oxide has its own significance and advantages in terms of cost-effectiveness and mass production. Nonetheless, it cannot provide the large area layered samples with uniform thickness.

For the large area uniform synthesis, CVD (Chemical Vapor Deposition) process is the most widely accepted methods to synthesize the layered graphene.[45,46] In the CVD process, carbon sources from the precursors are deposited onto catalytic metal substrates at the high temperature (i.e. generally 800~1000°C), which nucleates the graphene islands. Continuous deposition of active carbon species finally merges nucleated islands as a fully-grown atomically thin layer. It has been experimentally verified that various solid[47,48], liquid[49,50], and gas[45] carbon sources can be used as precursors for the graphene synthesis. Due to the nucleated nature of CVD-synthesized graphene samples, they are essentially polycrystalline with the grain sizes of 1~10 μm order. This indicates that the most attractive properties of graphene (i.e. the highest thermal and electrical conductivity) can be degraded, attributing to the significant scattering of energy carriers at the edge of grain boundaries during their propagation. However, manipulation of synthesis parameters (i.e. synthesis time and precursor partial pressure) and

adoption of two-step pressure control process can provide the high-quality samples with minimum grain boundary scattering. Even the CVD synthesis of millimeter-scale single crystalline graphene has been reported, representing the comparable electrical mobility with mechanical exfoliated graphene.[51]

2.1.2. Substitutionally doped graphene

Substitutional doping or heteroatom doping means the replacement of host C atoms in graphene lattices with other foreign atoms as shown in **Figure 1.1**. The major purpose of substitutional doping is to semi-permanently tailor the properties of graphene for the specific application, which depends on the choice of heteroatoms. Some experimental studies have been reported to incorporate substitutional dopants such as nitrogen (N)[23,52], boron (B)[53], sulfur (S)[54], and phosphorus (P)[55]. The current available synthesis methods for substitutional doping can be classified into post-treatment doping and *in situ* doping.[56] Post-treatment substitutes specific dopants into already-synthesized graphene lattices. In contrast, *in situ* doping simultaneously incorporate the heteroatoms while achieving graphene synthesis.

Most post-treatment facilitate graphene oxide (GO) samples for the

preparation of doped graphene because reactive oxygen functional groups in GO can act as doping sites. Targeting heteroatoms are incorporated using high-energy sources such as thermal annealing, ultrasonication, and plasma with appropriate precursors. Thermal annealing treatment typically requires more than 600°C of high temperature but it can be helpful to self-heal the lattice defects or broken sp² bonding.[57] Ultrasonication conveniently substitutes heteroatoms when GO samples are dispersed in the solution phase of heteroatom precursors, which can be attributable to the hydrophilic properties of oxygen functional groups. Plasma treatment has been reported to successfully achieve the Cl doping using precursor-based plasma.[58] GO-based approach of above ‘post-treatment methods’ possibly provides the cost-effective mass production of doped graphene samples.

The simplest approach for *in situ* method is the ball milling, which mechanically breaks the lattice edges of substitution sites. Ball-milling of graphite with precursors of specific heteroatoms provides massive production of doped-graphene nanosheets at low cost. Synthesis of S-doped graphene using PG and sulfur power ball milling was reported.[59] However, it only incorporates dopants near hexagonal edges, attributing to the chemical/mechanical stability of graphene. This indicates that this approach is inappropriate not only for the properties manipulation of bulk graphene but

for the platforms to understand the dopants effect.

As mentioned above, chemical vapor deposition (CVD) process is known to provide the most qualified graphene samples in the practical application point of view, i.e. the large area, uniform single layer graphene. Likewise, simultaneous supply of heteroatoms precursors during the process of pristine graphene growth makes it possible to conveniently synthesize the large area doped graphene. In addition, doping concentration can be easily manipulated by adjusting the precursors ratios for heteroatoms and carbon atoms. Similarly, typical characteristics of synthesized graphene like the number of layers, doping concentration, and grain sizes can be controlled with optimized CVD process parameters like temperature, pressure, or growth time. The non-destructive nature of CVD for the synthesis of doped graphene can also yield the comparatively defect-free graphene compared to other methods. In spite of other disadvantages of high operating temperature, our works facilitate the CVD process to synthesize the Si-doped graphene. Note that some previous studies regarding the synthesis of Si-doped graphene also adopt the CVD process, which may be attributable to the advantages mentioned above.

2.2. Synthesis of Si-doped graphene

2.2.1. Review of previous studies

Our extensive literature survey has been found the available experimental synthesis for the Si-doped graphene using solid[28], liquid,[30] and gas precursors[31], respectively. Use of a solid precursor (triphenylsilane ($C_{18}H_{15}Si$))[28] is known to incorporate pure Si-C bonding structure (i.e. 102.1 eV in XPS spectra) in graphene lattices, however, the provision of both Si and C using single precursor makes it difficult to manipulate the Si doping concentrations. In addition, crystalline solid (particle) nature of precursors possibly contaminates the inner systems of furnaces and the lack of supply lines requires additional heating systems like firebricks or heating belt to sublime precursors (**Figure 2.1**). Moreover, it was found that the synthesized SiG exhibits approximately two order-of-magnitude smaller crystallite sizes compared to that of PG. This can be attributed to the increasing bonding disorders or vacancies, which can results in the excessively large I(D)/I(G) (i.e. defects concentration) peak ratio. They obtained the SiG with the doping concentration of 2.63 %.

Liquid precursors of MTMS (Methoxytrimethylsilane, $C_4H_{12}OSi$)/hexane (C_6H_{14}) mixture were reported to be available for the synthesis of SiG. MTMS and hexane provides the Si and C atoms, respectively. They facilitated the

bubbler-assisted (Ar gases) supply of liquid precursors while synthesizing SiG and controlled the doping concentration by varying the MTMS/hexane volume concentration. SiG samples with controlled doping concentration represent the proportional relation between the XPs-measured doping concentration and I(D)/I(G) peak ratio with maximum doping concentration of 1.75 %. In addition, XPS spectra exhibits the consistent Si bonding configurations between samples with different concentration and pure Si-C bonding.

In case of gas precursors (Silane (SiH_4) and methane (CH_4))[31], they also allows for the Si doping concentration control by manipulating the flux ratio of the two precursor gases. However, generally gas precursors are suffer from the safety issues of flammable gas (i.e. methane)[60,61]. In addition, synthesized SiG samples show the slightly inconsistent Si 2p binding energy spectra (100-101.2 eV) between doping concentration controlled samples and exhibits ambiguity in detailed Si bonding configuration. For instance, authors represent an additional peak at 103.2 eV with almost an equal strength in their XPS spectra, which was remained unknown (**Figure 2.2**). This may obstructs the comprehensive understanding of the altered graphene properties by Si dopants. They reported the doping concentration level of the range from 2.7 to 4.5 %.

In summary, it has been reported that those solid, liquid, and gas precursors can be used while achieving the growth of SiG but each available methods do not represent the consistent characteristics between samples such as Raman spectra, relation between doping concentration and $I(D)/I(G)$. We believe that this inconsistency can be attributable to the difference not only in precursors phase but in the different synthesis parameters like temperature or pressure. Note that our understanding on the previous synthesis methods justifies the use of liquid precursors, which exhibit the advantageous aspects especially in terms of consistent and well-known Si bonding configurations. Therefore, our work improves the synthesis procedure to establish the controllable synthesis recipes for the high-quality Si-doped graphene.

2.2.2. Improvement of synthesis method

Our improvement of liquid precursors-based CVD synthesis majorly lies on the understanding on the effects of synthesis parameters. While previous liquid precursor synthesis facilitates the ambient pressure (AP) CVD, we adopt the low pressure (LP) CVD. It is known that mass-transport limited kinetics in APCVD can lead to variation in the thickness of precursor species boundary layer along the catalyst due to inherent defects, dust or its roughness (**Figure 2.3**).[62] And the variation in the boundary layer thickness possibly

induces the non-uniform distribution of precursor species across the copper catalyst. On the other hand, the major limiting step for the synthesis under LPCVD is the surface reaction of those species with catalyst due to high diffusivity of the precursor species. This indicates that synthesis under LPCVD less suffers from the non-uniform precursor species distribution than APCVD. In addition, the lowered pressure enhances the copper evaporation rates and increases the desorption of activated carbon species during the graphene growth. This results in the decrease of the graphene nucleation density and successively reduces the grain boundaries. These aspects of LPCVD possibly reduces the possible deposition of particulates and lattice defects near grain boundaries. Enhancement of annealing time not only removes the possible inherent impurities in catalytic copper substrate and also helpful to increase the grain sizes of synthesized graphene.

As shown in **Figure 2.4**, our synthesis results represent the lowered I(D)/I(G) peak ratio with comparable Si doping concentration of previous works. It is known that all of the lattices defects can activate the D peak such as vacancy, sp³ types, or substitutional dopants. Therefore, our lowered I(D)/I(G) ratio with comparable Si doping concentration indicates that D-peak activating defects other than Si dopants can be significantly reduced in our LPCVD synthesis. In addition, our optimized synthesis represents the

consistent XPS & Raman spectra between samples and proportionality between Si doping concentration and I(D)/I(G) peak ratio, indicating the well-controllable synthesis.

2.3. Details in synthesis recipes

2.3.1. Recipe for pristine graphene

Pristine graphene (PG) was synthesized using the low pressure chemical vapor deposition (LPCVD) that gives the uniform monolayer graphene. In our experiment, 25mm-thick copper foil (2.5 cm × 5 cm in dimension) with 99.999% purity (Alfa aesar, Product # 13382) was pre-cleaned with nickel etchant to be used as a catalyst.[9,35,46] First, the furnace was ventilated to the order of 10^{-5} Torr after putting the copper foil inside the CVD furnace to minimize the possible oxidation of copper foil induced by remaining oxygen. After ventilation, catalyst copper foil was thermally annealed for 40 min at 1000°C with a flow of hydrogen to recrystallize the grains of copper and remove impurities (**Figure 2.5**). In order to obtain the fully-grown graphene of centimeter scale in dimension, we facilitate the two-step CVD that consists of two stage with different CH₄ : H₂ flow rate ratio while maintaining the temperature of 1000°C. At the initial stage (CH₄ : H₂ = 30 sccm : 5 sccm), the methane gas was flowed into the CVD furnace for 10 min to nucleate the

graphene on the copper foil. Then, graphene eventually becomes the fully-merged graphene layer at the second step under the enhanced flow rate of CH₄ (CH₄ : H₂ = 60 sccm : 5 sccm) for 5 min. After the synthesis, the CVD chamber was cooled down fast to atmospheric temperature with mild hydrogen gas flow (1.5 sccm).

2.3.2. Recipe for Si-doped graphene

For the Si-doped graphene (SiG) synthesis, both LPCVD and copper foil with 99.999% purity were identically facilitated. Liquid precursors, MTMS (Methoxytrimethylsilane, C₄H₁₂OSi) and hexane (C₆H₁₄), were used for the resources of Si and C atoms, respectively. Our CVD synthesis system (SciEn Tech Inc.) was modified to accommodate a controlled supply of liquid precursors, as shown in **Figure 2.6**. Driving force for the supply of liquid precursor is the pressure difference between the liquid container and CVD furnace. MTMS/hexane concentration was maintained as 0.8% volume concentration, which gives the single bonding feature between Si and C as previously reported.[28] Analogous to the pristine graphene synthesis procedure, CVD furnace was ventilated before the growth and copper foil was thermally annealed at targeting temperature (from 800 to 1000°C) for 40 min (**Figure 2.6**) under hydrogen flow of 5 sccm. Then, MTMS/hexane was

simultaneously supplied into CVD furnace for 20 min with Ar and H₂ flow while maintaining the targeting temperature. The flux ratio of Ar and H₂ flow is 1000 : 50 sccm and the precursors pressure. The amount of supplied precursor is varied from 0.02 to 0.08 Torr increment of pressure. Those pressure and temperature variation control the characteristics of synthesized SiG, as discussed later. Total pressure inside the quartz furnace during the growth corresponds to the ~1 Torr. Cooling to atmospheric temperature was followed with only Ar flowing (500 sccm).

2.4. Si doping concentration & homogeneity control

2.4.1. Doping concentration

Systematic synthesis experiments enable to manipulate Si doping concentration (i.e. $\sim I(D)/I(G)$) by varying the synthesis temperature and precursors pressure. Those parameters are controlled with the range from 800 to 1000°C, and 0.02 to 0.08 Torr, respectively. The substitutional doping of Si is progressed under the competition between the formation of C-C and Si-C bonds. The Si incorporation with relatively lower bond energy of Si-C bond (320 kJ mol⁻¹)[63] may prevail at lowered temperature when compared to C-C bonds in graphene with higher energy (346 kJ mol⁻¹).[64,65] This indicates that lowered synthesis temperature (i.e. 800°C) provides the higher Si dopant

concentrations due to its higher bonding formation probability. However, the coverage of SiG at lowered temperature tends to be incomplete, and the grain sizes become too smaller because of the denser nucleation of C atoms. The resultant significant phonon scattering at the edge of grain boundaries can obscure the Si dopants effects on the reduced thermal conductivity of SiG.[8,9] On the other hand, an increase of the synthesis temperature (i.e. 1000°C) can create larger grains, which is attributable to the enhanced copper evaporation rate during the synthesis. However, the increasing temperature suppresses the probability of Si-C bonding formation and this shows progressively decreasing Si dopant concentrations. In addition, when we elevate the precursor partial pressure from 0.02 to 0.08 Torr, the increase of dopant-substrate collision frequencies are expected, which possibly incorporates more Si dopants into graphene lattices.[23]

All of elaborated aspects are shown in **Figure 2.7**, which represents the I(D)/I(G) Raman mapping results of synthesized samples. In case of samples under 0.02 Torr synthesis pressure, the average value of I(D)/I(G) gradually increases showing 0.134, 0.278, and 0.332 when the synthesis temperatures are 1000°C, 900°C and 800°C, respectively. Similarly, average I(D)/I(G) increases from 0.312 to 0.614 when the temperature decreases from 1000°C to 900°C for the 0.08 Torr synthesis pressure. Note that average I(D)/I(G) and

Si doping concentration can be linearly correlated with the below equation of

$$C_{Si} = 3.4137[I(D)/I(G)] + 0.1296$$

where the C_{Si} is the XPS-measured Si doping concentration (see **Figure 2.4**).

2.4.2. Doping homogeneity

Systematic Raman mapping study allows the statistical approach to understand the effects of synthesis parameters on the Si doping homogeneity. We believe that synthesis temperature is the major factor that affects the doping distribution of SiG. This is because the formation probability of Si-C bond against C-C bond significantly depends on the synthesis temperature, as mentioned above. Doping homogeneity can be numerically compared by facilitating the standard deviation of I(D)/I(G) distribution in Raman mapping result (**Figure 2.8**). We found that the standard deviation decreases when the synthesis temperature decreases for both synthesis pressure. In addition, G peak and 2D peak Raman shift, whose position significantly depends on the doping characteristics, show homogeneous distribution when the temperature decreases, as shown in **Figure 2.9**. For lowered temperature, elevated probability of Si-C bond formation during the growth of each graphene

lattices can be attributed to the enhanced doping homogeneity. Also notable increases of $I(D)/I(G)$ average value are represented in **Figure 2.8**.

2.5. Sample characterization

2.5.1. Raman spectroscopy

Raman spectrums, non-destructive and versatile tool for the material characterization,[66,67] were obtained for PG and SiG after transferred onto SiO₂ TEM grid as shown in **Figure 2.10**. Typical intense peak, G peak (~ 1580 cm⁻¹) and 2D peak (~ 2680 cm⁻¹), are presented in the Raman spectrum of PG. It is known that G peak originates from the lowest order zero-momentum phonon (E_{2g}) scattering at the Brillouin zone center, while 2D peak corresponds to the excitation of two phonons with opposite momentum in the vicinity of the **K** point.[66,68] In addition, arising D peak and D' peak in SiG spectrum are activated by double resonant inter-valley and intra-valley process with defects which provide the lost momentum to satisfy the conservation.[69,70] Monolayer characteristics and negligible defects for PG are confirmed from the 2D peak to G peak intensity ratio ($I(2D)/I(G) \sim 3$) and D peak to G peak intensity ratio ($I(D)/I(G) \sim 0$), respectively. On the other hand, Raman spectrum of SiG shows the noticeable increase of $I(D)/I(G)$ compared to that of PG, indicating the D peak activation by Si dopants as

defects in SiG lattice.[28,30,31] The lowered 2D-G peak ratio can be attributed to the p-type doping and increasing rate of scattering between photoexcited electron and defects, both stemming from substitutional Si dopants.[68] In addition, deconvolution of SiG spectrum (inset of **Figure 2.10. (a)**) indicates the boundary-like properties of defects in SiG ($I(D)/I(D') \sim 4$)[71] induced by lattices distortion near substitutional Si dopants. Similar boundary-like nature of N dopants in N-doped graphene was already observed in previous work.[69] Those elaboration demonstrates the substitutional characteristics of Si dopants in graphene lattice.

2.5.2. X-Ray Photoemission Spectroscopy (XPS)

XPS can be used to analyze the surface characteristics of materials by measuring the binding energy of specific atoms. Quantitative doping concentration in SiG was deduced from the XPS spectra (SIGMA PROBE). We transferred synthesized PG and SiG onto sapphire substrate (Alfa Aesar, Product # 45020) before the XPS investigation, not typical SiO_2 substrate, to avoid the spectral interference of Si signal from the underneath substrate. In addition, transfer procedure also might help to remove the impurities or clusters in graphene/copper, thus increasing the spectral accuracy of the result. In **Figure 2.10. (b)**, single peak of binding energy at 102.1 eV demonstrates

the characteristics of single Si bonding to host C atoms.[28,30] In addition, negligible intensity near 103 ~ 105 eV reveals no bonding form of O – Si – C, for example.[28,30,72] Therefore, our SiG samples are pertinent to study the sole effect of Si dopants on thermal properties. And Si dopants concentration (Si/C) is calculated as 1.91 % in average from XPS spectra.

2.5.3. Scanning Electron Microscopy (SEM)

We facilitate the SEM to confirm the growth characteristics of as-synthesized graphene on copper foil. SEM image can visualize the contrast of as-synthesized graphene against underneath copper substrate, which is attributable to the large atomic number difference between carbon and copper. As shown in **Figure 2.11**, incomplete growth of graphene represents the notable contrast in the captured image, while fully grown graphene do not. This notable contrast also allows to visualize the growth of multilayer graphene. We confirmed the full growth of SiG before conducting all of the characterization.

2.5.4. Grain size visualization

Nucleation mechanisms for the CVD growth of graphene inherently exhibit the polycrystalline characteristics, whose grain boundaries essentially scatter

the propagating energy carriers. We visualize grain boundaries of PG and SiG after their full growth on copper catalyst in order to elaborate the effects of grain sizes on in-plane thermal conductivity (**Figure 2.12**). Mild dry annealing (MDA) enables the optical visualization of its grain boundaries by oxidizing underneath copper substrate.[9,73] Then digital image processing allows the derivation of average grain size, which is defined as area-equivalent diameter in statistical results. Both PG and SiG are found to have the micron-scale order grain size, 3.78 μm for PG and 1.04 μm for SiG, respectively. The reduced grain size of SiG is attributable to the decreased synthesis temperature from 1000°C to 900°C, which suppresses the copper evaporation rate and enhances the number of remaining nucleated carbon species. Along with the doping concentration analysis, we have discovered that the CVD synthesis at 900°C under 0.08 Torr precursor pressure provides the best tailored SiG for both large grain sizes and high doping concentrations, whose properties will be our main concern for the characterization and thermal conductivity measurement.

2.6. Summary

In chapter 2, we report the all of our elaborations regarding (doped) graphene synthesis, improved synthesis recipes, manipulation of doping

properties, and characteristics of synthesized graphene samples. Among the various graphene synthesis techniques, CVD justifies the practical necessity in terms of large area synthesis and properties controllability. In addition, heteroatoms incorporation can be easily conducted by supplying the precursors of targeting dopants. By comparing and summarizing available techniques for Si-doped graphene synthesis, we found that liquid precursors (MTMS/hexane) not only provide the pure Si-C bonding but manipulate the doping concentrations under controlled precursors concentration.

Our LPCVD allows to synthesize the high-quality Si-doped graphene with lowered defects. Surface-reaction limited kinetics and enhanced copper evaporation rate in LPCVD suppresses lattice defects induced by non-uniform distribution of precursors and nucleated grain orientation mismatch, respectively. I(D)/I(G) and Si doping concentration correlation shows that our SiG samples exhibit lowered I(D)/I(G) with comparable doping concentration. This represents that little defects other than Si dopants are reside in the lattices of our SiGs. We also found the linear correlation between the Si dopants concentration and I(D)/I(G), which provides the rough estimation on Si dopants concentration with I(D)/I(G) variation.

Manipulation of Si doping concentrations are conducted by controlling the synthesis parameters, temperature and precursors pressure. Reduced

temperature allows to increase the possibility of Si-C bonding incorporation, attributing to the lower Si-C bonding energy compared to C-C bonding. In addition, increased precursors also enhance the Si doping concentration by increasing the collision frequency to catalytic substrates. We also found that uniform Si dopants distribution can be obtained with lowered synthesis temperature. I(D)/I(G) Raman mapping and statistical analysis of Raman data support all of those experimental findings.

In terms of both significant grain size and Si doping concentration, SiG samples under 900°C synthesis temperature and 0.08 Torr precursors pressure are considered as optimized one, which will be used for the following research. Raman spectrum comparison indicates the substitutional dopants characteristics, p-type doping behavior, and boundary-like defects (lattice distortion) near Si dopants. XPS spectrum analysis represents the successful incorporation of pure Si-C bonding in SiG lattice. Fully-grown SiGs are ensured through the examination of SEM images. Finally, grain boundary visualization shows the order-of-magnitude larger grain sizes of both PG and SiG than average phonon mean free paths of graphene as supported on SiO₂ substrates.

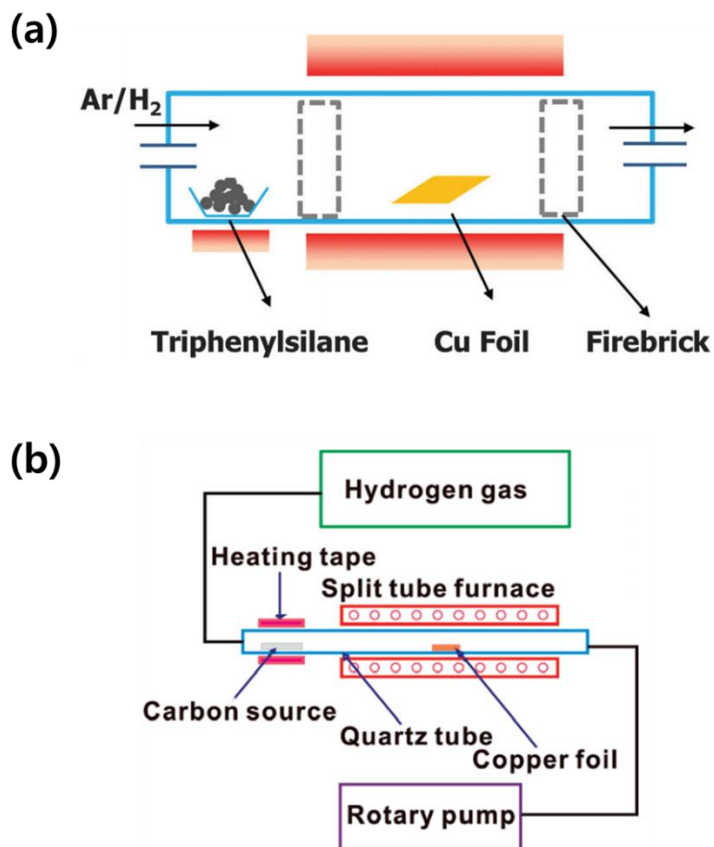


Figure 2.1. Schematics for the synthesis of (a) Si-doped graphene[28] (from Wang et al, 2015, *J. Mater. Chem. C*) and (b) pristine graphene[48] (from Li et al, 2011, *ACS NANO*) using solid precursors. Both system require the heating tape to sublimate the solid precursors after the annealing process. In addition, the furnace can be contaminated by placed solid precursors during the ventilation.

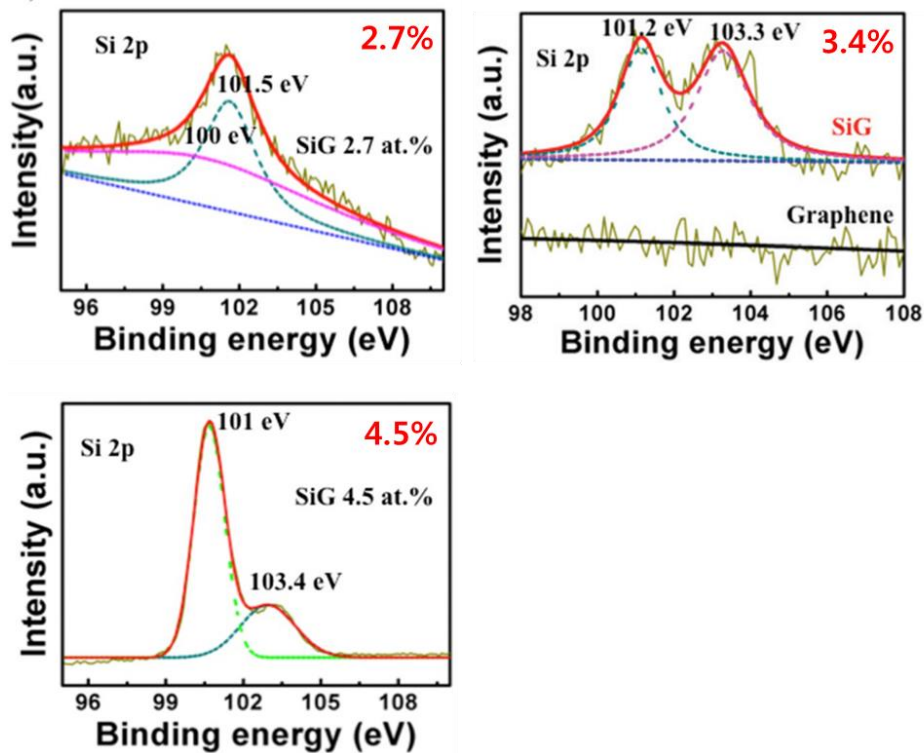


Figure 2.2. (From Zhang et al, 2016, *Nanoscale*) XPS spectrums of Si-doped graphene samples synthesized by gas precursors (methane and silane). Samples with different doping concentration represent the inconsistent XPS spectra with unknown peak of more than 103 eV. This obstructs the exclusive study on the pure Si dopants effects.

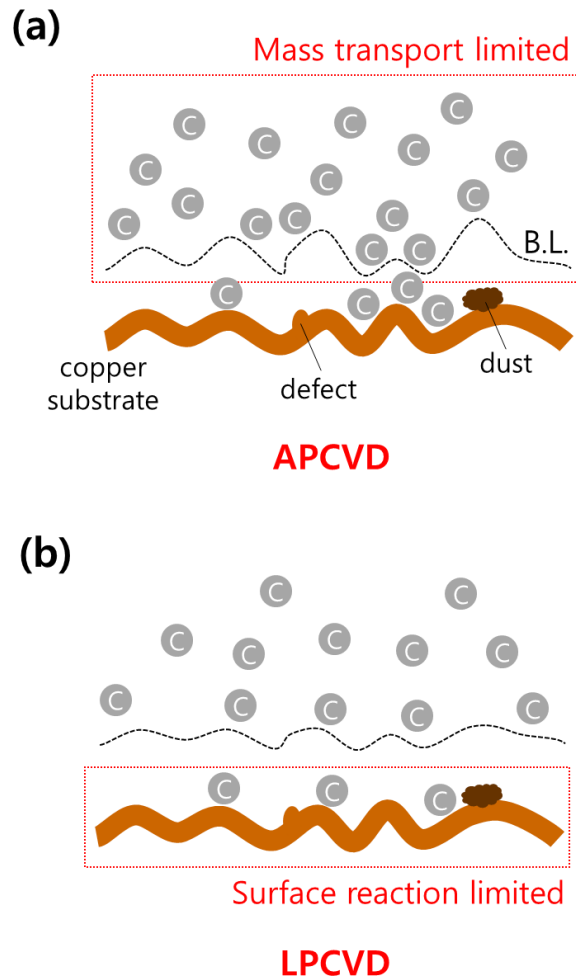


Figure 2.3. Descriptions on the kinetics in (a) APCVD and (b) LPCVD near copper substrates. Non-uniform precursors distribution near catalytic copper substrate can be attributed to the mass-transport limited kinetics in APCVD. On the other hand, surface reaction limited kinetics in LPCVD can synthesize uniform graphene as long as the temperature of the substrate is uniformly maintained.

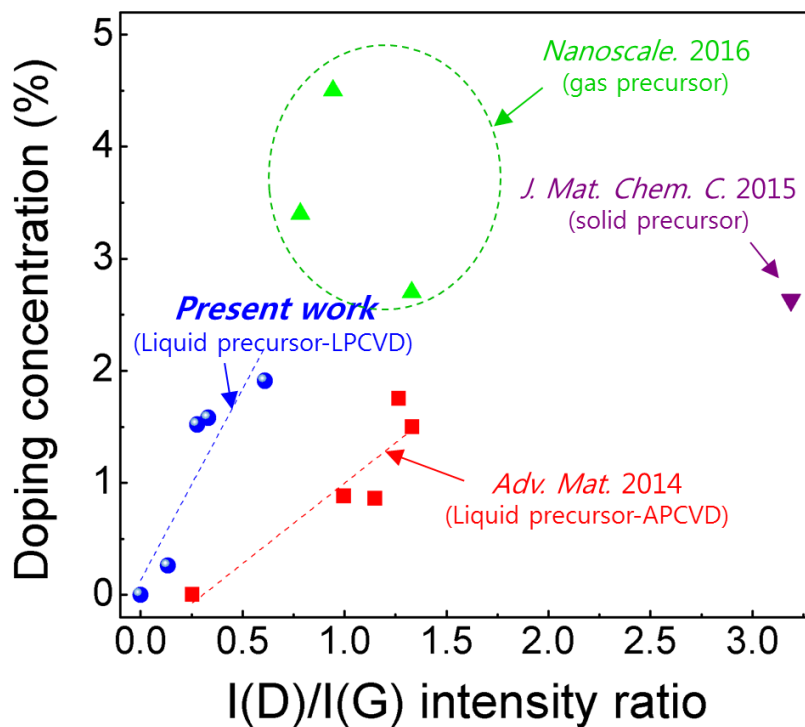
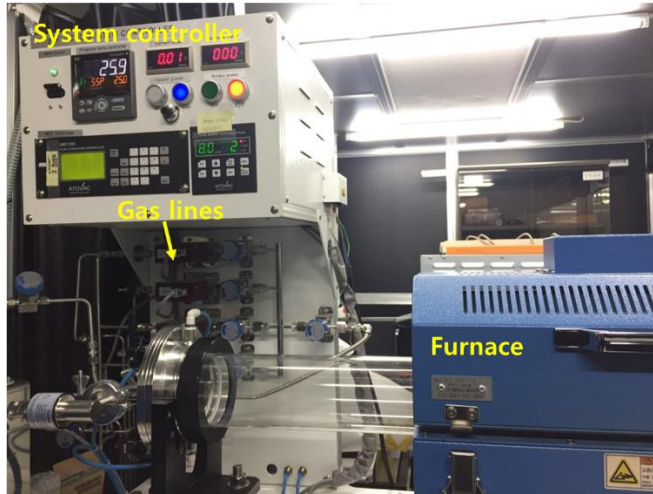


Figure 2.4. Si dopants concentration as functions of I(D)/I(G) Raman peak ratio for SiG samples with available synthesis methods using solid, liquid, and gas precursors. Lowered I(D)/I(G) with comparable Si doping concentration indicates the negligible defects in graphene lattices other than Si dopants.

(a)



(b)

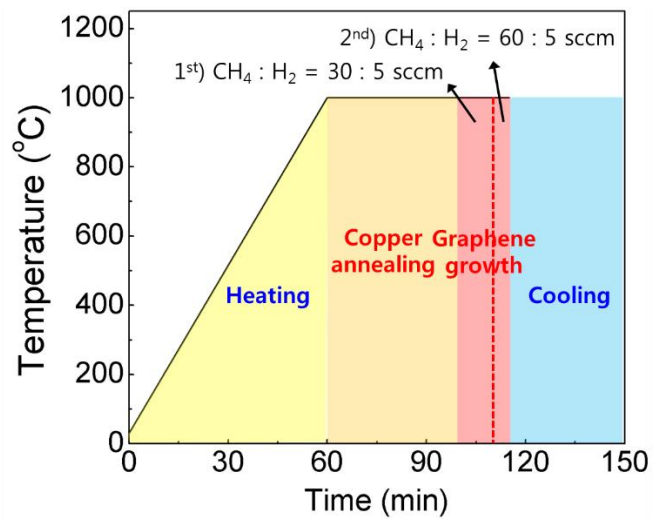


Figure 2.5. (a) CVD systems for graphene synthesis. (b) Descriptions on the pristine graphene synthesis procedures with time and temperature variation. Two-step method enables to grow the large domain graphene.

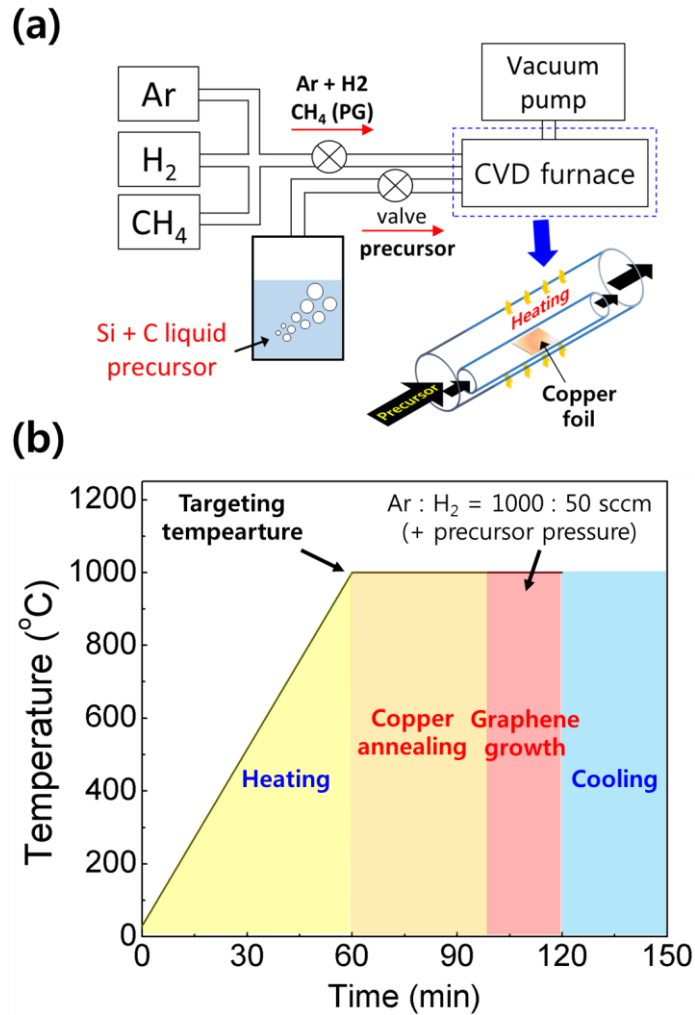


Figure 2.6. (a) Modified CVD system to accommodate the liquid precursors for the Si-doped graphene synthesis. (b) Descriptions on the Si-doped graphene synthesis procedures with time and temperature variation.

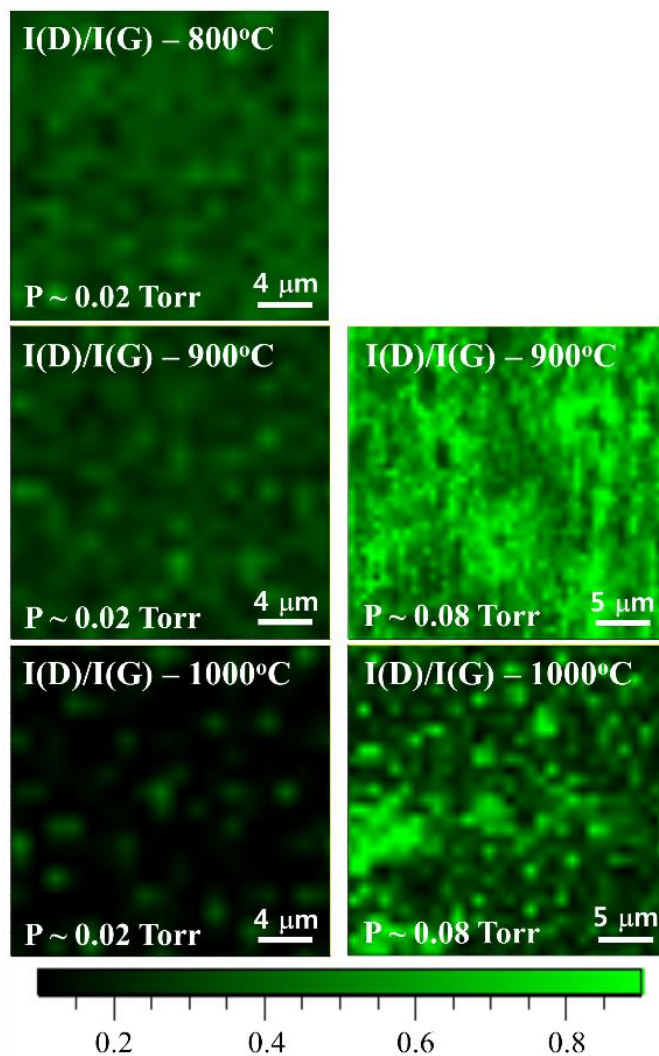


Figure 2.7. I(D)/I(G) Raman peak ratio mapping for the Si-doped graphene samples with different pressure and temperature conditions. Note that decreasing temperature and increasing precursors pressure enhance the doping concentration and homogeneity.

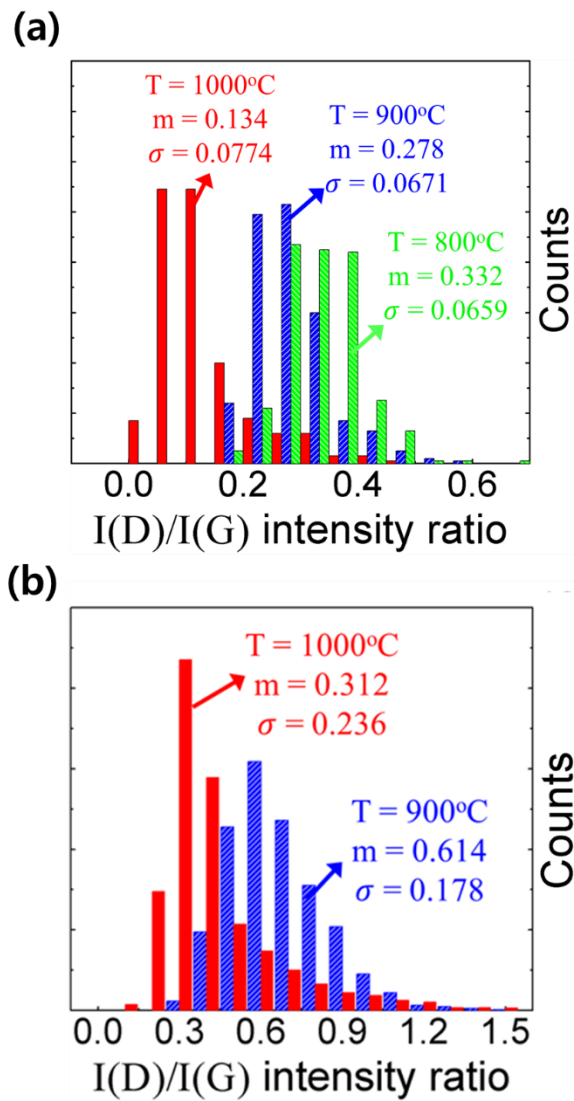


Figure 2.8. Statistical distribution of I(D)/I(G) peak ratio obtained from the Raman mapping in Figure 2.7. for the precursor pressure of (a) 0.02 Torr, and (b) 0.08 Torr.

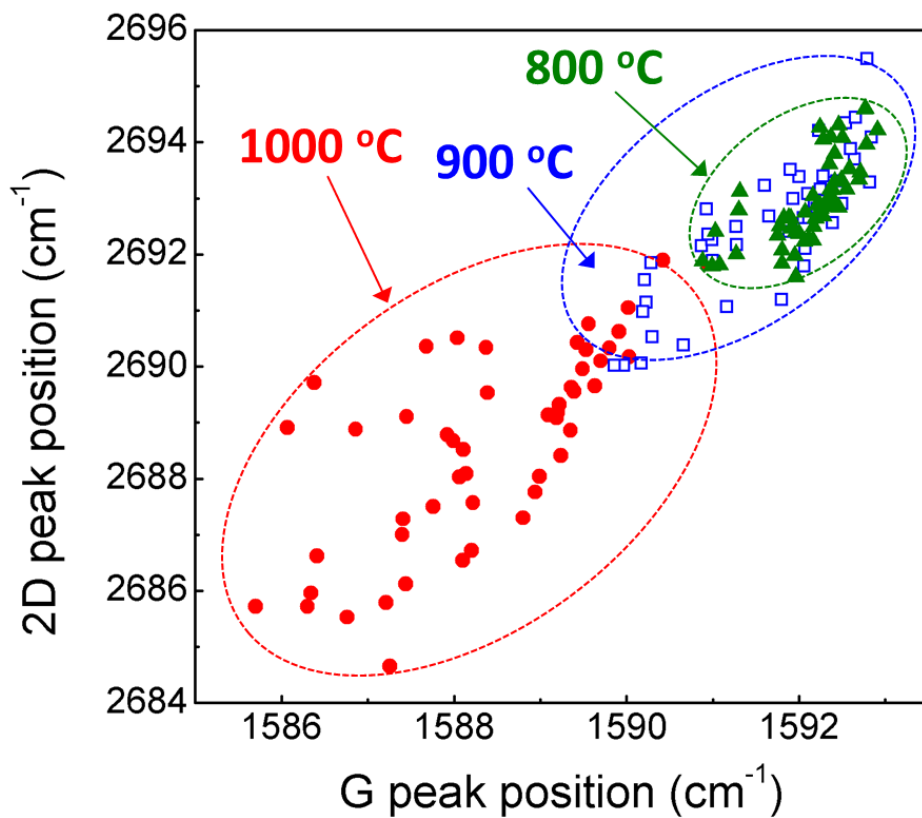


Figure 2.9. Distribution of G and 2D Raman peak position in Si-doped graphene synthesized with varied temperature at 0.08 Torr precursor pressure. More homogeneous distributions with lowered temperature indicates the homogenous Si doping distributions in Si-doped graphene. Randomly selected 50 positions data are represented.

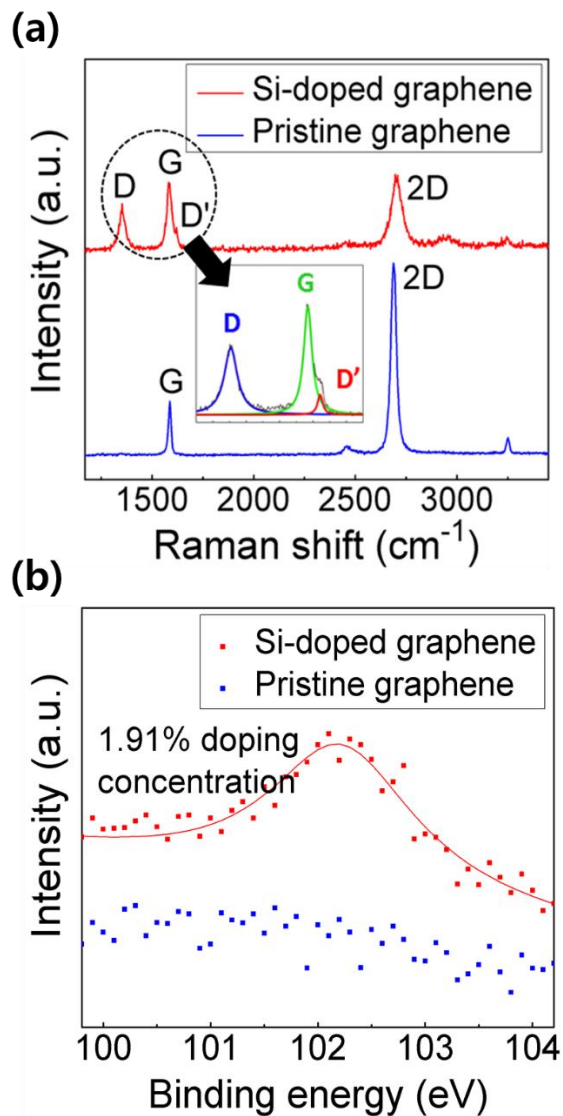
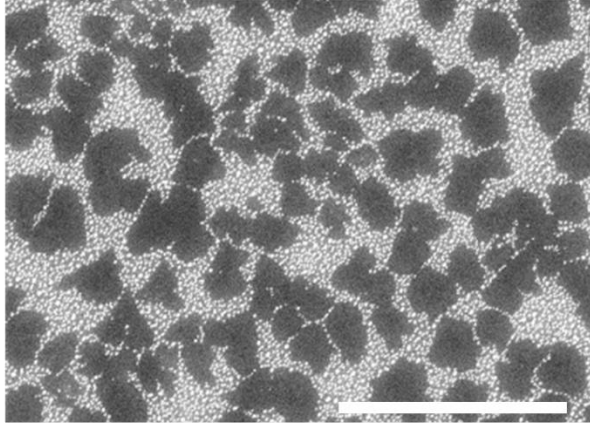


Figure 2.10. (a) Representative Raman spectrum of pristine graphene and Si-doped graphene. Inset figure shows the deconvoluted spectra, which indicates the boundary-like defects (lattice distortion) of Si dopants. (b) XPS spectra of near Si binding energy for both pristine graphene and Si-doped graphene.

(a)



(b)

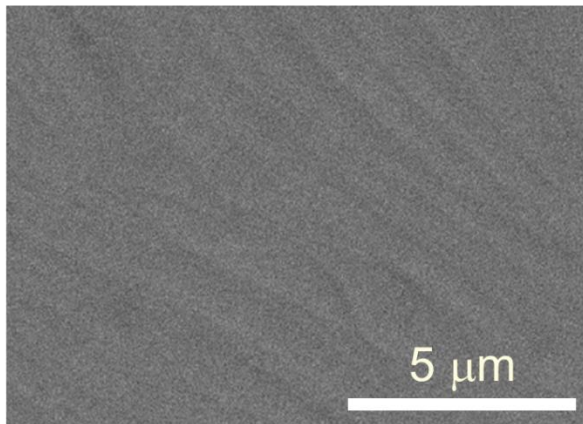


Figure 2.11. SEM image of **(a)** incompletely grown graphene and **(b)** fully-grown graphene. Some wrinkles in fully-grown graphene are observed.

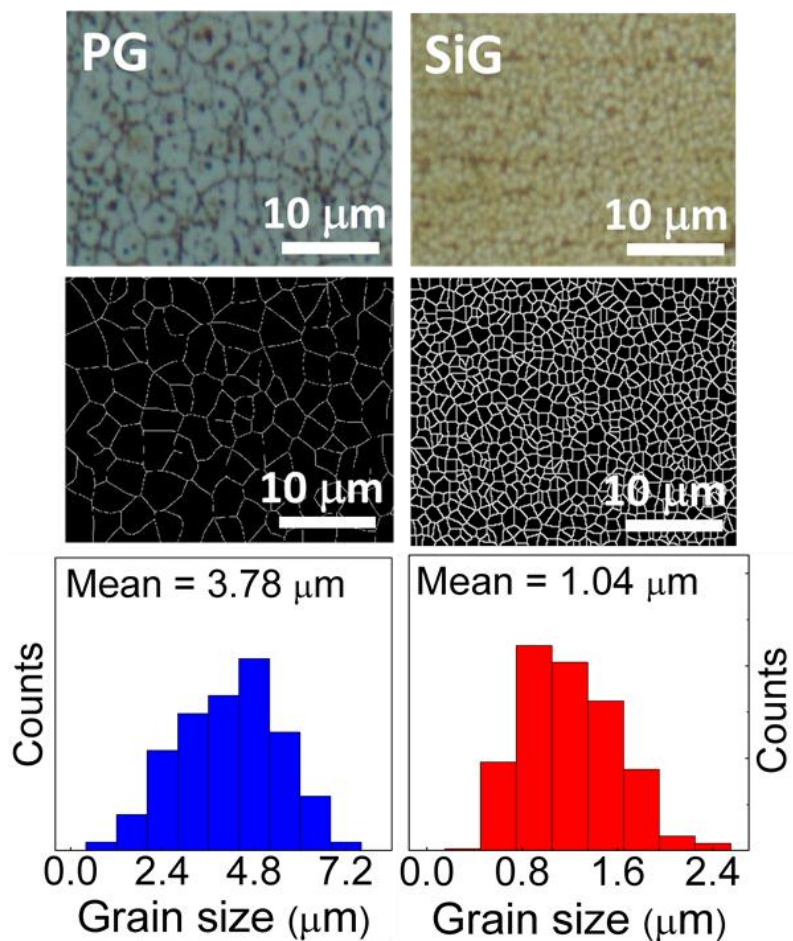


Figure 2.12. Grain size visualization of synthesized pristine graphene and Si-doped graphene. MDA enables to optically observe the grain boundaries of graphene. Lowered synthesis temperature in Si-doped graphene can be attributable to the decreased grain size.

Chapter 3

Thermal conductivity measurement

3.1. Measurement scheme

Thermal conductivity derivation basically requires the measurement of temperature enhancement of specific materials under the input heat (or power). This is because diffusive heat transport can be generally described by the below Fourier law

$$Q = -kA \frac{dT}{dx}$$

where Q is the heat flux, A is the cross-sectional area, k is the thermal conductivity, and dT/dx is the temperature gradient along the heat propagation direction, respectively. Sufficiently larger system size compared to average phonon MFPs of materials ($L \gg \lambda_p$) ensures the diffusive heat transport when the phonons are dominantly scattering between themselves, not restricted by system physical boundaries.[4] Therefore, experimental measurements design should develop how to give the heat flux, precisely

measure the temperature enhancement and materials geometry.

In case of graphene, thermal conductivity measurement of graphene can be conducted by both electrical method and Optothermal Raman method. Electrical resistance methods electrically heat the graphene and derive the temperature enhancement from the calibration data with measured resistance.[41] In spite of the measurement accuracy, sample preparation procedure should follow the complicated fabrication process which possibly contaminates the samples. In addition, micron-scale patterning makes it hard to completely neglect the effects of phonon boundary scattering.

Optothermal Raman method, the main concern of our research, facilitates the Raman laser as a heater and a temperature prober.[9,35,39,74] Raman spectrum of graphene generally represents the distinct peaks, whose center position depends on the temperature increment. Therefore, temperature probe through the Raman laser can be easily accessed by recording the Raman peaks shift with the temperature variation. Note that each of Raman peaks reflect the temperature of specific phonons, LO phonons for G peak and TO phonons for 2D peak, for instance.[75,76] In spite the relatively higher measurement inaccuracy, the simple fabrication process allows us to facilitate the Raman method for the measurement of SiG thermal conductivity. Fortunately, our group research demonstrates the enhancement of measurement accuracy

through the use of extremely thin substrate, as described in the next section.

3.2. Sample preparation

3.2.1. Why supported graphene?

When the graphene samples are synthesized and facilitated for the experimental or practical applications, one-atom-thick layers should be transferred and supported onto the solid substrates. This is because graphene cannot be essentially self-standing without underlying substrates, which is attributable to its high surface energy. Therefore, investigation on the graphene properties as supported justifies more practical necessity. In addition, underlying solid substrates are known to significantly scatter the propagating energy carriers, whose scattering rates depends on the materials properties and contact conditions. In spite of the importance of the substrate effect, only the suspended graphene samples are facilitated in previous studies when investigating the quantitative alteration of thermal conductivities by introduced defects.[10,13,15] For the optothermal Raman measurement, the ambiguity majorly lies on the uncertain dissipation of heat through the underlying substrate (out-of-plane), as described in **Figure 3.1**. This 3-D complexity obstructs the precise derivation of in-plane thermal conductivity, compared to the suspended samples.

In spite of above practical ambiguities in deriving the supported graphene thermal conductivity, previous study innovated the accuracy-enhanced Optothermal Raman thermometry with the utilization of extremely thin substrate.[35] Use of an ultra-thin (8-nm) SiO₂ TEM grid as supporting substrate turned out to minimize the heat dissipation through the substrate compared to the typical SiO₂/Si substrate (**Figure 3.2**). About five order-of-magnitude reduction of substrate thickness not only increases the in-plane thermal resistance and substrate heat capacity, thereby significantly enhancing the measurement reliability for in-plane thermal conductivity of graphene. The resulting in-plane conductivity of the supported graphene was affected neither by the wide variation of the temperature-dependent substrate conductivity nor the inherently uncertain graphene-substrate interfacial conductance.

3.2.2. Graphene transfer

SiG samples grown on copper foil are transferred onto 8-nm thick SiO₂ TEM grid, following the procedure described in **Figure 3.3**. First, PMMA solution is prepared by dissolving the PMMA powder (Sigma Aldrich, #182265) in chlorobenzene (Sigma-Aldrich, #319996) with 46 mg/ml concentration and continuously stirring for 2 days. Graphene/copper samples

are coated with PMMA layer by spin-coating PMMA/chlorobenzene solution with 4000 rpm for 45s. Then, PMMA layers are cured by annealing at 165°C for 90 sec. Copper etchant solution is made by the sonication of Ammonium Peroxydisulfate (Alfa Aesar, #54106) dispersed in DI water with the concentration of 1 mg/50ml, where PMMA/graphene/copper layers are gently placed. After mild etching of underneath copper, DI water jet spray is conducted on behalf of O₂ plasma to remove the graphene grown on the opposite side and enhance the rate of copper etching. Then, PMMA/graphene/copper samples are cut into 1 mm × 1 mm pieces and placed again into etchant to completely remove the underneath copper foil. After 3 hours, PMMA/graphene samples are rinsed with DI water for 30 min, and successively they are transferred onto targeting 8-nm SiO₂ TEM grid. Because of their small size, we use the “perfect loop” (TED PELLA, #13064) which facilitate the surface tension for the easy pick-up and transfer (**Figure 3.4**). After transfer, PMMA/graphene/SiO₂ samples are dried in ambient and vacuum, for 30 min, respectively. Supporting PMMA layers are removed by dipping samples in acetone for 90 min, and successive cleaning with IPA and DI water completes the whole transfer process. Optical visualization with 100x objective lens represents the successful transfer with minimum wrinkles or folded area, as shown in **Figure 3.5**.

3.2.3. Thermal annealing

We mentioned that graphene-substrate scattering dominantly influences on the in-plane thermal conductivity of supported graphene, attributable to the significant suppression of out-of-plane vibrational ZA phonon modes.[6,41] However, note that inevitable initial suspension of graphene after wet transfer onto solid substrate do not ensure the complete adhesion between graphene and substrate. For example, thermal conductivity measurement immediately after the transfer is known to exhibit the comparable values with suspended graphene (~ 2000 W/mK), indicating the ‘suspended-like’ adhesion of ‘supported graphene’.[35] On the contrary, supported graphene can reflect the significance of substrate phonon scattering by enhancing the graphene-substrate conformity (adhesion). The dependence of graphene-substrate adhesion on the sample preparation conditions can interrupt the precise determination of in-plane thermal conductivity.

Therefore, we prepare the supported Si-doped graphene samples with the significant graphene-substrate conformity by repeated thermal annealing in ambient and vacuum. It is known that intercalated water molecules between graphene and solid substrates can be attributed to the significant graphene-substrate separation distance after wet transfer.[35] By conducting the repeated thermal annealing, those intercalated molecules can be removed and

therefore graphene-substrate conformity can be enhanced. Moreover, annealing in high vacuum additionally enhances the graphene-substrate conformity with further removal of intercalated molecules. Those samples can reflect the significant effects of underlying substrate in supported graphene. Note that vacuum-annealed supported pristine graphene exhibits the thermal conductivity of ~ 600 W/mK, order-of-magnitude lower than values measured immediately after transfer.[35]

To avoid the above ambiguity for the thermal conductivity derivation, supported Si-doped graphene samples with different conformity conditions were prepared by (1) annealing in the ambient pressure (ambient-annealed) with temperature range from 300 K to 500 K for more than 10 times and (2) annealing in high vacuum of 10^{-7} Torr (vacuum-annealed) with the same temperature range for 2 hours. Ambient-annealed samples may exhibit the intermediate conformity to the underlying substrate attributing to the remaining ambient species between graphene and substrate. On the other hand, vacuum-annealed samples could be corresponded to the supported graphene with saturated graphene-substrate conformity under the strongest phonon scattering from the substrate. This can be evidenced by room temperature thermal conductivity of ambient-annealed PG (900.18 W/mK, more than 10 times annealing at 530 K in average) higher than that of

vacuum-annealed PG (645.56 W/mK, annealing in a high-vacuum of 10^{-7} Torr with same temperature), as our previous study demonstrated.[35] We measured and found the thermal conductivities reduction for both ambient-annealed SiG and vacuum-annealed SiG by comparing them with those of PG under corresponding thermal annealing condition.

3.3. Thermal conductivity measurement

3.3.1. Detailed procedure

Thermal conductivity measurement procedure follows the three steps; (1) Measurement of effective optical absorption (α_{eff}), (2) Temperature calibration of graphene samples, (3) Measurement of temperature enhancement by irradiated heat flux, and (4) Numerical calculation of heat diffusion equation.

First, we measure the effective optical absorption of the Si-doped graphene as supported to calculate the precise given heat flux in samples. Our measurement scheme considers not only direct absorption from given heat flux but the reflected heat flux from the underlying substrate, as shown in **Figure 3.6**. The effective optical absorption of supported graphene can be described as

$$\alpha_{eff} = \alpha_g + \alpha_g \rho_{SiO_2} (1 - \alpha_g)$$

where the α_g is the optical absorption of graphene and ρ_{SiO_2} is the reflectance of underlying SiO₂. Here, α_g and ρ_{SiO_2} can be estimated by measuring the transmitted heat flux with and without the graphene, and SiO₂ TEM grid.

Our measurement experimentally determined the effective absorption of SiG to be $1.97 \pm 0.237 \%$ at $\lambda = 514 \text{ nm}$. The decreased effective absorption for the supported SiG from the generally accepted value of 2.3% for the suspended graphene is accredited by the internal reflections from the SiG-substrate interface.[35] The universal relation[77] between the optical transmittance (T) and optical conductivity (G) is given by $T = (1 + 2\pi G/c)^{-2}$ with the speed of light c . Defected graphene generally exhibits the decreasing optical conductivity, either by functionalization[78] or plasma irradiation[79]. Likewise, the substituted Si atoms provide the enhanced scattering of propagating electrons, and the reduction of the optical conductivity by the Si atoms can lead to an increase of the transmittance and thus a decrease of the absorption. Previous studies already demonstrated the decreasing optical absorption of Si-doped graphene.[28]

Note that graphene surface reflectance and the absorption of SiO₂ substrate

are assumed to be negligibly small, attributing to the facts of less than 0.1% for the visible range from 400 nm to 700 nm[77] (graphene reflection), and the extinction coefficient (the imaginary part of the complex refractive index) being less than 2×10^{-4} for the range above 330 nm (SiO₂ absorption), respectively.[80] When the heat flux is given by Q , the actual heat flux in the equation should be given as $\alpha_{eff}Q$.

In second stage, graphene samples are placed onto hot plate to linearly calibrate graphene temperature with Raman peak positions shift, dw/dT . Before the calibration, we repeatedly anneal the samples for more than 10 times with the range up to 500 K to enhance the graphene-substrate conformity (ambient-annealed samples). Then, we correlate both 2D peak and G peak shift with the hot-plate temperature interval of 30 K. For the each temperature, we collected more than 10 Raman spectrums to estimate the uncertainties range from the measurement error. Note that we facilitate the 514 nm wavelength laser and 100x objective lens for the whole Optothermal Raman measurement (inVia-reflex, Renishaw).

After the calibration, we record the Raman shift under the targeting input heat flux, given by Raman laser (dw/dQ). Given heat flux is measured by using the power meter. Maximum given heat flux is set as $\sim 1\text{mW}$, attributing to the expected lower thermal conductivity of Si-doped graphene. Again we

collected more than 7 Raman spectrums for each incident heat flux to estimate the measurement uncertainty. Use of calibration data enables to obtain the temperature increment by the given heat flux. Probing the temperature enhancement of vacuum-annealed samples are followed by the measurement for ambient-annealed samples. Note that linear correlation of dw/dQ allows to derive the effective thermal conductivity near room temperature, while the exclusive derivation with each Q vs. w relation gives the temperature-dependent thermal conductivity.

Heat diffusion equation for our graphene/SiO₂ system can be described by below separated governing equations with cylindrical coordinate as.[9,35,39,74,81]

$$\text{at graphene : } k_g \frac{1}{r} \frac{d}{dr} \left(r \frac{dT_g}{dr} \right) - k_{SiO_2} \frac{1}{r} \frac{d}{dr} \left(r \frac{dT_{SiO_2}}{dr} \right) - \frac{h}{t_g} (T_g - T_a) +$$

$$q''_{laser} = 0$$

$$\text{at SiO}_2 \text{ substrate : } \frac{1}{r} \frac{d}{dr} \left(r \frac{dT_{SiO_2}}{dr} \right) + \frac{d^2 T_{SiO_2}}{dz^2} = 0$$

The boundary conditions for above equations are given by:

$$T_g(\infty) = T_{SiO_2}(\infty, z) = T_\infty$$

$$\left. \frac{\partial T_g}{\partial r} \right|_{r=0} = \left. \frac{\partial T_{SiO_2}}{\partial r} \right|_{r=0} = 0$$

$$k_{SiO_2} \frac{1}{r} \frac{d}{dr} \left(r \frac{dT_{SiO_2}}{dr} \right) \Big|_{z=t_{SiO_2}} = G(T_g - T_{SiO_2} \Big|_{z=t_{SiO_2}})$$

$$k_{SiO_2} \frac{\partial T_{SiO_2}}{\partial z} \Big|_{z=0} = h(T_{SiO_2}(r, 0) - T_a)$$

Here, k_g and k_{SiO_2} are the thermal conductivity of graphene and SiO₂ (1.37 W/mK)[82], T_g and T_{SiO_2} are the temperature of graphene and SiO₂ substrate, t_g and t_{SiO_2} are graphene (0.335 nm) and SiO₂ thickness (8 nm), h is convective heat transfer coefficient of graphene ($2.9+5.1/-2.9 \times 10^4$ W/m²K)[74], T_a is room temperature (300 K), and G is thermal boundary conductance (30 MW/m²K)[83] between the substrate (SiO₂) and graphene. Another parameter q''_{laser} is the absorbed heat flux calculated as $\alpha_{eff} q_o'' \exp(-2r^2/r_o^2)$ with Gaussian energy distribution of incident laser, and α_{eff} is the effective absorption of graphene under the additional consideration of reflection from the substrate. The laser beam radius r_0 is the estimated as $r_0 = \lambda_L/(\pi NA)$ ($NA = 0.75$, $\lambda_L = 514$ nm). Note that out-of-plane conduction through the underlying substrate and convective heat

transfer are also considered (**Figure 3.7**)

We facilitate the Gauss-Seidel iterative numerical analysis under finite different scheme to derive the two-dimensional temperature distribution for the graphene/substrate.[9,35] Temperature distribution in graphene derived from the governing equation can be weight-averaged as effective temperature of graphene, T_m , using the below equation.

$$T_m = \frac{\int T_g(r) \exp(-2r^2/r_0^2) r dr}{\int \exp(-2r^2/r_0^2) r dr}$$

Determination of k_g can be conducted by facilitating k_g as a fitting parameter matching the experimentally measured graphene temperature T_m and numerically calculated T_m with given parameters.

Note that we conduct experiments with the I(D)/I(G) variation by exclusively probing the area with different I(D)/I(G) peak ratio. We believe that this enables to elaborate the effects of Si dopants concentration on the thermal conductivity reduction of graphene. We selected the 7 points with the different I(D)/I(G) peak ratio with the range from 0.38 to 0.88. Our estimation in chapter 2.4.1 indicates the corresponding Si dopants concentration range of 1.43 % ~ 3.13 %.

3.3.2. Temperature calibration result

In case of pristine graphene, 4 peaks in Raman spectrum can be facilitated for the temperature calibration (**Figure 3.8**). Previous study demonstrated that zone-center longitudinal optical (LO) phonons are associated with the G peak ($\sim 1580 \text{ cm}^{-1}$), and transverse optical (TO) phonons are related to the emerging 2D peak ($\sim 2680 \text{ cm}^{-1}$). [75] Two minor peaks, D+D'' peak ($\sim 2450 \text{ cm}^{-1}$) and 2D' peak ($\sim 3240 \text{ cm}^{-1}$) involves the LA/TO phonons and two LO phonons, respectively. For the temperature calibration of Si-doped graphene, both G peak and 2D peak are used, attributing to their distinct peak shape and high intensity. To elaborate the effects of Si doping concentration on the measured thermal conductivities, we individually calibrate the temperature with the $I(D)/I(G)$ variation, which reflects Si dopants concentration as mentioned in Chapter 2. All of the calibrations are conducted for the temperature range from 300 K to 430 K.

For the all measured case of $I(D)/I(G)$, 2D peak calibration results (dw_{2D}/dT) represent the sensitive temperature dependence compared to those of dw_G/dT , indicating the better measurement reliability of 2D peak calibration (**Figure 3.9**). In addition, both dw_{2D}/dT and dw_G/dT decrease with the increase of $I(D)/I(G)$ (Si dopants concentration). This indicates the enhanced temperature increment with the same Raman shift, possibly

translated as the decrease of thermal conductivity. Note that we linearly correlate the Raman shift and graphene temperature. The results are summarized in **Table 3.1**.

During the calibration experiment, we avoid the local heating by facilitating the low power laser of ~ 0.05 mW. Because the hot plate heats the graphene at the bottom of graphene/SiO₂ samples, the low thermal conductivity of SiO₂ ($k_{SiO_2} = 1.37$ W/mK) possibly induces the temperature gradient along the out-of-plane direction. However, we assume that supported graphene temperature is almost same with the hot plate set-up temperature. This can be justified by the use of extremely thin (8-nm) SiO₂ TEM grid, which minimize the possible temperature gradient between the graphene surface and the bottom of substrate. We also emphasize that Gaussian fitting is facilitated to record the Raman peak shift center for each spectrums.

3.3.3. Temperature enhancement under heat flux

Next, we record and linearly correlate the Raman peaks shift with the variation of heat flux input, Q . By using the obtained data of dw_{2D}/dQ and dw_G/dQ , temperature of graphene under specific input heat flux can be obtained following the below equations

$$T_G = \frac{dw_G}{dQ} / \frac{dw_G}{dT} + 300$$

$$T_{2D} = \frac{dw_{2D}}{dQ} / \frac{dw_{2D}}{dT} + 300$$

where T_G and T_{2D} indicate the graphene temperature obtained from the G peak calibration and 2D peak calibration, respectively (**Figure 3.10 and 3.11**). Thermal conductivities are derived by matching the experimentally measured temperature (T_G and T_{2D}) and the numerically calculated temperature T_m with fitting parameter of thermal conductivity (k). This also enables to obtain the thermal conductivities with the temperature variation.

As shown in **Figure 3.5**, we successfully transfer the graphene onto TEM grid of $70 \mu\text{m} \times 70 \mu\text{m}$ square area. When we consider the average phonon mean free path of supported graphene ($\sim 90 \text{ nm}$), large Knudsen number $L/\lambda \gg 1$ ensures the diffusive heat transport when heat flux of maximum 1 mW is irradiated. Although the data is not shown, this also justifies the boundary conditions of constant room temperature when solving the heat diffusion equations.

3.4. Summary

In chapter 3, we discuss all of detailed aspects regarding the thermal

conductivity measurement of graphene. The fact that one-atom-thick single layer graphene should be practically supported onto solid substrate justifies the use of supported graphene during the whole experiment. Our advantageous use of ultra-thin 8-nm SiO₂ TEM grid as supporting substrate is known to enhance the measurement reliability. To reduce the ambiguity induced by the different graphene-substrate conformity for the in-plane thermal conductivity of supported graphene, we prepare the two-kinds of graphene with different graphene-substrate separation distance. Note that our samples reflect the effects of Si dopants concentration in affiliated with substrate scattering of vibrational phonon modes (ZA) for the thermal conductivity reduction.

We facilitate Optothermal Raman thermometry, which uses the Raman laser as a heater and temperature prober. Temperature-dependent shift of some distinct peaks in Raman spectrum allows to calibrate the temperature with the variation of incident heat flux. By comparing the experimental temperature and numerically-solved temperature distribution in the supported graphene, we can derive the thermal conductivity of both PG and SiG. All of experimental results are summarized in Figures of chapter 3. We will discuss and elaborate the various aspects of thermal properties alteration induced by the substitutionally doped Si atoms, in chapter 4.

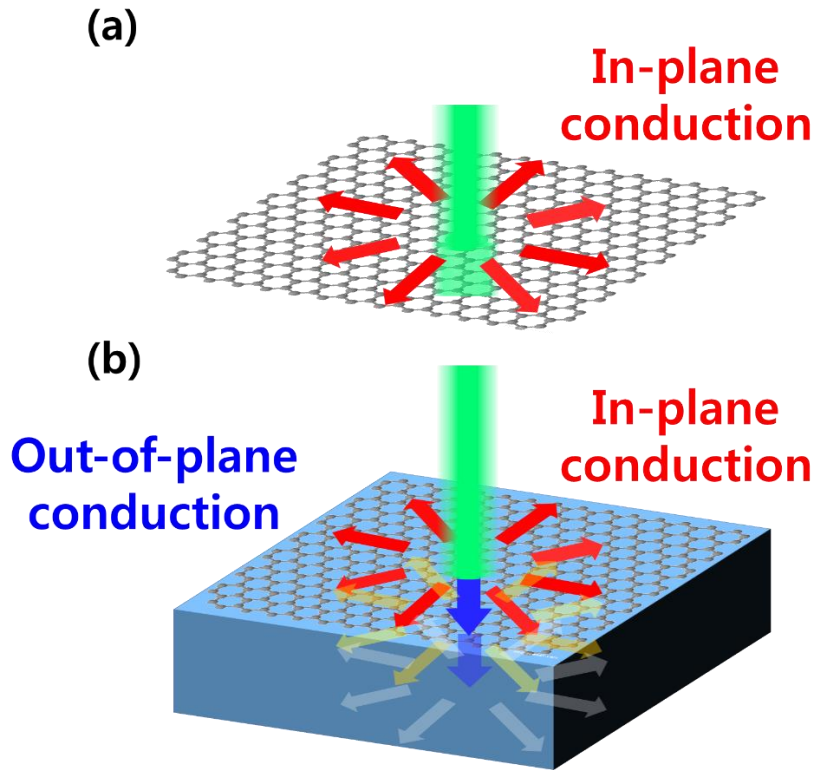


Figure 3.1. Description of the heat dissipation of incident heat flux for the (a) suspended graphene and (b) supported graphene. Additional out-of-plane conduction in supported graphene increases the ambiguity in exclusively deriving the in-plane conduction, which results in the increased measurement uncertainty.

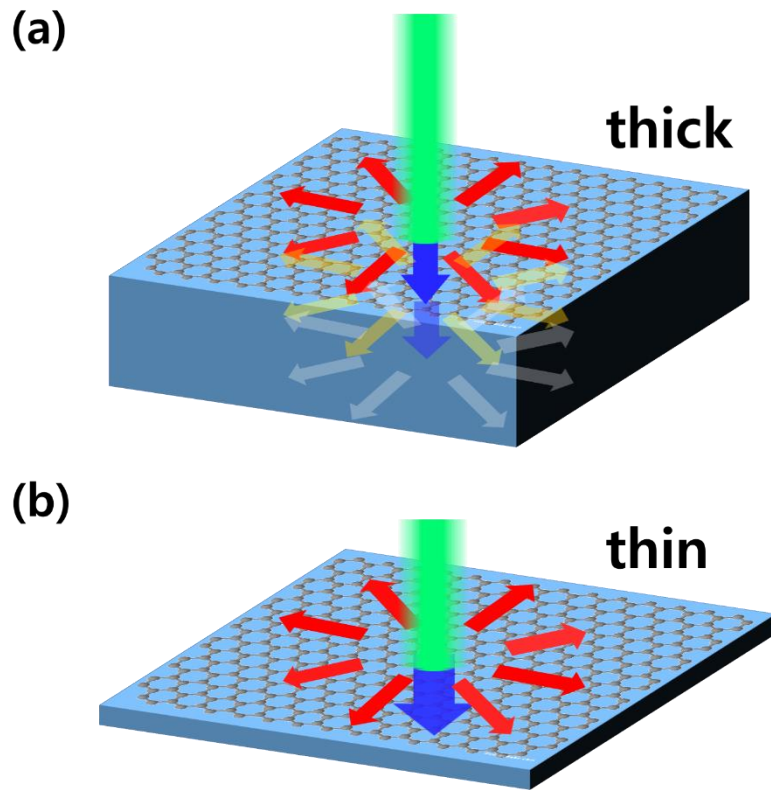


Figure 3.2. Description of the heat dissipation of incident heat flux for the graphene supported onto (a) thick substrate and (b) thin substrate. Decreased out-of-plane conduction enhances the measurement reliability to derive the in-plane thermal conductivity of supported graphene.

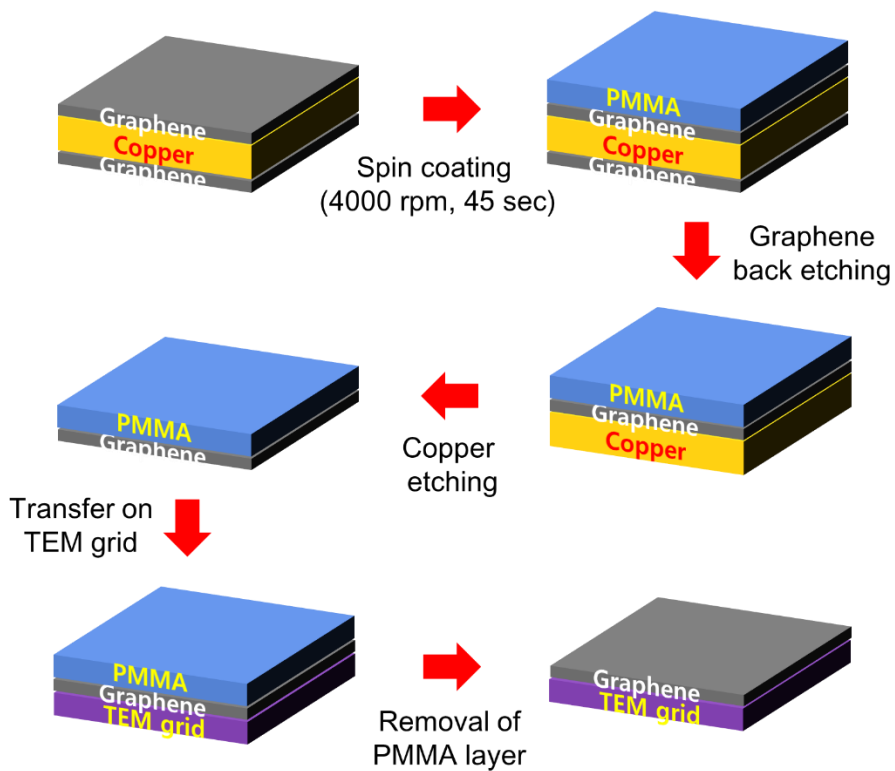


Figure 3.3. Transfer procedure of CVD-synthesized graphene. Both pristine and Si-doped graphene samples were transferred onto 8-nm thin SiO₂ substrate by facilitating the described “PMMA-transfer method”.

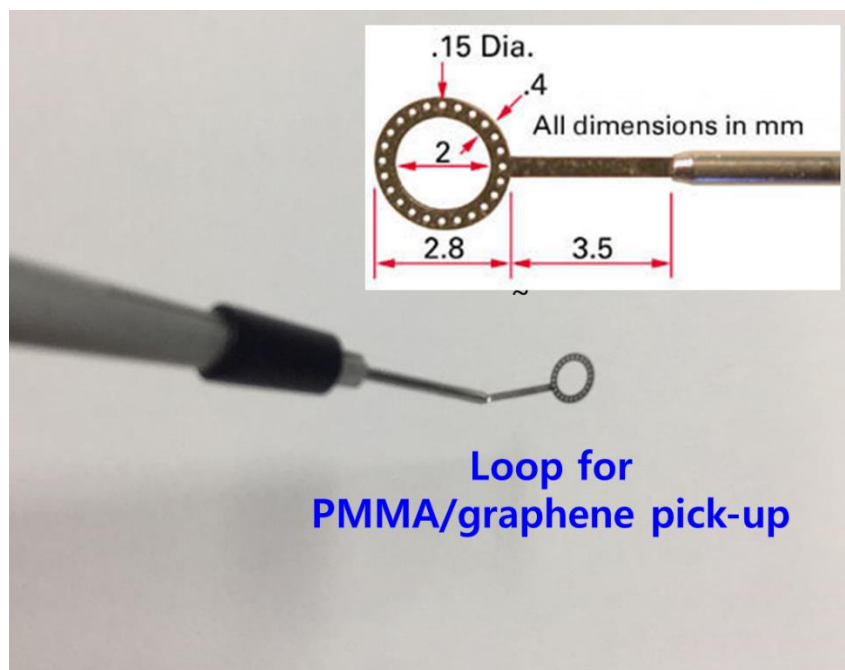


Figure 3.4. Picture of loop for picking up the PMMA/graphene film during the transfer process. About the area of $1\text{mm} \times 1\text{mm}$ graphene can be transferred.

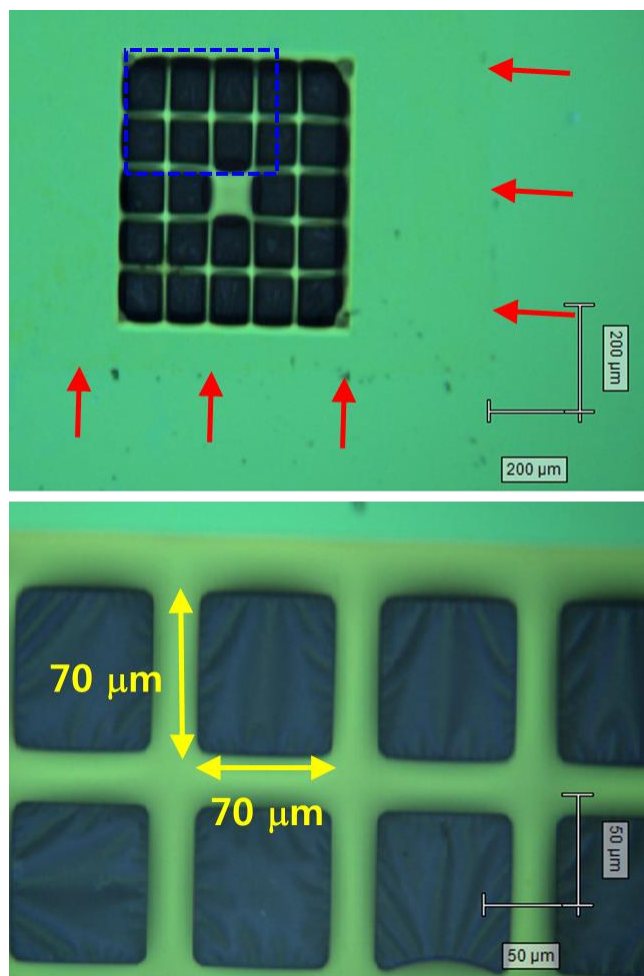


Figure 3.5. Pictures of graphene as transferred onto SiO₂ TEM grid. Red arrows indicate the interfaces of graphene showing the mild optical contrast. Blue box represents the below zoomed-area, which describes well-transferred graphene with minimum wrinkles or chemical residues.

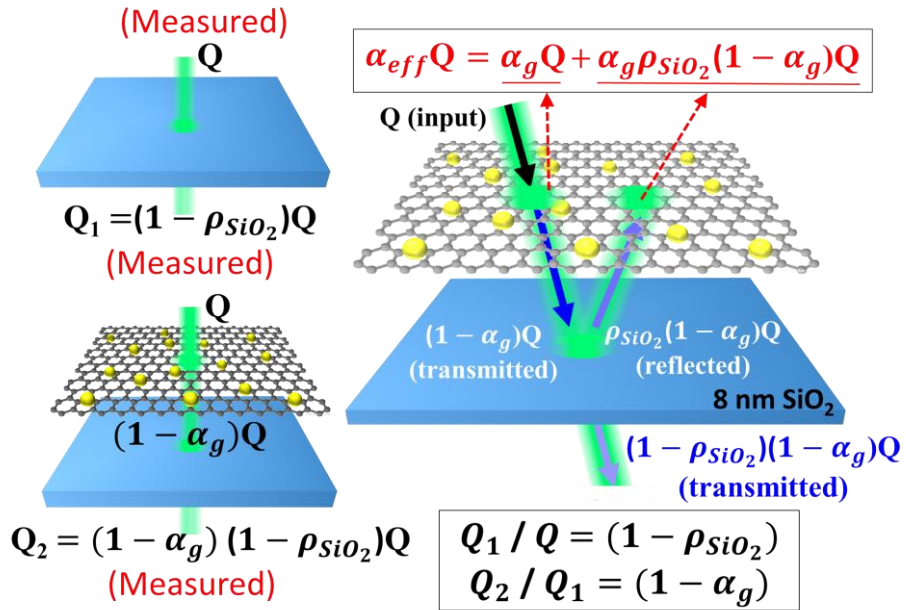


Figure 3.6. The schematic view of the “effective optical absorption” of supported graphene. Both direct absorption and indirect absorption from the reflected laser from underlying substrate are considered. The reduced optical absorption can be attributable to the decreased optical conductivity by the Si dopa

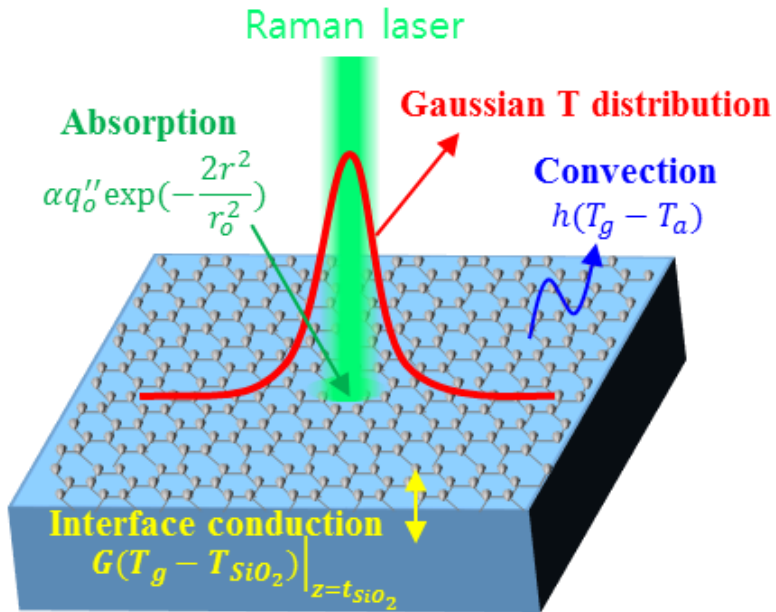


Figure 3.7. Schematic description for the heat diffusion equation considering the optical absorption from incident heat flux, air convection, and conduction through the substrate.

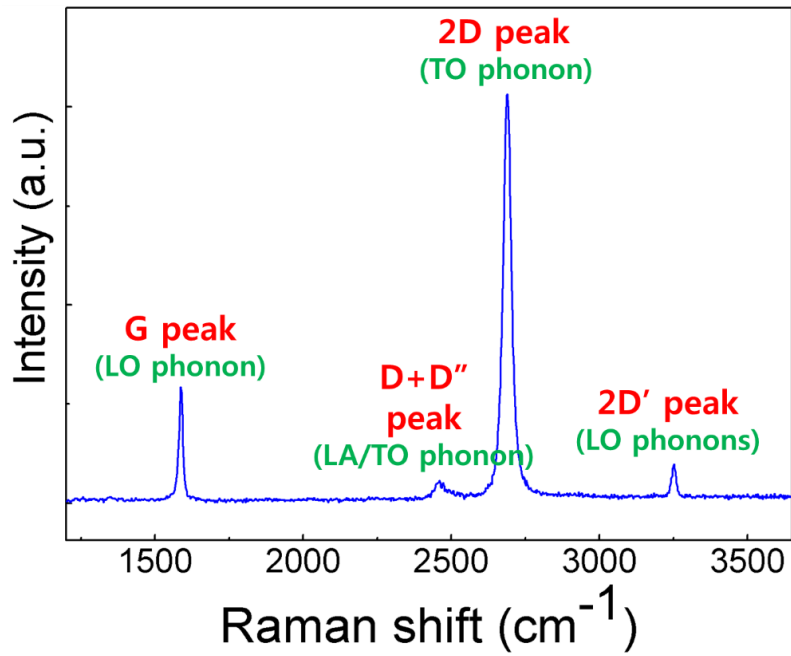


Figure 3.8. Typical Raman spectrum of pristine graphene with different distinct peaks. Each peaks reflect the scattering of optical electrons with corresponding phonons, which enables to probe the temperature of different heat carriers.

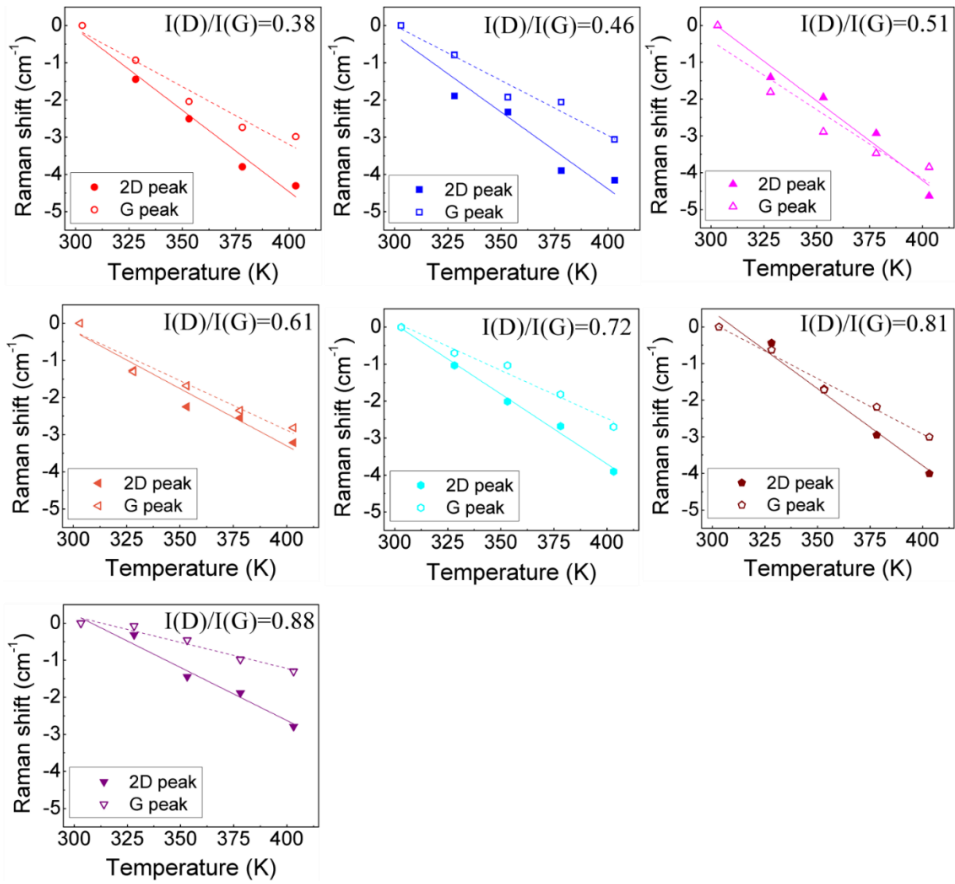


Figure 3.9. Experimental results for the Raman peak shift calibration with the graphene temperature and $I(D)/I(G)$ variation, dw/dT . All of the results indicate that the slope of G peak calibration is lower than that of 2D peak, representing the temperature-sensitivity and measurement reliability of 2D peak calibration.

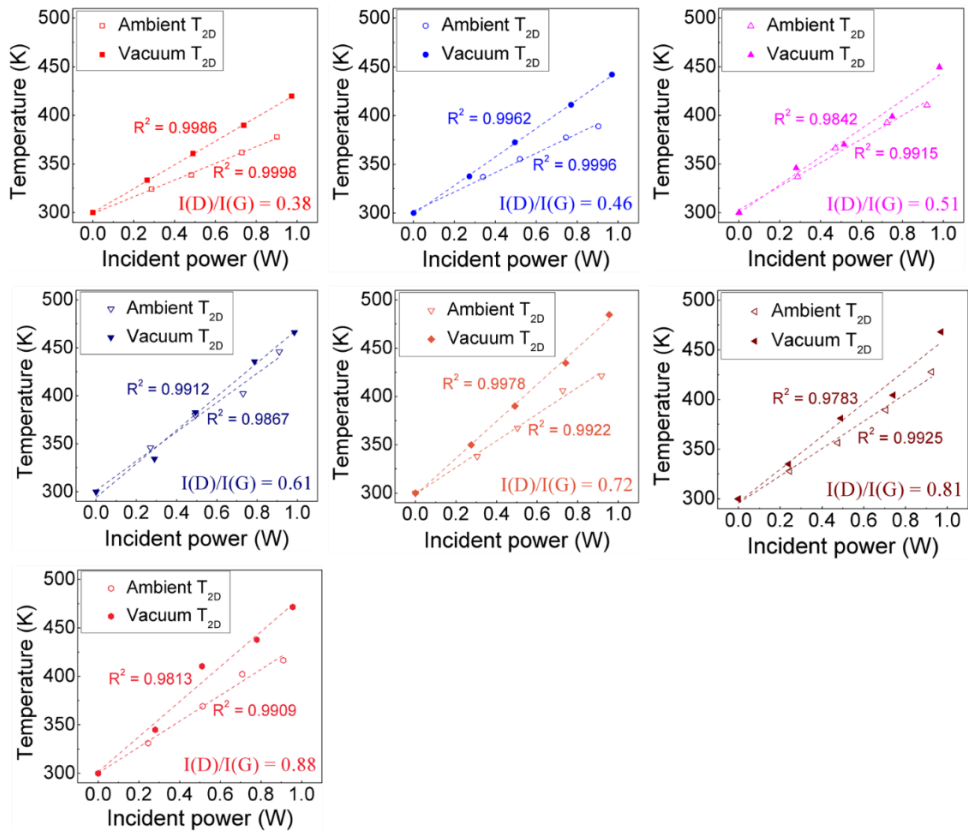


Figure 3.10. Experimental results for the graphene temperature vs. incident heat flux with the facilitation of 2D peak. Ambient-annealed samples and vacuum-annealed samples exhibit the different temperature with the same incident heat flux, indicating the dissimilar graphene-substrate conformity between samples.

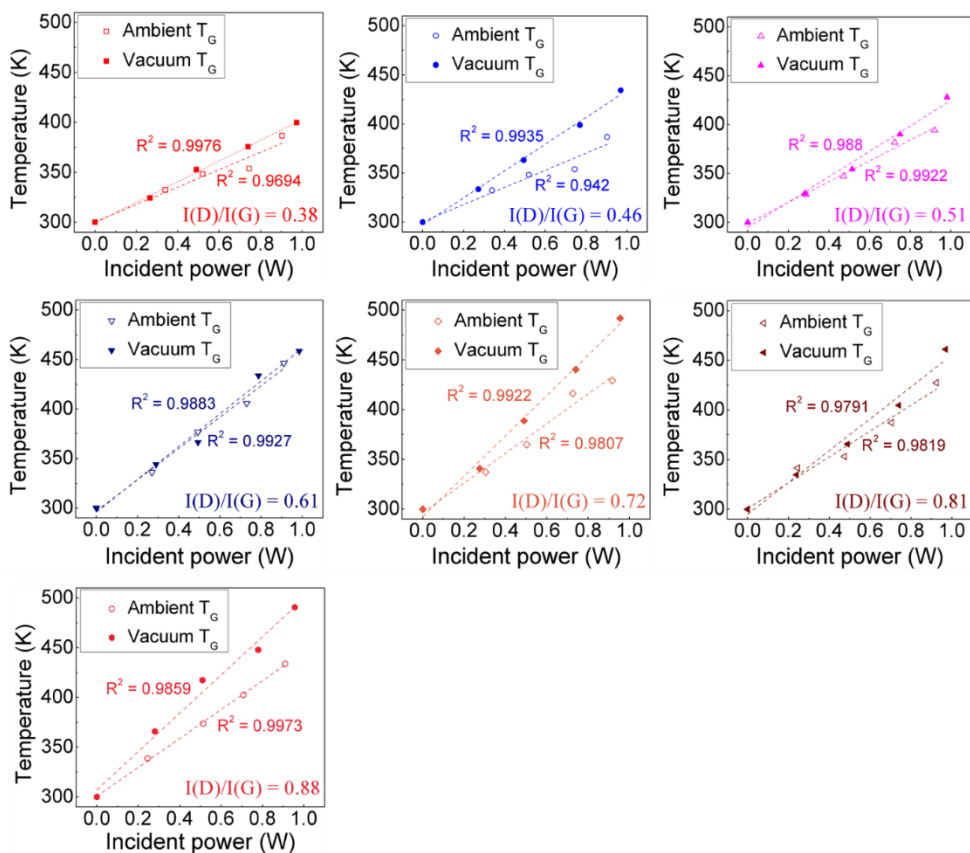


Figure 3.11. Experimental results for the graphene temperature vs. incident heat flux with the facilitation of G peak. Similar difference between ambient-annealed samples and vacuum-annealed samples can be observed when compared to 2D peak calibration results.

| I(D)/I(G) | 2D peak calibration | | G peak calibration | |
|-----------|---------------------------------|----------------------------|------------------------------|----------------------------|
| | dw_{2D}/dT (cm^{-1}/K) | dT/dQ_{in} (K/mW) | dw_G/dT (cm^{-1}/K) | dT/dQ_{in} (K/mW) |
| 0.38 | -0.0438 | 85.759 | -0.0311 | 61.738 |
| 0.46 | -0.0413 | 99.445 | -0.0296 | 86.014 |
| 0.51 | -0.0439 | 121.57 | -0.0374 | 106.24 |
| 0.53 | -0.0311 | 126.67 | -0.0232 | 105.87 |
| 0.61 | -0.0308 | 170.08 | -0.0267 | 187.67 |
| 0.72 | -0.0378 | 142.8 | -0.0261 | 149.34 |
| 0.81 | -0.0421 | 137.14 | -0.0303 | 131.35 |
| 0.88 | -0.0293 | 130.54 | -0.14 | 154.86 |

Table 3.1. Summarized results for the temperature calibration and temperature vs. incident heat flux with the I(D)/I(G) variation.

Chapter 4

Thermal properties of Si-doped graphene

4.1. Thermal conductivity reduction

4.1.1. Si dopants concentration effect

Our main concern is the thermal conductivity of supported Si-doped graphene compared to pristine graphene, which reflects the effects of Si dopants on thermal conductivity reduction. The measurement with the $I(D)/I(G)$ variation (from 0.38 to 0.88) allows to elaborate the Si dopants concentration effect. In chapter 3, we already estimated the corresponding Si dopants concentration range from 1.43 % to 3.13 %. By following the detailed procedure described in chapter 3, we derive the thermal conductivity of Si-doped graphene as shown in **Figure 4.1, 4.2** and **Table 4.1** with both 2D peak and G peak calibration. Note that all of results in **Figure 4.1, 4.2** and **Table 4.1** indicate the thermal conductivity at (near) room temperature, which is attributable to the linear correlation between the incident heat flux and Raman peak shift (dw/dQ). In chapter 4.1.1, we only concentrate on the thermal conductivities of graphene annealed in ambient pressure (ambient-annealed

samples).

Here, we regard the effective thermal conductivity of ambient-annealed SiG as the thermal conductivity measured at the average I(D)/I(G) value (~0.61 which estimated to be 1.91% Si doping concentration) with 2D peak calibration, 76.17 W/mK. This effective thermal conductivity of supported SiG shows nearly two order-of-magnitudes reduction from the suspended PG case of 2663 W/m·K[9] and nearly one order-of-magnitude reduction from the supported PG of 900.18 W/mK[35].

Assuming the independent contribution of each phonon scattering mechanisms, total phonon scattering rate (τ) from Matthiessen's rule can be described as

$$\tau_{PG}^{-1} = \tau_{int}^{-1} + \tau_{GB}^{-1} + \tau_{sub}^{-1}$$

$$\tau_{SiG}^{-1} = \tau_{int}^{-1} + \tau_{GB}^{-1} + \tau_{sub}^{-1} + \tau_{Si}^{-1}$$

where the τ_{int}^{-1} is the phonon scattering rate induced by the intrinsic properties of graphene including normal and Umklapp scattering, τ_{GB}^{-1} by the grain boundary scattering in CVD-synthesized graphene, τ_{sub}^{-1} by the underlying substrates scattering, and τ_{Si}^{-1} by the incorporated Si dopants. The additional phonon scattering mechanisms in SiG can be mainly

attributable to the increasing phonon scattering rate by Si dopants, τ_{Si}^{-1} .

The phonon scattering rate by the presence of substitutional atoms can be described by $\tau_{Si}^{-1} = V_0(\omega^3/v^2)\Gamma$, [7,13,15] where V_0 is the volume per atom, ω is the phonon frequency, v is the phonon group velocity, and Γ is the phonon scattering strength. Here, the average phonon group velocities are known to be nearly identical, i.e., $(v_{SiG}/v_{PG}) = (M_{PG}/M_{SiG})^{1/2} = 0.9875$, [15,84]. Therefore, the phonon scattering rate by foreign atoms is a strong function of the phonon scattering strength Γ , which is known to be proportional to the square of mass difference between the dopant and the host atom, i.e., $\Gamma \sim (\Delta M)^2$. When compared to previous study, the excessively high phonon scattering strength of Si dopants ($\Gamma \sim 256$) results in the order-of-magnitude reduction by 90% for 1.91% Si doping concentration, while the ^{13}C isotope doping [15] in ^{12}C of suspended case provides $\Gamma \sim 1$ and results in only 27% reduction of thermal conductivity at a comparable concentration of 1.1 at.%. Note that our SiG samples show the order-of-magnitude reduction even under simultaneous contribution of substrate scattering, which possibly reduces the relative contribution of other scattering mechanisms (Si dopants) on total phonon scattering rate. This large mass difference of Si dopants also represent the larger reduction compared to other substitutional dopants with small mass difference, such as N and B (**Table 4.2**).

Note that we assumed the substitutional Si dopants are similarly treated as isotope defects and did not account for possible thermal conductivity alteration caused by the bond strength change in Si–C bonding.[85] According to the second-order perturbation theory[34], total phonon scattering rate change by point defects should be described as below

$$\tau_{Si}^{-1} \propto (S_1^2 + (S_2 + S_3)^2)$$

which includes the mass difference with host atoms and point defects (S_1), bond strength change (S_2), and bond length change induced by point defects incorporation (S_3). Note that S_1 represents the phonon scattering contribution of τ_{Si}^{-1} , while S_2 and S_3 represent the contribution of τ_{int}^{-1} . Previous theoretical prediction demonstrated the effects of both bond strength and length alteration on thermal conductivity reduction in N-doped graphene. In their study, graphitic nitrogen doping showed about 61% reduction, while pyridinic doping represented nearly 89% reduction both compared to pristine suspended graphene.[18] This enhanced thermal conductivity reduction can be attributable to the significant bond properties alteration (S_2 and S_3) near nitrogen dopants. As described in above paragraph, we only consider the mass difference term (S_1) to explain the effects of Si dopants on thermal

conductivity reduction. Nevertheless, we believe that it does not substantially contradict our discussion to explain that large mass difference between C and Si can be majorly attributed to the thermal conductivity reduction caused by intentionally substituted Si dopants.

All of the measured thermal conductivities show the progressive decrease with the Si dopants concentration ($\sim I(D)/I(G)$). At the maximum Si doping concentration ($I(D)/I(G) \sim 0.88$, 3.13 % Si doping concentration), thermal conductivity is reduced to 96.4 W/mK (2D peak calibration) and 79.469 W/mK (G peak calibration). With the increase of doping concentration, thermal conductivity reduction is observed to be saturated. The similar behavior of thermal conductivity reduction was demonstrated in previous experimental studies on other suspended defected graphene under e-beam or plasma irradiation.[10,13] This is because long-wavelength phonons, which significantly contribute to the heat propagation, are known to become less affected by additional defects with the increase of defects concentration.[13] Closely packed introduced defects after certain doping concentration do not effectively scatter the long-wavelength phonons compared to sporadically distributed defects at the low concentration.

Therefore, we believe that the certain critical defects concentration N_c , where the thermal conductivity reduction effectively stops, might be the

function of inter-defect distance (d) to average phonon mean free path (λ) ratio, λ/d . The average phonon mean free path for supported graphene on SiO₂ is known to be 90 nm.[86] Our SiG shows the critical defects concentration at the I(D)/I(G) \sim 0.61, which can be corresponded to the spatially averaged Si dopants concentration, 1.91 at.%. Considering the carbon number density in graphene ($3.82 \times 10^{15} \text{ cm}^{-2}$), the inter-defects (Si dopants) distance at the critical defects concentration for our sample could be estimated from the equation of $d = 1/(\pi N_c)^{1/2} = 1/(\pi \times 0.0191 \times 3.82 \times 10^{15} \text{ cm}^{-2})^{1/2} = 0.66 \text{ nm}$ and this gives the $\lambda/d \sim 136$.

Two previous studies facilitate the suspended graphene which has the longer phonon mean free path (775 nm)[4] than supported graphene. One previous study determined the critical defect concentration as $1.5 \times 10^{11} \text{ cm}^{-2}$ under E-beam irradiation.[13] Another study demonstrated that thermal conductivity reduction effectively saturated near 0.1 % of defect concentration under oxygen plasma treatment.[10] Inter-defects distance is derived by following the same procedure and **Table 4.3** summarizes the comparison of the λ/d between samples experimentally observed the critical defects concentration. We found that λ/d ratio for our SiG samples is within the range of previous studies with minor variation. The difference can be attributable to the (1) distinction in the phonon scattering strength

between different types of defects, (i.e. vacancy defects and Si dopants), and the lack of criteria for the determination of N_c (i.e. specific value of $d\kappa/dN$ at N_c). In addition, unavoidable uncertainty for the Optothermal Raman thermometry can be minorly attributed to the observed difference in λ/d ratio. Note that supported graphene requires about two order-of-magnitude much defects concentration for the saturated thermal conductivity reduction. Further studies regarding the determination of critical defects concentration for defected graphene with specific conditions will be helpful to manipulate the heat spreading efficiency in graphene.

4.1.2. Graphene-substrate conformity effect

As mentioned above, wet transfer process onto solid substrate inevitably induces some suspension of graphene, which can be attributable to the nanoscale roughness of underlying substrate. Our previous studies already demonstrated that thermal annealing efficiently enhances the graphene-substrate conformity and enables thermal conductivities to reflect the substrate effects. Enhanced graphene-substrate conformity indicates the increase of substrate ZA phonon scattering which is known to significantly reduce the in-plane thermal conductivity. As mentioned in chapter 3.2.3, we individually measure the thermal conductivities of ambient-annealed SiG

(intermediate conformity) and vacuum-annealed SiG (maximum conformity) to remove the possible ambiguity from the dissimilar contribution of substrate on phonon scattering, τ_{sub}^{-1} . Definitely we compare the thermal conductivities with supported pristine graphene with corresponding thermal annealing conditions.

As shown in **Figure 4.1, 4.2 and Table 4.1**, vacuum-annealed SiG shows the notably reduced thermal conductivities compared to those of ambient-annealed SiG. This can be attributable to the enhanced graphene-substrate conformity in vacuum-annealed SiG samples. Intercalated water molecules in supported graphene are efficiently removed when thermally annealed in high vacuum.[35] This decreases the graphene-substrate separation distance and successively enhances the graphene-substrate conformity, finally increasing the scattering rate of the propagating phonons in graphene. We can conclude that still the importance of graphene-substrate conformity on the in-plane thermal conductivities holds for the case of substitutionally doped graphene.

From the Metthiessen's rule, the difference in τ_{sub}^{-1} between the ambient-annealed SiG and vacuum-annealed SiG may affect the relative contribution of Si dopants on total phonon scattering. Similar alterations in relative contribution of specific phonon scattering mechanisms were already examined, decreasing temperature dependence in supported graphene or

defected graphene, for instance.[9,14,35,41] When the measured thermal conductivities are fitted with $I(D)/I(G)^{-\alpha}$, we found the lowered α of vacuum-annealed SiG when compared to that of ambient-annealed. For the 2D peak and G peak calibration, α decreases from 0.906 to 0.851 and from 1.568 to 1.27, respectively. This indicates that thermal conductivity dependence on Si dopants concentration is reduced when vacuum-annealed, which can be attributable to the relatively enhancement of substrate scattering contribution (τ_{sub}^{-1}), in spite of the only slight difference between ambient and vacuum conditions. On the other hand, the slight difference of α can also interpreted as the dominant contribution of Si dopants phonon scattering comparable to the substrate scattering.

4.1.3. Grain size effect

The nucleation growth mechanism of CVD graphene samples are inherently polycrystalline, which scatters the propagating energy carriers at the grain interfaces (grain boundary). Phonon scattering rate at the grain boundary τ_{GB}^{-1} enhances when the grain sizes decrease attributing to the increase in nucleation density. Intuitively, this grain boundary scattering rate shows their significance only when the grain sizes are decreased comparable to the average phonon mean free paths, as demonstrated by previous

experimental researches using suspended graphene.[9,25] This is because the propagating phonons tend to be scattered at the grain boundary before scattered by another phonons, only when the grain sizes are comparable to the average phonon mean free path.

Similarly, in spite of the inherent polycrystalline growth of CVD graphene,[9,25] previous theoretical analysis in supported graphene already demonstrated that grain boundaries significantly affects thermal conductivity only when the grain sizes are smaller than average phonon MFP (~ 90 nm) (**Figure 4.3**).[8,86] As shown in chapter 2.5.4, our SiG samples exhibit the order-of-magnitude larger grain sizes ($\sim 1 \mu\text{m}$), indicating the negligible effect of grain boundary scattering on the thermal conductivity reduction. Therefore, phonon scattering associated with grain boundaries is not main concern in terms of thermal conductivity reduction of SiG compared to PG.

4.1.4. Doping inhomogeneity effect

Si dopants do not exhibit the perfect uniform distribution along the graphene lattices, which is attributable to the chemical probability dependence of Si-C bonding incorporation. Although our Optothermal Raman thermometry locally probe the thermal conductivities of graphene samples, Si dopants distribution near heating area essentially influences the

measured thermal conductivities because of inevitable temperature gradient near probe point. Therefore, we calculate the effective Raman probing area under temperature gradient, thermal activation boundary (TAB), and confirm the dopants distribution ($\sim I(D)/I(G)$) (**Figure 4.4**). Uniform dopants distribution inside the TAB means that measured thermal conductivities do not hold the possible uncertainties induced by non-uniform dopants distribution.

The radius of TAB, r_{TAB} is calculated based on the criterion for TAB, $(T_{TAB} - T_a)/T_m \approx 0.02$, where the T_{TAB} , T_a , and T_m are the temperature at TAB, ambient temperature (300 K), and the measured temperature of graphene under maximum laser irradiation (power of 1mW), respectively. For each regions with specific $I(D)/I(G)$, Gaussian temperature distribution calibrated from 2D peak correlation for vacuum-annealed SiG is facilitated to derive the r_{TAB} . At the TAB, all the regions show the temperature enhancement below 10 K with the radius of shorter than 2 μm (**Table 4.4**). When we draw the TAB at the measured spots in Raman mapping (**Figure 4.5**), we found the relatively uniform distribution of Si dopants within TAB. This indicates that our derived thermal conductivities contain negligible uncertainties possibly stemming from the doping inhomogeneity inside the examination regions.

4.2. Temperature independence of thermal conductivity

4.2.1. Si dopants effect

In chapter 4.1.1, all of the thermal conductivities are measured at room temperature, which were derived from the Q vs. T linear correlation. On the other hand, individual derivation of thermal conductivities from the each Q vs. T correlation results enables to obtain the temperature dependence of SiG thermal conductivity with Si doping concentration variation. Temperature-dependent thermal conductivities are plotted in **Figure 4.6**, for the case of 2D peak calibration based ambient-annealed samples. This figure describes the negligible temperature dependence of SiG for the temperature range from 300 K to 500 K (see **Table 4.5**). In the total phonon scattering rate from Metthiessen's rule, intrinsic phonon scattering term τ_{SiG}^{-1} includes the temperature-dependent Umklapp scattering mechanisms, which is the main contribution on the in-plane thermal resistance in graphene.

In case of PG, the phonon-phonon Umklapp scattering increases with a temperature increase due to the increased phonon population and this is generally well represented by the negative temperature dependence of thermal conductivities.[7,9] When the Si dopants are incorporated into PG lattices, additional phonon scattering contribution by Si dopants arises, as described in chapter 4.1.1. Therefore, the prevailing Si dopants-phonon

scattering will lower the relative contribution of phonon-phonon scattering and successively the temperature dependence of thermal conductivities can also be reduced.[12,21] In addition, suppression of long-wavelength phonons, which importantly contribute to the whole in-plane conduction but show significant temperature dependence, can be attributed to the suppressed temperature dependence. Well-fitted linear correlation between the temperature enhancement and incident heat flux for other cases of vacuum-annealed samples with G peak calibration also indicates the similar temperature independence of thermal conductivities (see **Figure 3.10 and 3.11**). Consistent findings have been demonstrated in point-defected graphene,[14] where the temperature dependence of thermal conductivity is found to be weakened with the increase in vacancy defects concentration.

4.2.2. Graphene-substrate conformity effect

Similar with above elaboration, enhanced graphene-substrate conformity (τ_{sub}^{-1}) can conceal the effects of temperature-dependent Umklapp scattering included in intrinsic graphene scattering rate of τ_{int}^{-1} . Previous study demonstrated that temperature dependence of pristine graphene thermal conductivity becomes weakened with repetition of thermal annealing, which allows to enhance the graphene-substrate conformity.[35] Direct

measurement of thermal conductivities after transfer shows the temperature dependence comparable to the suspended case. However, when the number of thermal annealing exceeds five times, temperature dependence is significantly reduced and vacuum annealing shows further suppression (**Figure 4.7**). Similarly, our ambient-annealed SiG and vacuum-annealed SiG exhibit the negligible temperature dependence. Along with the Si dopants, long-wavelength phonons suppression by underlying substrate can be attributed to the observed temperature dependence.

4.3. Non-equilibrium errors in measurement data

4.3.1. Why non-equilibrium problem arises?

Non-equilibrium error in thermal conductivity measurement scheme indicates the possible uncertainties induced by the non-equilibrium state between different polarized phonons. Generally thermal conductivity measurement requires the precise derivation of temperature enhancement of materials under specific heat flux. Therefore, if we measure the temperature of specific phonons that show the deviated temperature with other phonons, thermal conductivity can be under- or over-estimated while solving the heat diffusion equation. According to previous theoretical and experimental studies[31,76], non-equilibrium error problem arises when Optothermal

Raman thermometry is facilitated to measure the in-plane thermal conductivity of suspended graphene. The main reasons for the non-equilibrium error in Optothermal Raman thermometry can be summarized into three aspects; (1) inherent weak coupling between energy carriers, (2) Large length mismatch between heating spot size and average phonon MFP, and (3) unbalanced contribution of different phonons on in-plane thermal conduction.

Two atoms in unit cell gives the six phonons in graphene, three optical phonons and three acoustic phonons. Previous theoretical study[76] used the simulation models based on the first principles density functional theory and a multi-temperature model to indicate that Raman laser-excited hot electrons are mainly relaxed by the optical phonons. However, the weak coupling between the optical phonons and acoustic phonons makes it hard to result in the sufficient scatter between phonons, which leads to the strong non-equilibrium. Perturbation theory based calculation in conjunction with phonon-phonon scattering rates also represent the weak coupling between acoustic phonons themselves, especially for flexural acoustic (ZA) phonons. Therefore, non-equilibrium error can be reflected in measurement data when we measure the temperature of specific phonons that show the weak coupling with other energy carriers.

As mentioned in chapter 1, suspended graphene shows exceptionally long average phonon MFPs 775 nm, attributing to strict momentum conservation requirement in 2D materials along with strong bond strength in sp² C-C. On the other hand, local thermal conductivity measurement in Optothermal Raman thermometry heats the spot size of about 218 nm in radius (100x objective lens for 514 nm wavelength laser, in our case), much shorter than average phonon MFPs. This length mismatch do not ensure the enough space to interact between phonons so that they do not sufficiently scatter each other to reach the thermal equilibrium before they propagate out of heating spot. Especially considering the dominant contribution of long MFPs phonons (> 775 nm) on thermal conduction, insufficient heater size cannot provide the required thermalization length for phonons equilibrium in graphene.

Finally, unequal contribution of different phonons on thermal transport can enlarge the non-equilibrium error in thermal conductivity derivation. Optical phonons generally show the lowered group velocity compared to acoustic phonons for most materials, less contributing to the thermal conductivity. In case of graphene, it is well-accepted that ZA phonons are dominantly contribute to heat transport up to 85% among the three acoustic phonons (LA, TA, and ZA).[6,41] This can be explained by the large density of states (DOS) and symmetry-based strict selection rule that suppresses the anharmonic

phonon-phonon scattering.[87] However, as mentioned above, ZA phonons exhibit the weakest coupling with the hot electrons and optical phonons, representing the most deviated temperature with other energy carriers. This indicates that probing the temperature of energy carriers other than ZA phonons can lead to the amplified non-equilibrium error in measurement data. Previous theoretical predictions already demonstrated that simulation under the assumption of equal contributions of all acoustic phonons reduced the underestimation factor from 2.6 to 1.8.[76]

Unfortunately, we cannot probe the exact temperature of ZA phonons, the most dominant heat carrier in suspended graphene, by facilitating the Optothermal Raman thermometry. As mentioned above, Optothermal Raman thermometry calibrates the graphene temperature with the peak shifts in Raman spectrum, which reflect the temperature of specific phonons (**Figure 3.8**). Because Raman scattering indicates the inelastic scattering between the incident photons and optical electrons, most Raman peaks represent the temperature of optical phonons in graphene, which are the most coupled energy carriers with optical electrons. Therefore, probing the temperature of minor contributor (optical phonons) in Optothermal Raman thermometry can be the most important reason for possible non-equilibrium error. Note that reduced R^2 in Lorentzian of Raman peaks can be attributed to the inadequate

strategy of enlarged heater size to suppress the non-equilibrium error.

4.3.2. Non-equilibrium error in Si-doped graphene

To access the non-equilibrium error in Si-doped graphene, we compare the calibrated temperature T_{2D} and T_G , where T_{2D} mostly represents the phonon temperature in the vicinity of the K point (TO phonons, 2D peak) and T_G represents the phonon temperature at the Brillouin-zone center (LO phonons, G peak).[66] We conveniently define the normalized discrepancy of the two calibrated temperatures for the two different phonons as $[\frac{|T_{2D}-T_G|}{\text{Max}(T_{2D}:T_G)} \times 100]$, implying the quantitative measurement of the non-equilibrium error (**Figure 4.8**). We found that the discrepancies due to the possible non-equilibrium effect are less than 6% for all tested I(D)/I(G) ratios range, and they show the gradual decrease with increasing I(D)/I(G) (~Si dopants concentration). The possible breakdown of strict momentum conservation requirement in defected graphene can lead to the stronger coupling between energy carriers compared to defect-free graphene, resulting in the reduced local non-equilibrium error. In addition, substitutionally doped Si atoms can drive more rapid relaxation and shorten the required thermalization length, which is attributable to the reduced phonon MFPs (**Figure 4.9**). The shorter MFPs under the higher dopant density can further

shorten the relaxation time to reach equilibrium even more quickly. This trends, decreasing non-equilibrium error with the increase of Si dopants concentration, are distinctly observed in the derived thermal conductivities as shown in Figure (**Figure 4.10 and 4.11**). Almost the same thermal conductivities are derived when Si dopants concentration is more than 2 %, indicating the significantly suppressed non-equilibrium error.

As mentioned above, dominant contribution of ZA phonons on total phonon conduction (up to 85%) in suspended graphene can be attributed to the one of main reason for the non-equilibrium error.[37,41,75,87] This is because ZA phonons show the weakest coupling with the optical phonons, whose temperatures are calibrated from Raman G peak and 2D peak. However, in case of our supported graphene, where the underlying substrate supports the one-atom-thick graphene, out-of-plane phonons vibrational modes are known to be almost completely suppressed by the substrate. Substrate-induced disorder possibly and the breakdown of reflection symmetry possibly reduces the ZA phonons lifetime in supported graphene.[37] Likewise the reduced non-equilibrium error in the case of equal contribution of three acoustic phonons, suppression of the weakest coupled ZA phonons in supported graphene can be attributable to the observed minor non-equilibrium error. This can be evidenced by the slightly decreased non-

equilibrium error in vacuum-annealed samples compared to ambient-annealed case, where the graphene exhibits the saturated conformity with the substrate. Therefore, we believe that non-equilibrium error does not prevail at least in our measurement data for supported Si-doped graphene.

4.4. Summary

In chapter 4, we discuss the thermal properties of Si-doped graphene as supported on SiO₂ substrate. When the Si dopants are incorporated into defect-free graphene, thermal conductivity drastically reduces with the increase of Si doping concentration. Even with the 2% Si dopants, order-of-magnitude reduction is observed for supported graphene, and two order-of-magnitude reduction for suspended graphene. Large mass difference (ΔM) between the host carbon atoms and silicon dopants can be mainly attributable to the observed thermal conductivity reduction, which is also evidenced by the larger reduction in SiG compared to other light dopants such as N or B. Also we found that critical defects concentration can be the function of inter-defect distance to average phonon MFP ratio, which needs further study. Our systematic consideration shows that the effects of graphene-substrate conformity, grain sizes, and the doping inhomogeneity are not the significant concern in the thermal conductivity reduction in Si-doped graphene.

Incorporated Si dopants also have influence on the temperature dependence of thermal conductivity and non-equilibrium between phonons in graphene. Reduced temperature dependence of thermal conductivity in SiG can be attributed to the relatively lowered contribution of phonon-phonon Umklapp scattering compared to arising Si-phonon scattering, and suppressed long wavelength phonons that represent the significant temperature dependence. We found that non-equilibrium error, which attacks the measurement reliability of Optothermal Raman thermometry, tends to be reduced when the Si dopants enhances scattering rate for thermal equilibrium between phonons by reducing the phonon MFPs and breaking the reflection symmetry of graphene. In chapter 5, relative comparison between thermal conductivity reduction and electrical conductivity reduction will shed the light on the possibility of Si-doped graphene as a thermoelectric materials.

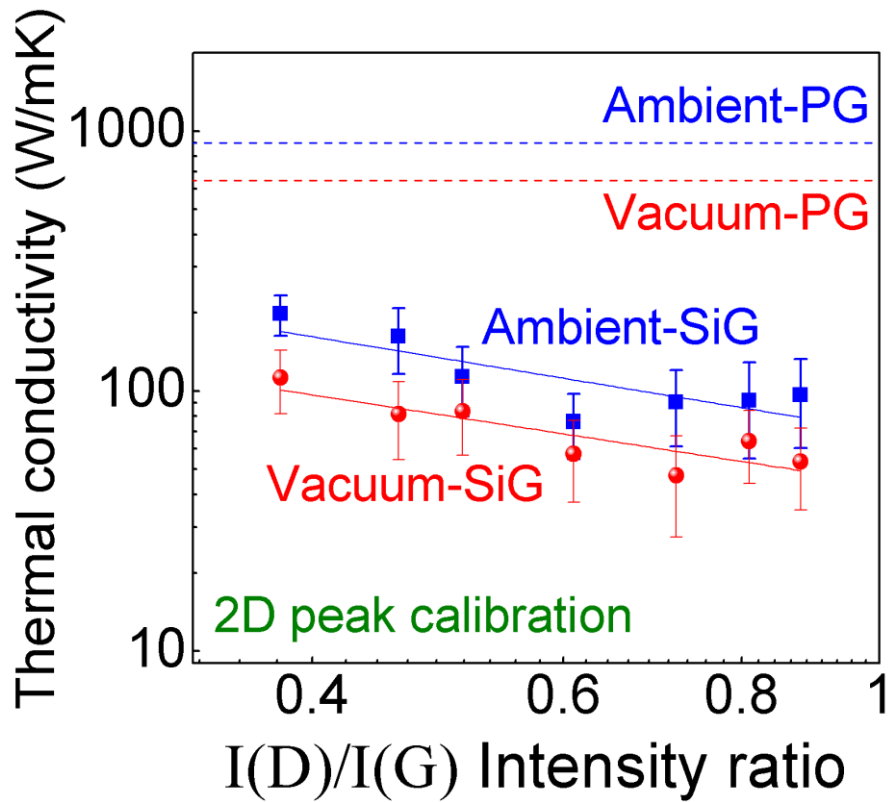


Figure 4.1. Thermal conductivities of SiG with the increase of I(D)/I(G) intensity ratio based on 2D peak calibration. More than 2% Si dopants concentration provides the order-of-magnitude reduction compared to supported pristine graphene.

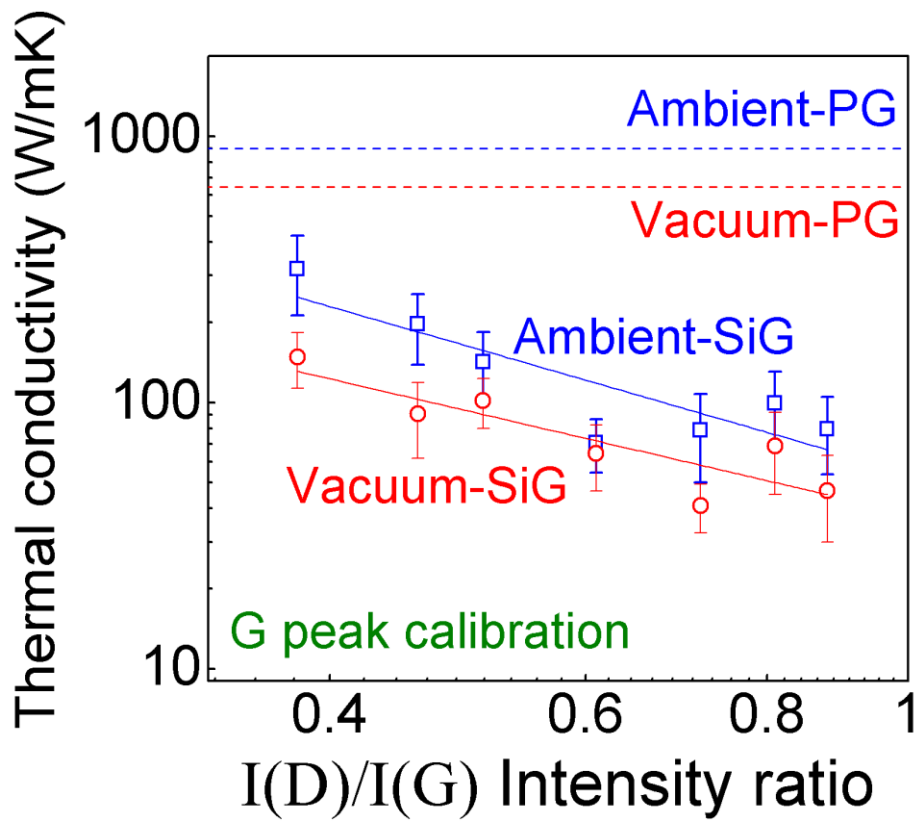


Figure 4.2. Thermal conductivities of SiG with the increase of I(D)/I(G) intensity ratio based on G peak calibration. Similar order-of-magnitude reduction can be observed.

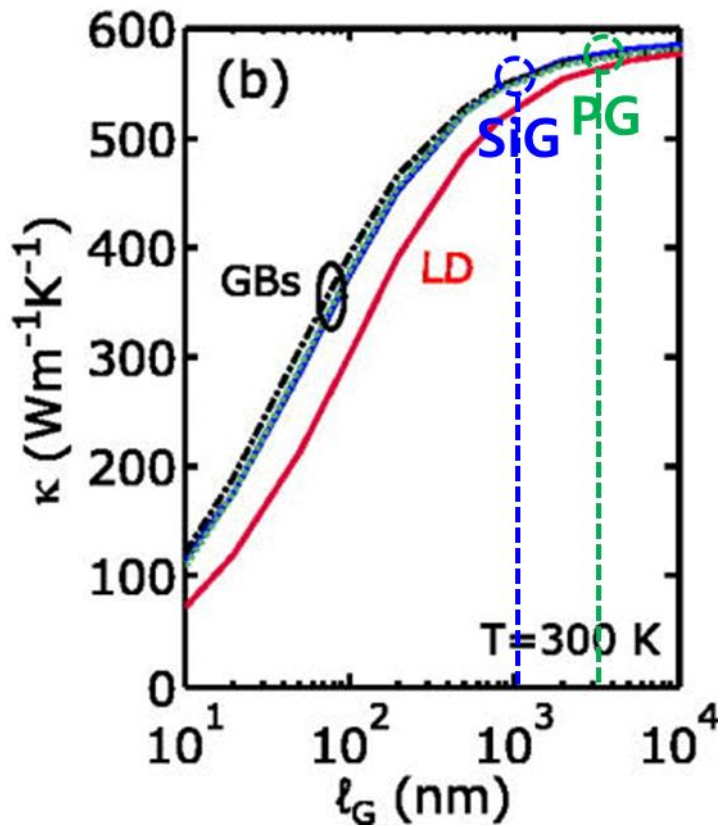


Figure 4.3. (From Y. Serov et al, 2013, *APL*) Theoretical predictions on thermal conductivity of supported graphene with the grain sizes (GB) and line defects (LD). The effects of grain boundaries on thermal conductivity reduction can be negligible when the grain sizes are longer than average phonon MFPs of supported graphene (~ 90 nm).

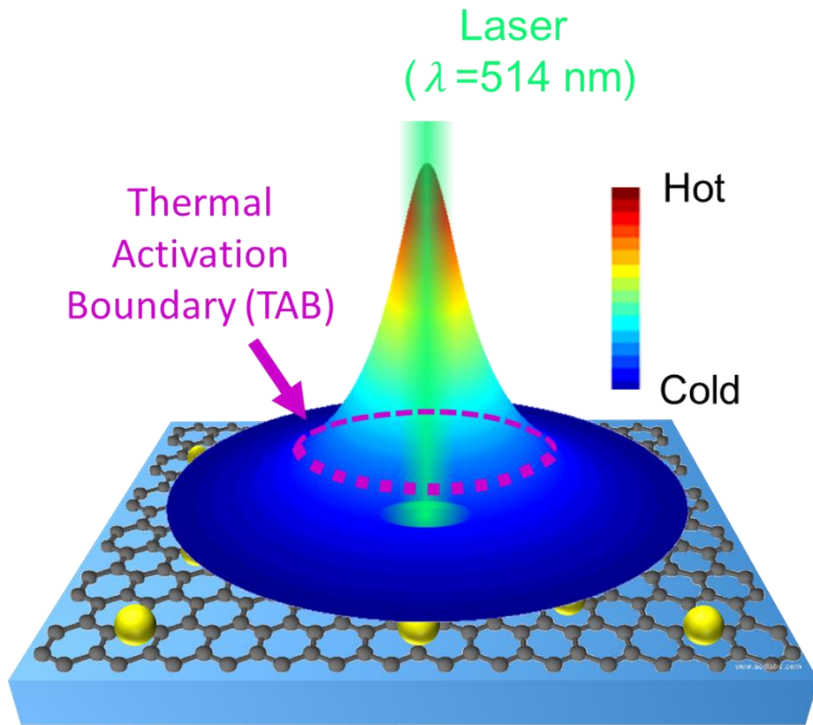


Figure 4.4. A schematic description of the thermal activation boundary (TAB). Dopants distribution within the TAB determines the possible uncertainties induced by doping inhomogeneity, attributing to the large temperature gradient inside the TAB. Yellow atoms indicate the Si dopants.

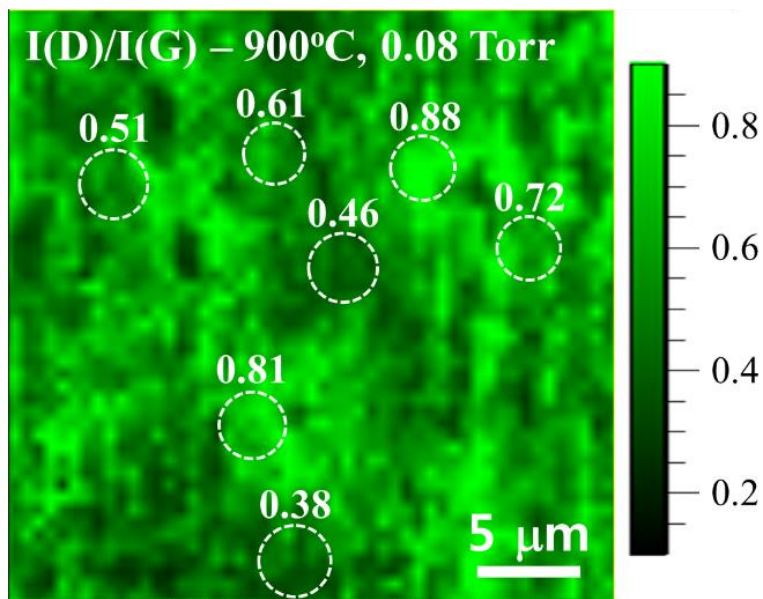


Figure 4.5. Estimated TAB size for the each measurement spots with different I(D)/I(G) ratio. Relatively uniform distribution of I(D)/I(G) (Si dopants) possibly ensures the negligible uncertainties from doping inhomogeneity.

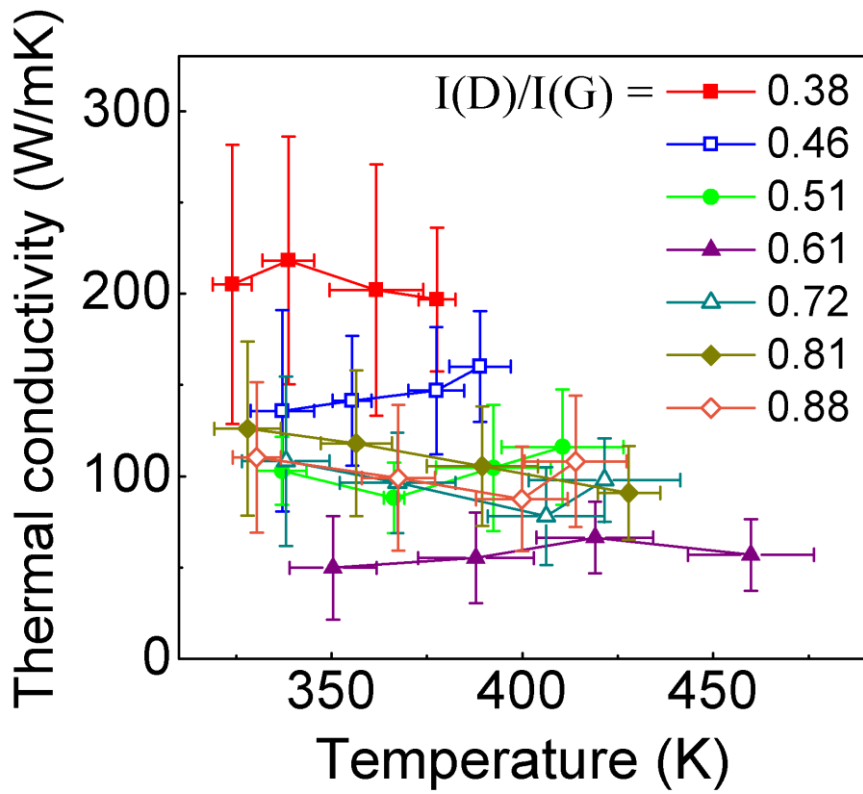


Figure 4.6. Thermal conductivities of SiG with the I(D)/I(G) variation as a function of temperature, which indicates the negligible temperature dependence in Si-doped graphene.

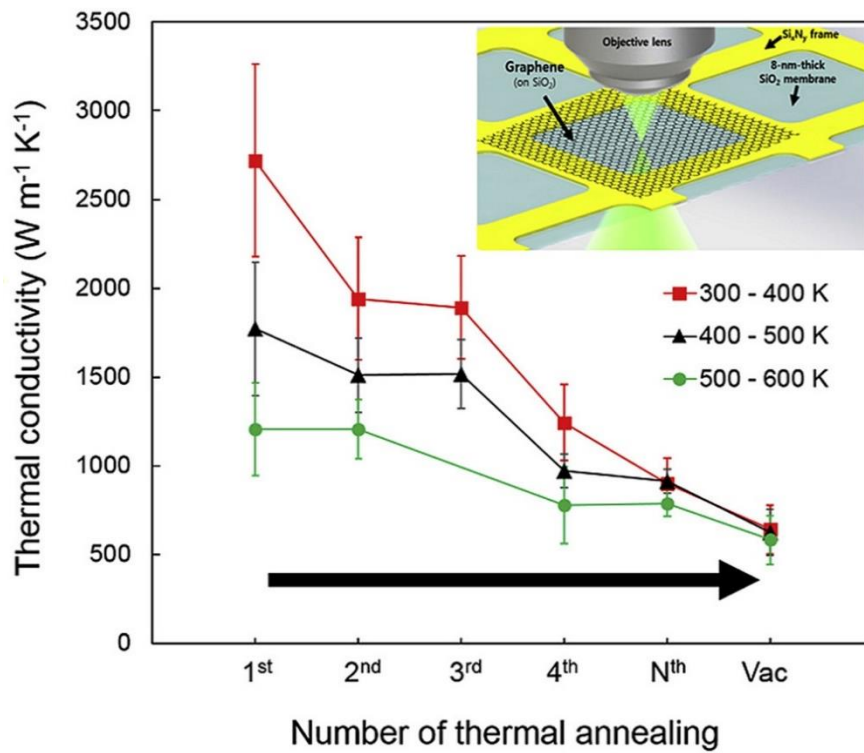


Figure 4.7. (From Kim et al, 2017, *Carbon*) Thermal conductivities of pristine supported graphene with the increasing number of thermal annealing. Enhanced graphene-substrate conformity by thermal annealing in vacuum suppresses the long-wavelength phonons in graphene, reducing the temperature dependence.

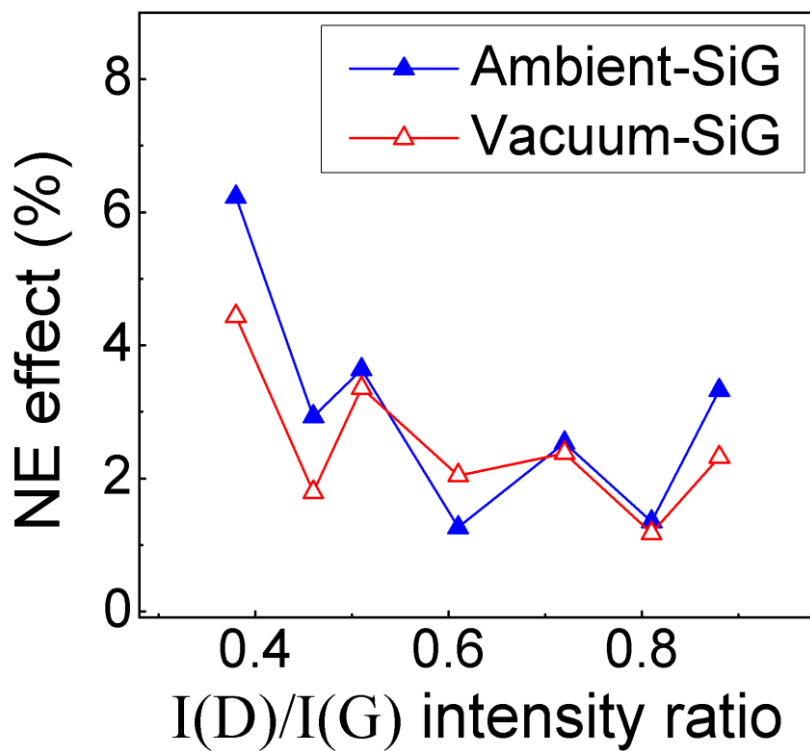


Figure 4.8. Non-equilibrium error in Si-doped graphene with a function of I(D)/I(G) intensity ratio. Temperature discrepancy exhibits less than 6% of non-equilibrium error and gradually decreases with the increase of I(D)/I(G).

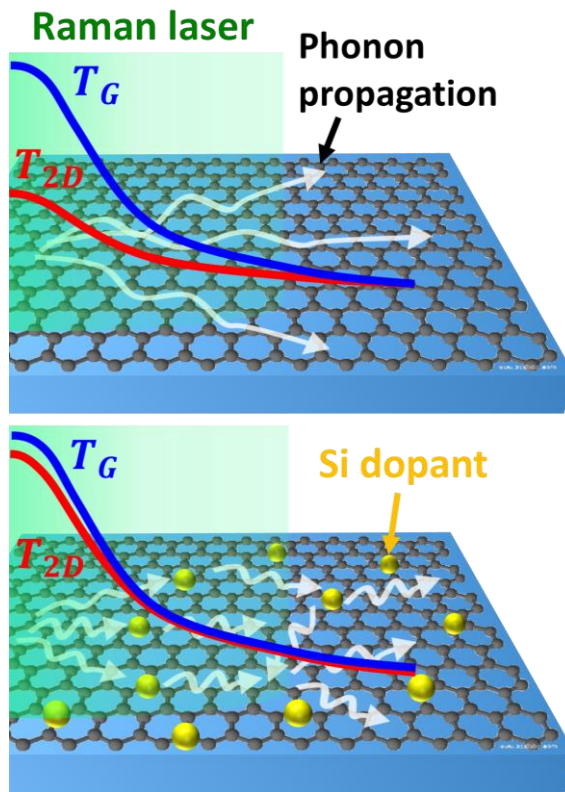


Figure 4.9. A schematic illustration for the non-equilibrium effects for PG and SiG. The effects decrease with the increase in Si doping concentrations, attributing to the reduced phonon MFPs and breakdown of reflection symmetry, both by the presence of Si dopant atoms.

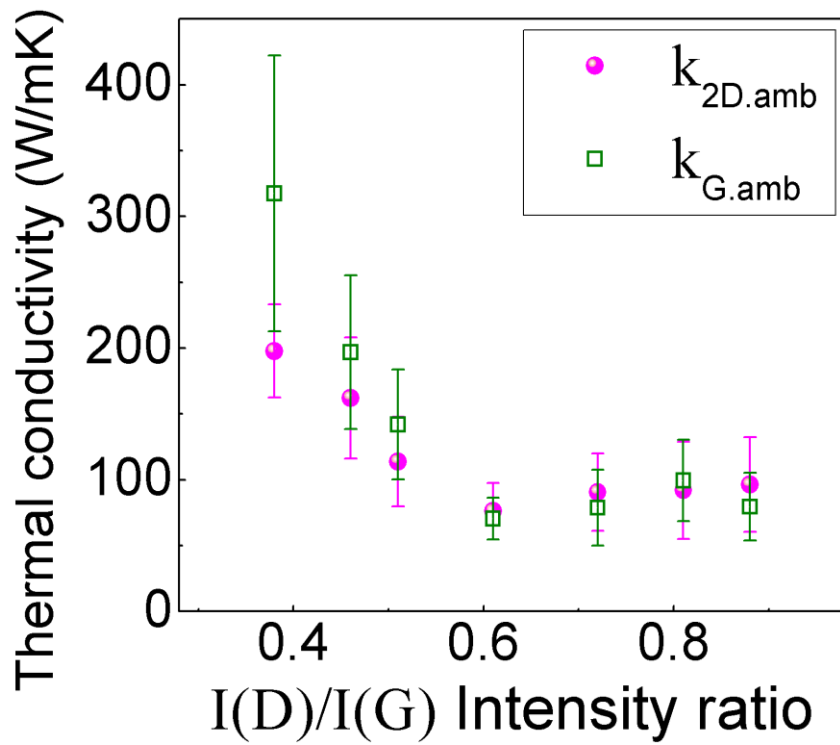


Figure 4.10. Thermal conductivities of ambient-annealed SiG derived both by 2D peak calibration ($k_{2D.amb}$) and G peak calibration ($k_{G.amb}$). Both values become similar with the increase of I(D)/I(G) ratio.

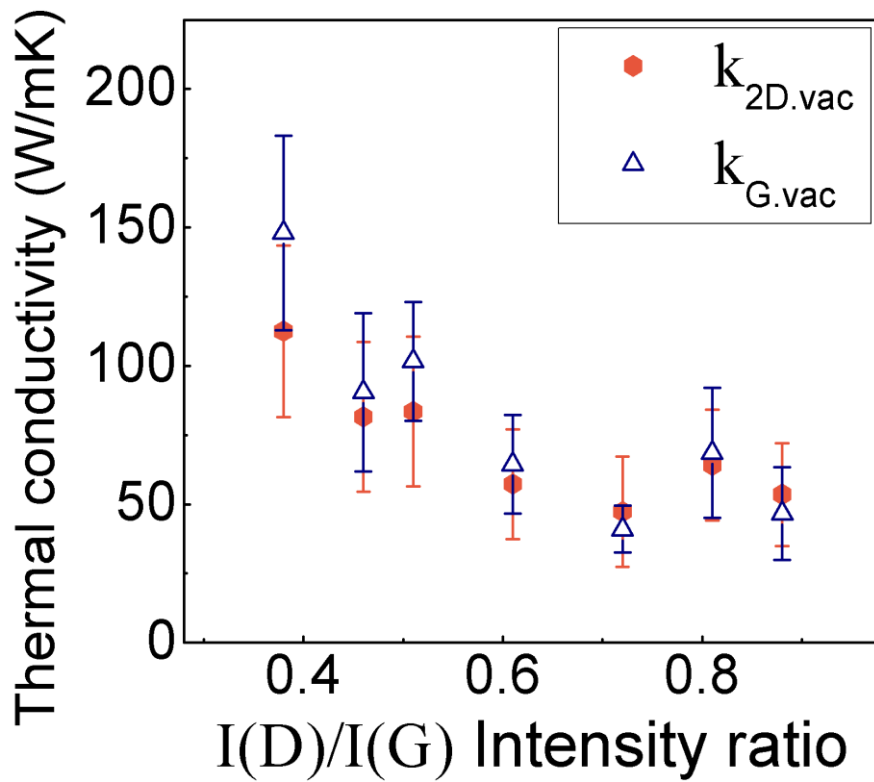


Figure 4.11. Thermal conductivities of vacuum-annealed SiG derived both by 2D peak calibration ($k_{2D.vac}$) and G peak calibration ($k_{G.vac}$). Similar with ambient case, both values become closer with the increase of I(D)/I(G) ratio.

| I(D)/I(G) | 2D peak calibration | | G peak calibration | |
|----------------------------------|----------------------------|-------------------------|---------------------------|------------------------|
| | $k_{2D.amb}$ (W/m·K) | $k_{2D.vac}$ (W/m·K) | $k_{G.amb}$ (W/m·K) | $k_{G.vac}$ (W/m·K) |
| 0: pristine graphene (suspended) | 2662.5 [9] | | ~2500 [39] | |
| 0: pristine graphene (supported) | - | | 900.18 [35] | 645.56 [35] |
| 0.38 | 197.813 | 112.52 | 317.511 | 148.034 |
| 0.46 | 162.204 | 81.598 | 196.992 | 90.465 |
| 0.51 | 113.745 | 83.549 | 142.016 | 101.599 |
| 0.61 | 76.17 | 57.251 | 70.543 | 64.444 |
| 0.72 | 90.71 | 47.342 | 78.8 | 40.972 |
| 0.81 | 92.08 | 64.089 | 99.52 | 68.562 |
| 0.88 | 96.4 | 53.552 | 79.469 | 46.666 |

Table 4.1. Summary for the thermal conductivities with the I(D)/I(G) variation of Si-doped graphene. Note the order-of-magnitude reduction and two order-of-magnitude reduction of Si-doped graphene, compared to supported pristine graphene and suspended pristine graphene, respectively.

| Reference | Dopant | k/k_0 | Note | Method | Descriptions |
|----------------------------------|-----------------------------------|--|--|-------------------------------------|---------------------------|
| Experimental Measurements | | | | | |
| Present work | Si (M = 28) | 0.089 | 1.91% concentration Ambient- annealed | Optothermal Raman Thermometry | Supported CVD graphene |
| | | 0.036 (Relative to the suspended k_0) | | | |
| | | 0.072 | 1.91% concentration Vacuum- annealed | | |
| | | 0.020 (Relative to the suspended k_0) | | | |
| Chen, et al. [15] | ¹³C (M = 13) | 0.631 | 1.1% concentration | | Suspended CVD graphene |
| Theoretical Predictions | | | | | |
| Goharshadi , et al. [19] | N (M = 14) | 0.412 | | MD (Equilibrium) | Suspended graphene |
| Hu, et al. [14] | ¹³C (M = 13) | 0.801 | 5% concentration | MD (Nonequilibrium) | |
| | ²⁴C (M = 24) | 0.041 | 10% concentration | | |
| Mortazavi, et al. [16] | B (M = 10.8) | 0.164 | Zigzag (ZZ) | | |
| | | 0.149 | Armchair (AC) | | |
| Mortazavi, et al. [17] | N (M = 14) | 0.365 | ZZ | | |
| | | 0.323 | AC | | |
| Zhang, et al. [18] | N (M = 14) | 0.385 | Graphitic-N | | |
| | | 0.113 | Pyridinic-N | | |

Table 4.2. Thermal conductivity reduction ratio (k/k_0) of substitutionally doped graphene at room temperature. The dopants concentration is 2% unless specified otherwise. Note that present work firstly demonstrates the thermal conductivity reduction of doped graphene as supported on the substrate.

| | Present work | [13] | [10] |
|---------------------------|----------------------|----------------------|-----------------------|
| N_c (cm ⁻²) | 7.3×10^{13} | 1.5×10^{11} | 3.82×10^{12} |
| d (nm) | 0.66 | 14.57 | 2.88 |
| λ/d | 136.26 | 53.19 | 268.47 |

Table 4.3. Comparison of critical defects concentration (N_c), average phonon MFP to inter-defect distance ratio (λ/d) with previous works showing the saturated thermal conductivity reduction.

| I(D)/I(G) | T_m (K) | T_{TAB} (K) | r_{TAB} (mm) |
|------------------|-----------------------------|---------------------------------|----------------------------------|
| 0.38 | 422.22 | 308.44 | 1.709 |
| 0.46 | 446.56 | 308.93 | 1.633 |
| 0.51 | 444.74 | 308.89 | 1.638 |
| 0.61 | 475.18 | 309.5 | 1.459 |
| 0.72 | 490.92 | 309.82 | 1.506 |
| 0.81 | 465.92 | 309.32 | 1.575 |
| 0.88 | 480.7 | 309.61 | 1.533 |

Table 4.4. Maximum temperature of graphene for thermal conductivity measurement spots (T_m) and corresponding temperature for thermal activation boundary (T_{TAB}), and its radius (r_{TAB}).

| I(D)/I(G) | Irradiated laser power | | | |
|-----------|------------------------|------------------------|------------------------|------------------------|
| | ~0.283 mW | ~0.494 mW | ~0.724 mW | ~0.912 mW |
| 0.38 | 205.106 (324.022 K) | 218.232 (338.689 K) | 202.037 (361.725 K) | 196.815 (377.616 K) |
| 0.46 | 135.850 (337.128 K) | 141.327 (355.395 K) | 146.948 (377.495 K) | 160.144 (388.910 K) |
| 0.51 | 102.956 (336.978 K) | 88.178 (366.346 K) | 104.649 (392.396 K) | 116.062 (410.515 K) |
| 0.61 | 49.861 (350.389 K) | 55.260 (387.817 K) | 66.449 (419.009 K) | 56.976 (459.846 K) |
| 0.72 | 108.301 (338.037 K) | 96.368 (367.291 K) | 78.109 (406.228 K) | 98.013 (421.513 K) |
| 0.81 | 126.114 (328 K) | 118.106 (356.473 K) | 105.599 (389.506 K) | 90.848 (427.886 K) |
| 0.88 | 110.327 (330.423 K) | 99.184 (367.516 K) | 87.582 (399.891 K) | 108.209 (413.918 K) |

Table 4.5. Temperature-dependent thermal conductivities of Si-doped graphene with the variation of I(D)/I(G). Note the negligible temperature dependence regardless of the I(D)/I(G) ratio.

Chapter 5

Thermoelectric properties of Si-doped graphene

5.1. Thermoelectric properties of graphene

Thermoelectric effects mean the direction conversion between the temperature gradient and voltage gradient. In spite of its huge potentials for the application in power generation and energy harvesting from wasted heat with no moving part, current low conversion efficiency limits the practical application of thermoelectric devices.[88] As mentioned in chapter 1, generally thermoelectric efficiency ZT can be described as below equation.

$$ZT = \frac{\sigma S^2 T}{k}$$

We directly understand that high thermal conductivity in pristine graphene greatly suppresses its thermoelectric conversion efficiency, which reduces the temperature gradient in materials. In addition, Seebeck coefficient, which indicates the measure of thermoelectric voltage induced by the temperature difference along the materials, is found to be small compared to other bulk

materials, which is attributable to the gapless characteristics of graphene's electronic band structure.[89] Gapless materials generally cannot separate the contribution of single carrier type (electron or hole), and counteracting of both charge carriers reduces the induced thermoelectric voltage. Both previous experimental and theoretical studies represent the low ZT value of pristine graphene, ranging from 10^{-4} to 10^{-2} . [26,90-92]

Considering that practical application of thermoelectric devices requires the ZT at least larger than 1, [88] innovative strategies for the ZT enhancement should be preceded for the application of graphene as thermoelectric materials. Recently, strategies for the conversion efficiency enhancement include the nanostructuring of materials, introduction of structural defects, and doping. [27] All of adopted strategies focus on the simultaneous increase of Seebeck coefficient and suppression in lattice thermal conductivity, while maintaining the excellent electrical conductance.

Nanostructured graphene nanoribbons (GNR) are known to enhance the thermoelectric efficiency by simultaneously reducing the thermal conductivity and increasing the Seebeck coefficient. Quantum confinement effect in GNRs improves the density of states (DOS) near Fermi level, thus increasing the thermoelectric power (Seebeck coefficient). [27] In addition, patterning of zigzag edges structure in GNRs simultaneously suppresses

lattice thermal conductivity through significant boundary scattering. Some MD based theoretical predictions reported the achievement of ZT enhancement, $ZT_{\max} \sim 1$ for mixed structure of zigzag and armchair edge sections,[90] $ZT_{\max} \sim 0.2$ for armchair GNRs with vacancy defects,[91] and $ZT_{\max} \sim 2.5$ for the GNRs with the mixed vacancy and isotopes defects,[92] for instance. However, most MD predictions use the oversimplified model and have limitations in domain sizes, reflecting only the ideal case for the thermoelectric efficiency enhancement.

Most experimental studies regarding ZT enhancement of graphene induce the structural or point defects to independently suppress the lattice thermal conductivity. Order-of-magnitude larger average mean free path of phonons compared to electrons allows higher phonon scattering rate than that of electrons by controlling the grain sizes of polycrystalline graphene, thus showing the possibility of ZT enhancement.[9,25] In addition, recent study directly measured the thermoelectric properties of nano-hole patterned graphene and also exhibited the simultaneous decrease of thermal conductivity while enhancing thermoelectric power.[20] However, they measured the thermal conductivities of graphene as suspended on SiN_x membrane, obstructing the consistent comparison between the thermal properties reduction and electrical properties measured on SiO_2 substrate.

Other groups successfully derive the ZT with the I(D)/I(G) Raman peak ratio variation in defected graphene under high power oxygen-plasma irradiation, and found the maximum 3 times enhancement compared to that of pristine graphene, $ZT/ZT_0 \sim 3$. [26] However, absolute value of ZT in defected graphene do not represent the possibility of practical application of graphene as thermoelectric materials with too low ZT of 10^{-3} order.

In terms of thermoelectric conversion efficiency enhancement, Si-doped graphene can be excellent candidate, attributing to its great suppression in lattice thermal conductivity as shown in chapter 4. In addition, previous experimental demonstration of bandgap opening by substitutional Si dopants indicate the possibility of thermoelectric power enhancement. [31] This can be attributable to the contribution of electrons and holes can be separated through finite bandgap in electronic structure. [89] The same number of valance electrons between host C atoms and Si dopants (group 14) possibly maintain the high electrical conductance with minimum electrons scattering. In chapter 5, we measure the electrical properties of Si-doped graphene and compare the electrical properties alteration with previous thermal conductivity reduction. This will shed the light on the possible application of doped graphene as an efficient thermoelectric materials.

5.2. Electrical properties in Si-doped graphene

4-point probe measurement is adopted for the electrical properties measurement for both pristine and Si-doped graphene (**Figure 5.1**). Two probes (drain and source) generate the voltage difference and remaining two probes measure the voltage drop across the graphene (V_{gr}) without suffering from the possible contact resistance. Facilitation of standard resistor for the whole electrical system allows to derive the current flowing through graphene. By measuring the voltage drop across the standard resistance (V_{st}), we can calculate the sheet resistance of graphene (R_{gr}) using below equation

$$R_{gr} = R_{st} \frac{V_{gr}}{V_{st}}$$

where R_{st} indicates the resistance of standard resistor. With the geometric configuration of transferred graphene with length of L , thickness of t_g , and width of W , graphene conductivity (σ) can be deduced from below equation

$$\sigma = \frac{1}{R_{gr}} \frac{L}{W t_g}$$

Another electrical properties, electrical mobility (μ), is the measure of the

ability to move through the materials when the electric field is applied for charge carriers. Electrical mobility has relation with the electrical conductivity as

$$\sigma = en\mu$$

where e is the elementary charge, n is the charge carrier concentration. To calculate the electrical mobility of graphene, we manipulate the carrier concentration by facilitating the dielectric materials, SiO_2 . Applied gate voltage across the dielectric SiO_2 film enables to control the concentration of doped charge carrier in graphene films. Total induced charge (Q) of charge carriers induced by the applied gate voltage (V_g) can be calculated $Q = C_{\text{SiO}_2} V_g$, where the $C_{\text{SiO}_2} = 1.15 \times 10^{-4} \text{ F/m}^2$ is the capacitance of SiO_2 . Considering that Q can be corresponded to the $e \times n$ in the equation of σ , we can conclude the equation for the derivation of electrical mobility as below.

$$\mu = \frac{1}{C_{\text{SiO}_2}} \frac{\Delta\sigma}{\Delta V_g}$$

By calculating the slope from the σ vs. V_g correlation from the experiment,

we can derive the electrical mobility of graphene. For the more detailed description, we separate the equations for each electron and hole contributions as below.

$$\sigma = \begin{cases} \mu_e C_{SiO_2} \Delta V_g + \sigma_{Dirac} = \mu_e C_{SiO_2} (V_g - V_{g,Dirac}) + \sigma_{Dirac} \\ -\mu_h C_{SiO_2} \Delta V_g + \sigma_{Dirac} = -\mu_h C_{SiO_2} (V_g - V_{g,Dirac}) + \sigma_{Dirac} \end{cases}$$

Here, $V_{g,Dirac}$ and σ_{Dirac} are the gate voltage and electrical conductivity at the dirac point, the point with the lowest electrical conductivity. In addition, μ_e and μ_h indicate the electron and hole mobility, whose contributions are dominant in the range of $V_g > V_{g,Dirac}$ and $V_g < V_{g,Dirac}$, respectively.

The field effect transistors (FET) based on graphene samples were fabricated using the conventional photolithography with the patterned Au/Cr electrodes on 300 nm SiO₂/Si substrate (**Figure 5.2**). Before the measurement, fabricated samples were thermally-annealed at 500°C for 2 hours to remove the absorbed molecules and enhance graphene-substrate conformity in high vacuum of 10⁻⁷ Torr. This enables the consistent comparison between the thermal conductivity reduction and electrical properties reduction, attributing to the similar graphene-substrate conformity. The drain-source voltage is fixed as 0.1 V and we vary the gate voltage from -36 V to +36 V to control

the sign of dominant charge carriers. The resistance of standard resistor is set as 500 Ω . The length of graphene for measurement area is fixed as 20 μm while the width of graphene is ~ 1.5 mm measured by optical microscope. To measure the electrical properties with the Si dopants concentration variation, we use the three SiG samples with average $I(D)/I(G)$ peak ratio of 0.38, 0.51, and 0.72, respectively. Each $I(D)/I(G)$ values are corresponded to the Si dopants concentration of 1.43 %, 1.87 %, 2.59 %, respectively.

Figure 5.3 represents the measured electrical conductivities of three SiG samples with the gate voltage variation at room temperature. We clearly confirm the conductivity variation when the majority charge carriers are imposed by the induced gate voltage through the dielectric SiO_2 substrate. Note that lowered gate voltage compared to dirac voltage ($V < V_g$) indicates the hole as a dominant charge carrier, while higher gate voltage ($V > V_g$) indicates the electron. Our thermal annealing in high vacuum before electrical conductivities measurement removes other possible chemical residue which influences on the electrical characteristics. In this situation, dirac voltage shift indicates the alteration of intrinsic doping characteristics in graphene. We found that dirac voltage moves to +8 ~ +10 V while PG shows the dirac voltage near 0V, representing the charge carriers neutrality of PG and p-type doping in SiG, respectively.[93] The role of hole as majority charge carriers

in SiG (p-type doping) is consistent with the observed upshift of G peak and 2D peak in Raman spectrum (see **Figure 2.10**).

As mentioned in chapter 5.2.1, we can derive the electrical mobilities with the I(D)/I(G) peak ratio variation by facilitating the above equations and calculating the linear slope in **Figure 5.3** (see **Table 5.1**). Sub-linear behavior near dirac voltage for higher I(D)/I(G) can be attributable to the increasing short-range scattering of charge carriers by substitutional Si dopants.[94] When compared to the electrical mobility of PG, all the SiG samples exhibit the progressively reduced electrical mobility with the increase of Si dopants concentration, which can be attributable to the enhanced charge carrier scattering near the substitutional Si dopants as described by the below equation[95]

$$\tau_{Si.e} \approx \frac{2e^2}{\pi h} \left(\frac{n}{n_{Si}} \right) \ln^2(k_F R)$$

where the $\tau_{Si.e}$ is the scattering rate of electrons by silicon dopants, e is the electronic charge, h is the Planck's constant, n is the induced charge carrier concentration, n_{Si} is the Si defects density, k_F is the Fermi wavevector, and R is the radius of scattering potential, respectively. Our measured

conductivities are comparable with the previously reported electrical mobility of SiG, 660 cm²/Vs for 2.63 % Si concentration[28] (solid precursor) and 463 cm²/Vs for 3.4 % Si concentration[31] (gas precursor). However, we believe that previous studies have some limitations of their inherent ambiguity in terms of samples configurations (see **chapter 2.2.1**) and weak graphene-substrate conformity. The maximum mobility reduction ratio (μ/μ_0 , μ_0 for PG) at the available Si doping concentration is derived as $\mu_n/\mu_{n0} = 0.47$ and $\mu_e/\mu_{e0} = 0.26$, respectively, which exhibit less reduction than thermal conductivities.

On the other hand, thermoelectric conversion efficiency (ZT) contains the electrical conductivities of materials, not mobilities themselves in the equation of thermoelectric conversion efficiency. Electrical mobility measurement exhibits the maintenance of electrical properties in SiG, which can be attributable to the absence of lattice defects for substitutional dopants. We also analyze the electrical conductivities reduction with the gate voltage variation for more precise elaboration in ZT enhancement by Si dopants. **Figure 5.4** shows the reduction ratio of electrical conductivities (σ/σ_0) with the gate voltage variation from the dirac voltage. We found the distinct contrast in reduction ratio between the hole and electron conductivities in each SiG samples. Smaller reduction ratio of hole conductivity can be

attributable to the intrinsically higher hole concentration in p-type doped SiG, while PG represents the comparable electrical conductivity for both hole and electrons. In addition, increasing Si dopants concentration ($\sim I(D)/I(G)$) also progressively decreases the electrical conductivity reduction ratio, similar with the electrical mobility.

This significantly high electrical properties in SiG can be comparable to the highest value of previously reported doped graphene with nitrogen or boron.[93,96,97] We believe that pure Si-C bond in our samples can be attributable to the minor reduction in electrical properties, in spite of large mass difference between host C atoms and Si dopants. This pure Si-C bond indicates that no other functional groups such as Si-O-C obstruct the propagation of electrons and also maintain the hexagonal lattice in graphene without substantial structural defects. The same number of valence electrons between the C and Si atoms can be possibly attributable to the maintained electrical properties of graphene.

5.3. Possibility of ZT enhancement

Previous chapter reports the electrical properties reduction when the Si dopants are incorporated into graphene lattices. By consistently comparing the reduction ratio between the electrical (σ/σ_0) and thermal conductivity

(k/k_0), possible ZT enhancement by Si dopants can be elaborated. **Figure 5.5** represents the k/k_0 and σ/σ_0 with the I(D)/I(G) ratio variation. We facilitates the thermal conductivities for vacuum-annealed SiG with 2D peak calibration for k/k_0 , which has the consistent graphene-substrate conformity with samples for σ measurement and the best measurement reliability.[35]

In case of electrical conductivities, electrical conductivities reduction shows the dependence on the biased gate voltage regardless of the induced majority charge carriers. With the increase of gate voltage difference for both hole and electrons, the electrical conductivity reduction ratio will be converged to the ratio of electrical mobility (see the above equation). Therefore, we consider the converged electrical conductivity reduction ratio as that of electrical mobilities for each of SiG samples with different I(D)/I(G) peak ratio. We found that SiG exhibits the further reduction of thermal conductivities compared to that of electrical conductivities regardless of the contribution of charge carriers.

Figure 5.6 finally represents the comparison between thermal conductivity reduction and electrical conductivity reduction in SiG by $(\sigma/\sigma_0)/(k/k_0)$. We found the progressive increase of $(\sigma/\sigma_0)/(k/k_0)$ for both hole and electrons contribution with the increase of Si dopants concentration. This shows the possibility that thermoelectric efficiency can be increased up to 8 times

compared to that of PG by incorporating the maximum 2.59 % Si dopants into graphene lattices. This can be attributable to the substantial decrease in thermal conductivities without significant reduction in electrical properties by substitutional Si dopants. Note that our incorporated Si dopants represents the further ZT enhancement of graphene when compared to the recent study on the effects of plasma-induced defects on ZT enhancement ($ZT/ZT_0 \sim 2$) for supported pristine graphene.[26] Destructive high energy irradiation by oxygen plasma can significantly break the lattice symmetry in graphene, which also shows the simultaneous reduction in electrical conductivities and thermal conductivities. In addition, oxygen plasma provides the unintentional oxygen functional groups in graphene lattices and is only applicable to the few layer graphene. On the other hand, although Si dopants severely obstructs the phonon transport by large mass difference with C atoms, substitutionally doped Si atoms do not severely induce the structure defects by pure Si-C bonding, allowing to maintain the significantly high electrical properties of graphene. Therefore, it can be concluded that substitutional Si doping can be one of the best strategy for the thermoelectric efficiency enhancement for graphene.

Note that our elaboration neglect the alteration of Seebeck coefficient by Si dopants. Increase of graphene thermopower has been achieved by breaking

the symmetry in graphene and opening the bandgap enough to have the sufficient majority charge carrier.[89] This is because bandgap opening enables to separate the contribution of majority charge carrier, thus minimizing the counteracting of opposite charge carriers and increasing the induced electric field under temperature gradient. Quantitative estimation on the relation between the bandgap and thermoelectric properties (Seebeck coefficient) is provided by the Goldsmid-Sharp as[98]

$$E_g = 2e|S|_{max}T_{max}$$

where the E_g is the bandgap, e is the electronic charge, $|S|_{max}$ is the maximum absolute value of Seebeck coefficient, and T_{max} is the corresponding temperature, respectively. This equation also indicates the enhancement of thermopower under the opening of bandgap. For the graphene, one study reported that thermopower can be greatly enhanced up to $\sim 700 \mu\text{V/K}$ by inducing the defects in few layer graphene with oxygen plasma treatment (Note that typical Seebeck coefficient of pristine CVD graphene is $20 \sim 50 \mu\text{V/K}$).[99] Their modeling also proposed the factor of two increasing Seebeck coefficient with the bandgap opening of 0.2 eV near room temperature. Considering the experimental demonstration of bandgap

opening (0.28 eV) in SiG with 3.1% doping concentration by first-principle study,[31] we believe that Seebeck coefficient could be increased by incorporation of Si dopants. Only minor decrease of electrical conductivity in SiG further supports the possibility of maintenance in powerfactor ($S^2\sigma$). Therefore, Seebeck coefficient is not the main concern for our elaboration regarding ZT enhancement.

5.4. Summary

In chapter 5, we experimentally measure the electrical properties of SiG with Si dopants concentration variation, and study the possibility of thermoelectric conversion efficiency of graphene using Si dopants. Our electrical measurement indicates that Si doping induces the p-type doping in graphene, justifying the consideration of hole as a majority charge carrier. Both electrical mobility and conductivity reduction ratio exhibits minor decrease compared to thermal conductivity reduction ratio. For instance, the majority charge carrier (hole) shows the electrical reduction ratio of 0.47 with 2.6% Si doping concentration. We consistently compare the reduction ratio by facilitating the same thermal annealing conditions for similar degree of graphene-substrate conformity, which allows to derive the $(\sigma/\sigma_0)/(k/k_0)$ enhancement under Si incorporation. Our calculation indicates the possible

maximum 8 times increase of thermoelectric conversion efficiency in SiG with 2.6% Si doping concentration, which shows further enhancement than previous oxygen-plasma treatment. We believe that pure Si-C bonds characteristics, the same number of valence electrons between Si and C atoms, and minimum breakdown of graphene lattices by substitutional dopants can be attributable to the observed maintenance of electrical properties compared to thermal properties. Negligible effects of Seebeck coefficient for the ZT enhancement can be justified by the inherent bandgap opening in SiG.

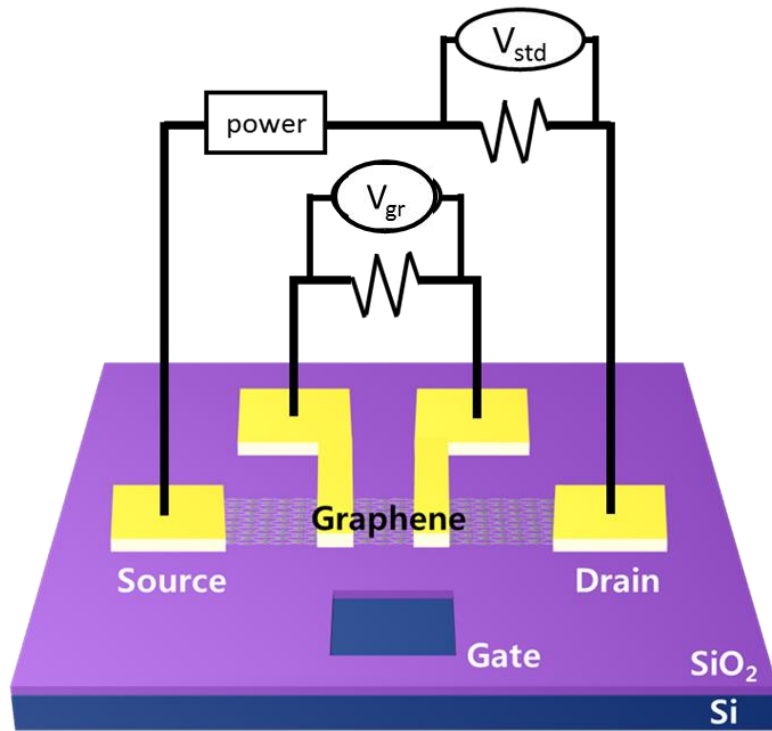


Figure 5.1. Schematic description on the 4-point measurement method for electrical conductivity. Gate voltage variation allows to derive the electrical mobility under the manipulation of majority charge carrier.

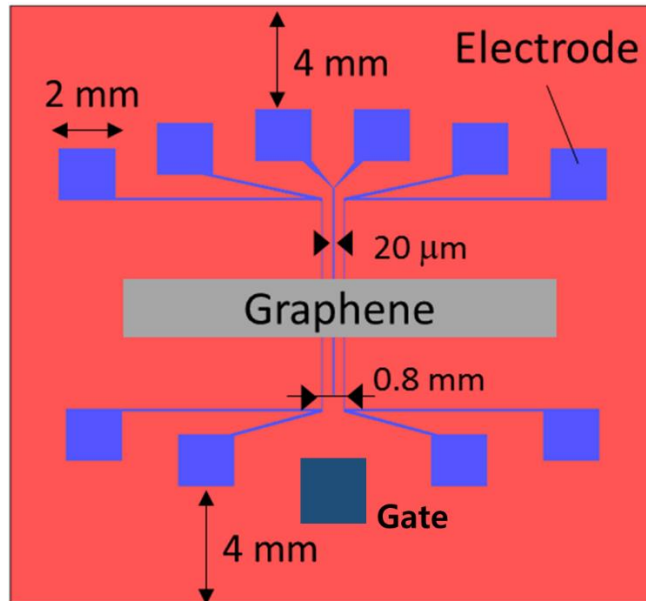


Figure 5.2. Design of the FET graphene/electrodes for the measurement of electrical properties using 4-point probe method.

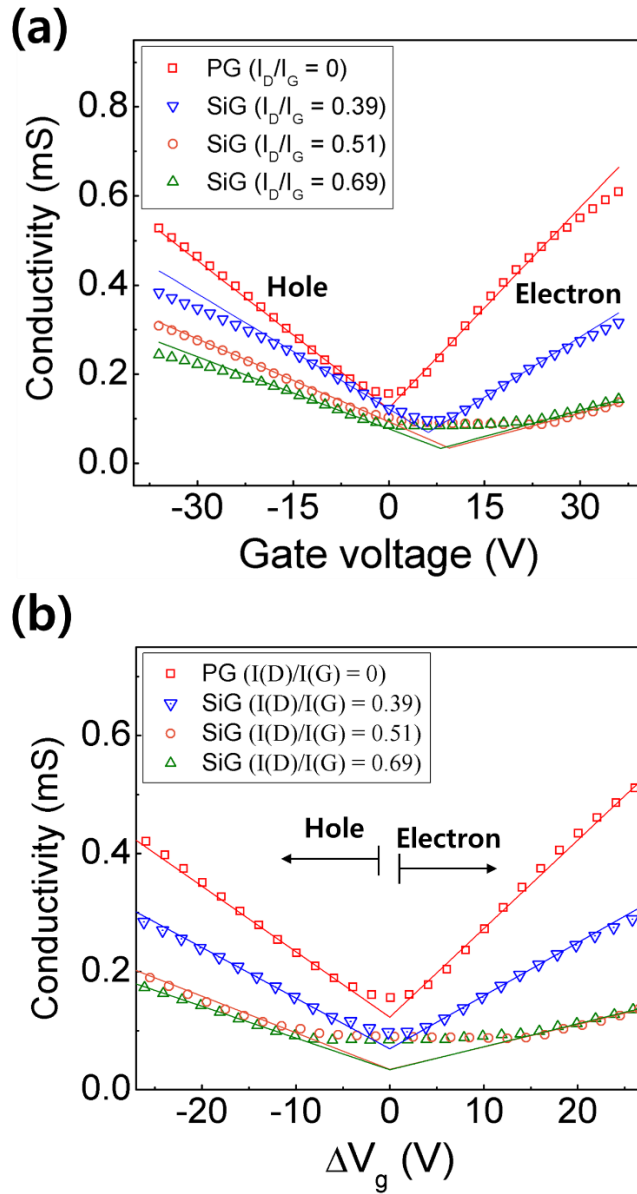


Figure 5.3. Electrical conductivity of both PG and SiG samples with (a) the gate voltage variation (from -36 V to +36 V), and (b) the gate voltage difference variation (ΔV_g) (from -28 V to +28 V).

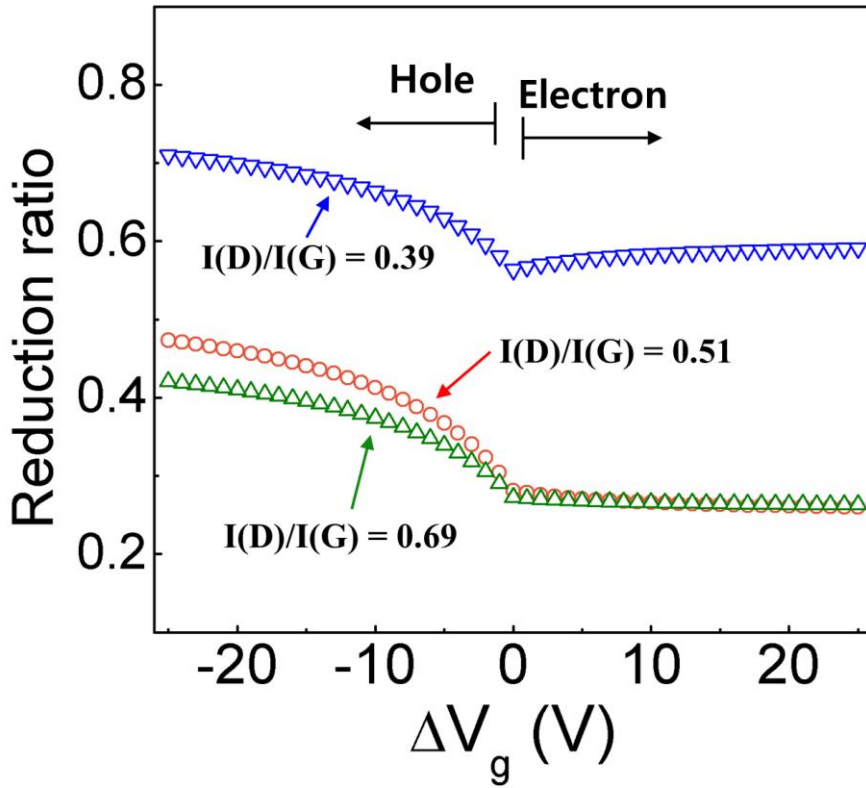


Figure 5.4. The reduction ratio (σ/σ_o) of SiG electrical conductivity (σ) compared to that of PG (σ_o) with the gate voltage difference variation. Lowered reduction for hole conductivity can be attributable to the increased hole concentration in SiG, and noticeable progressive decrease in reduction ratio with the increase of $I(D)/I(G)$ can be observed.

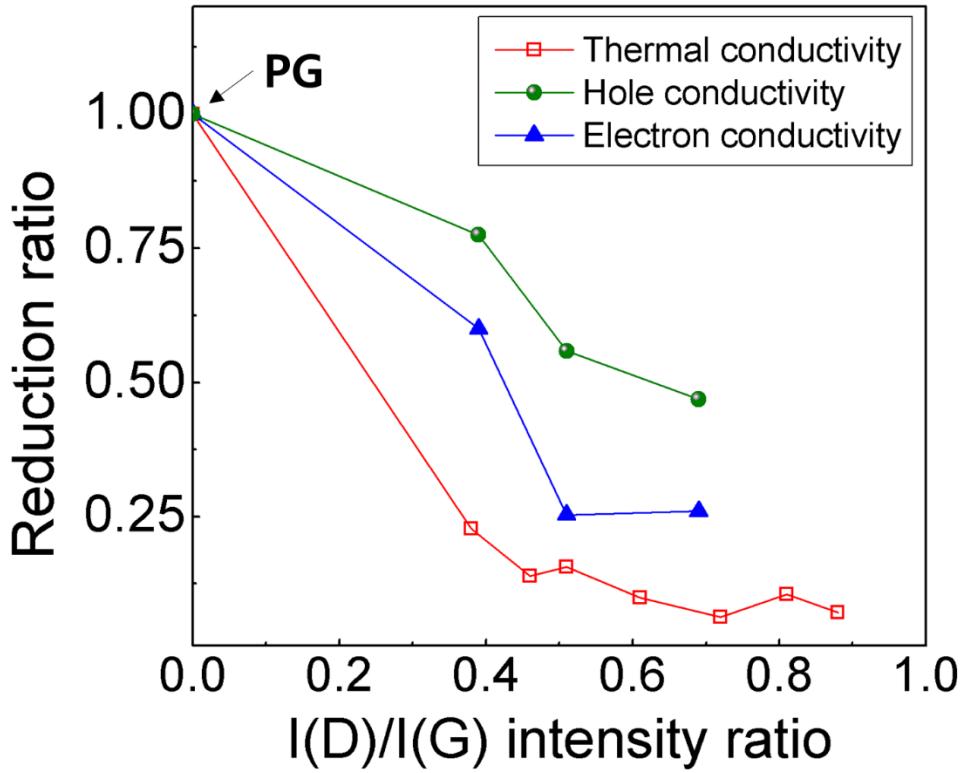


Figure 5.5. The average reduction ratio (σ/σ_0) of hole and electron electrical conductivity (σ), and thermal conductivity reduction ratio (k/k_0) compared to those of PG (k_0 and σ_0) with the $I(D)/I(G)$ variation. Observed lower k/k_0 compared to σ/σ_0 indicates the possibility of ZT enhancement in SiG.

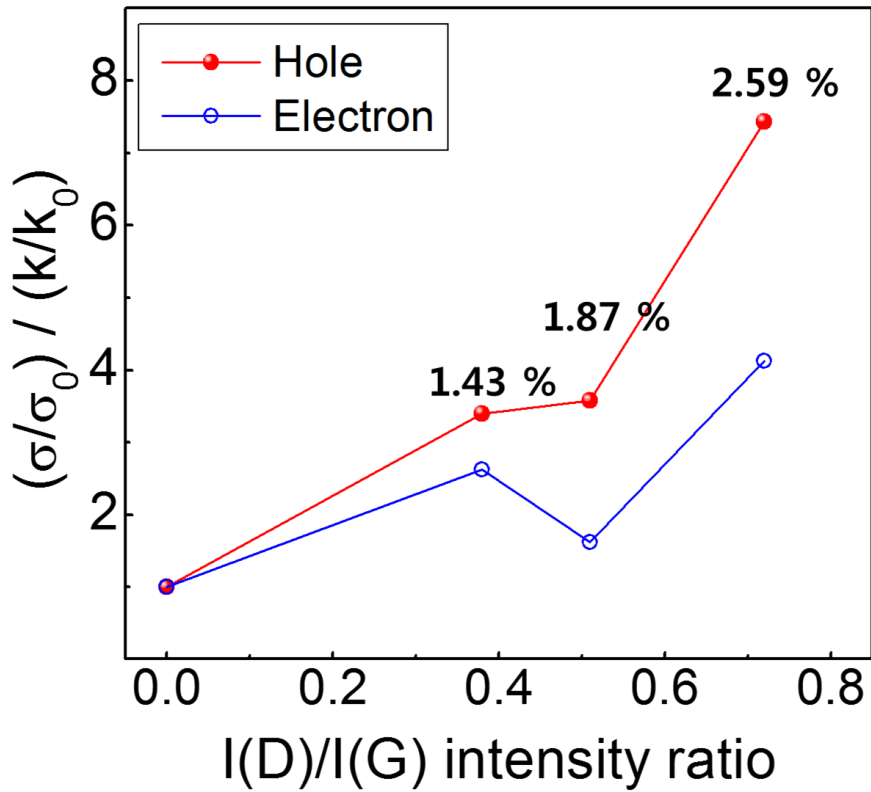


Figure 5.6. Reduction ratio comparison ($(\sigma/\sigma_0)/(\kappa/\kappa_0)$) which shows the possibility of ZT enhancement in SiG with different I(D)/I(G) peak ratio (Si dopants concentration). Maximum more than 8 times enhancement can be achieved by substituting about 2.6% Si dopants into graphene lattices.

| Samples | Hole mobility (cm²/V · s) | Electron (cm²/V · s) |
|------------------------------------|---|--|
| PG (I(D)/I(G) = 0) | 965.22 | 1304.35 |
| SiG (I(D)/I(G) = 0.39) | 747.8261 | 782.6087 |
| SiG (I(D)/I(G) = 0.51) | 539.1304 | 330.4348 |
| SiG (I(D)/I(G) = 0.69) | 452.1739 | 319.1304 |

Table 5.1. Electrical mobilities of PG and SiG samples with I(D)/I(G) variation. We found the minor decrease in electrical mobilities of SiG compared to thermal conductivity reduction, indicating the relative independent decrease in thermal conductivity under Si incorporation.

Chapter 6

Summary and Conclusion

In this study, the effect of substitutional Si dopants on thermal properties of graphene was experimentally investigated, which provides the largest mass perturbation and thus severe phonon scattering in graphene. In chapter 2, we report the synthesis of Si-doped graphene under LPCVD using liquid precursors. Our choice of liquid precursors is based on the fact that solid and gas precursors have their own disadvantages in terms of sample qualities and doping concentration control. We optimized the synthesis recipes and succeed to synthesize the high-quality Si-doped graphene, showing lowered I(D)/I(G) peak ratio with comparable Si doping concentration. Systematic synthesis experiments also demonstrate that controlled synthesis temperature and pressure enables to manipulate the doping concentration and homogeneity, supported by the Raman mapping data. Those achievement enables the investigation on the effects of Si doping concentration as well as the exclusive understanding on the role of Si dopants.

In chapter 3, we summarize the detailed experiment procedure for the measurement of thermal conductivities as supported on SiO₂. In spite of

inherent difficulty to probe the in-plane thermal conductivity of supported graphene, our use of extremely thin SiO₂ TEM grid minimizes the portion of out-of-plane heat dissipation, thus enhancing the measurement reliability. In addition, the use of solid substrate justifies more practical necessity than suspended graphene because graphene virtually cannot be self-standing without supporting substrate. We prepare the supported graphene samples with different graphene-substrate conformity by thermal annealing, which provides the precise reflection of the substrate scattering effect.

In chapter 4, thermal conductivities of Si-doped graphene are probed with Si doping concentration variation, which shows the order-of-magnitude reduction with 2% Si doping concentration compared to supported pristine graphene on SiO₂ TEM grid. This value shows further two order-of-magnitude reduction compared to suspended pristine graphene with no phonon-substrate scattering. Grain size visualization and the same thermal annealing recipe between the pristine graphene and Si-doped graphene demonstrates that grain boundary scattering in polycrystalline graphene and graphene-substrate scattering are not main concern in the observed thermal conductivity reduction in Si-doped graphene. Instead, significantly large mass difference between substitutional Si dopants and C atoms can be majorly attributed to the drastic reduction in thermal conductivities. To our knowledge,

our measured thermal conductivities showed the lowest values compared to other theoretical or experimental studies with substitutional dopants of small mass difference. We also investigate the suppressed temperature dependence of thermal conductivities in Si-doped graphene, which is attributable to the reduced contribution of long wavelength phonons both by the Si dopants and underlying substrate. These effects also decrease the non-equilibrium effects between the heat carriers in Si-doped graphene, thus diminishing the possible underestimation on the thermal conductivities when facilitating the optothermal Raman thermometry.

In chapter 5, we further measure the electrical properties of Si-doped graphene with Si dopants concentration variation to probe the possibility of the thermoelectric conversion efficiency enhancement in Si-doped graphene. Our 4-point probe measurement shows that majorly charge carrier in Si-doped graphene exhibits the only half of electrical properties reduction when about Si atoms with 2.6% doping concentration are incorporated into graphene lattices. We found that thermal conductivities show the maximum 8 times further reduction compared to the electrical conductivity reduction, demonstrating the possibility of ZT enhancement in Si-doped graphene. We believe that our research has the novelty in terms of (1) the synthesis of high-quality Si-doped graphene using LPCVD, (2) the first measurement on

thermal properties of Si-doped graphene as supported and achievement of the highest thermal conductivity reduction in graphene proven by the experimental research, and (3) the first demonstration on the possibility of ZT enhancement in Si-doped graphene. Our study will provide not only the fundamental understanding on the thermoelectric properties of substitutionally doped graphene but the possibility of the graphene application as a thermoelectric devices.

Reference

- [1]. Nika, D. L.; Balandin, A. A. Phonons and thermal transport in graphene and graphene-based materials. *Rep. Prog. Phys.* **2017**, *80*, 036502.
- [2]. Novoselov, K. S.; Fal, V.; Colombo, L.; Gellert, P.; Schwab, M.; Kim, K. A roadmap for graphene. *Nature* **2012**, *490*, 192-200.
- [3]. Balandin, A. A.; Ghosh, S.; Bao, W.; Calizo, I.; Teweldebrhan, D.; Miao, F.; Lau, C. N. Superior thermal conductivity of single-layer graphene. *Nano Lett.* **2008**, *8*, 902-907.
- [4]. Xu, Y.; Li, Z.; Duan, W. Thermal and thermoelectric properties of graphene. *Small* **2014**, *10*, 2182-2199.
- [5]. Balandin, A. A. Thermal properties of graphene and nanostructured carbon materials. *Nat. Mater.* **2011**, *10*, 569-581.
- [6]. Nika, D. L.; Balandin, A. A. Two-dimensional phonon transport in graphene. *J. Phys.: Condens. Matter* **2012**, *24*, 233203.
- [7]. Nika, D.; Pokatilov, E.; Askerov, A.; Balandin, A. Phonon thermal conduction in graphene: Role of Umklapp and edge roughness scattering. *Phys. Rev. B.* **2009**, *79*, 155413.
- [8]. Serov, A. Y.; Ong, Z.-Y.; Pop, E. Effect of grain boundaries on thermal transport in graphene. *Appl. Phys. Lett.* **2013**, *102*, 033104.

- [9]. Lee, W.; Kihm, K. D.; Kim, H. G.; Shin, S.; Lee, C.; Park, J. S.; Cheon, S.; Kwon, O. M.; Lim, G.; Lee, W. In-Plane Thermal Conductivity of Polycrystalline Chemical Vapor Deposition Graphene with Controlled Grain Sizes. *Nano Lett.* **2017**, *17*, 2361-2366.
- [10]. Zhao, W.; Wang, Y.; Wu, Z.; Wang, W.; Bi, K.; Liang, Z.; Yang, J.; Chen, Y.; Xu, Z.; Ni, Z. Defect-engineered heat transport in graphene: a route to high efficient thermal rectification. *Sci. Rep.* **2015**, *5*, 11962.
- [11]. Adamyan, V.; Zavalniuk, V. Phonons in graphene with point defects. *J. Phys.: Condens. Matter* **2010**, *23*, 015402.
- [12]. Feng, T.; Ruan, X.; Ye, Z.; Cao, B. Spectral phonon mean free path and thermal conductivity accumulation in defected graphene: The effects of defect type and concentration. *Phys. Rev. B.* **2015**, *91*, 224301.
- [13]. Malekpour, H.; Ramnani, P.; Srinivasan, S.; Balasubramanian, G.; Nika, D. L.; Mulchandani, A.; Lake, R. K.; Balandin, A. A. Thermal conductivity of graphene with defects induced by electron beam irradiation. *Nanoscale* **2016**, *8*, 14608-14616.
- [14]. Hu, S.; Chen, J.; Yang, N.; Li, B. Thermal transport in graphene with defect and doping: Phonon modes analysis. *Carbon* **2017**, *116*, 139-144.
- [15]. Chen, S.; Wu, Q.; Mishra, C.; Kang, J.; Zhang, H.; Cho, K.; Cai, W.; Balandin, A. A.; Ruoff, R. S. Thermal conductivity of isotopically modified

graphene. *Nat. Mater.* **2012**, *11*, 203-207.

[16]. Mortazavi, B.; Ahzi, S. Molecular dynamics study on the thermal conductivity and mechanical properties of boron doped graphene. *Solid State Commun.* **2012**, *152*, 1503-1507.

[17]. Mortazavi, B.; Rajabpour, A.; Ahzi, S.; Rémond, Y.; Allaei, S. M. V. Nitrogen doping and curvature effects on thermal conductivity of graphene: A non-equilibrium molecular dynamics study. *Solid State Commun.* **2012**, *152*, 261-264.

[18]. Zhang, T.; Li, J.; Cao, Y.; Zhu, L.; Chen, G. Tailoring thermal transport properties of graphene by nitrogen doping. *J. Nanopart. Res.* **2017**, *19*, 48.

[19]. Goharshadi, E. K.; Mahdizadeh, S. J. Thermal conductivity and heat transport properties of nitrogen-doped graphene. *J. Mol. Graphics Modell.* **2015**, *62*, 74-80.

[20]. Oh, J.; Yoo, H.; Choi, J.; Kim, J. Y.; Lee, D. S.; Kim, M. J.; Lee, J.-C.; Kim, W. N.; Grossman, J. C.; Park, J. H. Significantly reduced thermal conductivity and enhanced thermoelectric properties of single-and bi-layer graphene nanomeshes with sub-10nm neck-width. *Nano Energy* **2017**, *35*, 26-35.

[21]. Chen, J.; Zhang, G.; Li, B. Substrate coupling suppresses size dependence of thermal conductivity in supported graphene. *Nanoscale* **2013**,

5, 532-536.

[22]. Rani, P.; Jindal, V. K. Designing band gap of graphene by B and N dopant atoms. *RSC Adv.* **2013**, *3*, 802-812.

[23]. Lv, R.; Li, Q.; Botello-Méndez, A. R.; Hayashi, T.; Wang, B.; Berkdemir, A.; Hao, Q.; Elías, A. L.; Cruz-Silva, R.; Gutiérrez, H. R.; Kim, Y. A.; Muramatsu, H.; Zhu, J.; Endo, M.; Terrones, H.; Charlier, J.-C.; Pan, M.; Terrones, M. Nitrogen-doped graphene: beyond single substitution and enhanced molecular sensing. *Sci. Rep.* **2012**, *2*, 586.

[24]. Houmad, M.; Zaari, H.; Benyoussef, A.; El Kenz, A.; Ez-Zahraouy, H. Optical conductivity enhancement and band gap opening with silicon doped graphene. *Carbon* **2015**, *94*, 1021-1027.

[25]. Ma, T.; Liu, Z.; Wen, J.; Gao, Y.; Ren, X.; Chen, H.; Jin, C.; Ma, X.-L.; Xu, N.; Cheng, H.-M. Tailoring the thermal and electrical transport properties of graphene films by grain size engineering. *Nat. Commun.* **2017**, *8*, 14486.

[26]. Yuki, A.; Yuki, I.; Kuniharu, T.; Seiji, A.; Takayuki, A. Enhancement of graphene thermoelectric performance through defect engineering. *2D Materials* **2017**, *4*, 025019.

[27]. Amollo, T. A.; Mola, G. T.; Kirui, M. S. K.; Nyamori, V. O. Graphene for Thermoelectric Applications: Prospects and Challenges. *Crit. Rev. Solid*

State Mater. Sci. **2017**, 1-25.

[28]. Wang, Z.; Li, P.; Chen, Y.; Liu, J.; Zhang, W.; Guo, Z.; Dong, M.; Li, Y. Synthesis, characterization and electrical properties of silicon-doped graphene films. *J. Mater. Chem. C* **2015**, 3, 6301-6306.

[29]. Zhou, W.; Kapetanakis, M. D.; Prange, M. P.; Pantelides, S. T.; Pennycook, S. J.; Idrobo, J.-C. Direct Determination of the Chemical Bonding of Individual Impurities in Graphene. *Phys. Rev. Lett.* **2012**, 109, 206803.

[30]. Lv, R.; dos Santos, M. C.; Antonelli, C.; Feng, S.; Fujisawa, K.; Berkdemir, A.; Cruz-Silva, R.; Elías, A. L.; Perea-Lopez, N.; López-Urías, F. Large-Area Si-Doped Graphene: Controllable Synthesis and Enhanced Molecular Sensing. *Adv. Mater.* **2014**, 26, 7593-7599.

[31]. Zhang, S.; Lin, S.; Li, X.; Liu, X.; Wu, H.; Xu, W.; Wang, P.; Wu, Z.; Zhong, H.; Xu, Z. Opening the band gap of graphene through silicon doping for the improved performance of graphene/GaAs heterojunction solar cells. *Nanoscale* **2016**, 8, 226-232.

[32]. Cho, J. H.; Yang, S. J.; Lee, K.; Park, C. R. Si-doping effect on the enhanced hydrogen storage of single walled carbon nanotubes and graphene. *Int. J. Hydrogen Energy* **2011**, 36, 12286-12295.

[33]. Chen, Y.; Liu, Y.-j.; Wang, H.-x.; Zhao, J.-x.; Cai, Q.-h.; Wang, X.-z.; Ding, Y.-h. Silicon-Doped Graphene: An Effective and Metal-Free Catalyst

for NO Reduction to N₂O? *ACS Applied Materials & Interfaces* **2013**, *5*, 5994-6000.

[34]. Klemens, P. The scattering of low-frequency lattice waves by static imperfections. *Proc. Roy. Soc. A* **1955**, *68*, 1113.

[35]. Kim, H. G.; Kihm, K. D.; Lee, W.; Lim, G.; Cheon, S.; Lee, W.; Pyun, K. R.; Ko, S. H.; Shin, S. Effect of graphene-substrate conformity on the in-plane thermal conductivity of supported graphene. *Carbon* **2017**, *125*, 39-48.

[36]. Lau, C. N.; Bao, W.; Velasco, J. Properties of suspended graphene membranes. *Mater. Today* **2012**, *15*, 238-245.

[37]. Koniakhin, S.; Utesov, O.; Terterov, I.; Nalitov, A. Substrate-induced reduction of graphene thermal conductivity. *Phys. Rev. B* **2017**, *95*, 045418.

[38]. Liu, J.; Wang, T.; Xu, S.; Yuan, P.; Xu, X.; Wang, X. Thermal conductivity of giant mono-to few-layered CVD graphene supported on an organic substrate. *Nanoscale* **2016**, *8*, 10298-10309.

[39]. Cai, W.; Moore, A. L.; Zhu, Y.; Li, X.; Chen, S.; Shi, L.; Ruoff, R. S. Thermal transport in suspended and supported monolayer graphene grown by chemical vapor deposition. *Nano Lett.* **2010**, *10*, 1645-1651.

[40]. Jang, W.; Chen, Z.; Bao, W.; Lau, C. N.; Dames, C. Thickness-dependent thermal conductivity of encased graphene and ultrathin graphite. *Nano Lett.* **2010**, *10*, 3909-3913.

- [41]. Seol, J. H.; Jo, I.; Moore, A. L.; Lindsay, L.; Aitken, Z. H.; Pettes, M. T.; Li, X.; Yao, Z.; Huang, R.; Broido, D. Two-dimensional phonon transport in supported graphene. *Science* **2010**, *328*, 213-216.
- [42]. Novoselov, K. S.; Geim, A. K.; Morozov, S. V.; Jiang, D.; Zhang, Y.; Dubonos, S. V.; Grigorieva, I. V.; Firsov, A. A. Electric Field Effect in Atomically Thin Carbon Films. *Science* **2004**, *306*, 666-669.
- [43]. Mishra, N.; Boeckl, J.; Motta, N.; Iacopi, F. Graphene growth on silicon carbide: A review. *Phys. status solidi (a)* **2016**, *213*, 2277-2289.
- [44]. Pei, S.; Cheng, H.-M. The reduction of graphene oxide. *Carbon* **2012**, *50*, 3210-3228.
- [45]. Li, X.; Cai, W.; An, J.; Kim, S.; Nah, J.; Yang, D.; Piner, R.; Velamakanni, A.; Jung, I.; Tutuc, E. Large-area synthesis of high-quality and uniform graphene films on copper foils. *Science* **2009**, *324*, 1312-1314.
- [46]. Lee, W.; Kihm, K. D.; Park, J. S.; Lee, W.; Kim, H.; Lee, C.; Cheon, S.; Lim, G. Wetting of nanofluids with nanoparticles of opposite surface potentials on pristine CVD graphene. *Exp. Fluids* **2016**, *57*, 118.
- [47]. Sun, Z.; Yan, Z.; Yao, J.; Beitler, E.; Zhu, Y.; Tour, J. M. Growth of graphene from solid carbon sources. *Nature* **2010**, *468*, 549.
- [48]. Li, Z.; Wu, P.; Wang, C.; Fan, X.; Zhang, W.; Zhai, X.; Zeng, C.; Li, Z.; Yang, J.; Hou, J. Low-Temperature Growth of Graphene by Chemical

Vapor Deposition Using Solid and Liquid Carbon Sources. *ACS Nano* **2011**, *5*, 3385-3390.

[49]. Gadipelli, S.; Calizo, I.; Ford, J.; Cheng, G.; Hight Walker, A. R.; Yildirim, T. A highly practical route for large-area, single layer graphene from liquid carbon sources such as benzene and methanol. *J. Mater. Chem.* **2011**, *21*, 16057-16065.

[50]. Srivastava, A.; Galande, C.; Ci, L.; Song, L.; Rai, C.; Jariwala, D.; Kelly, K. F.; Ajayan, P. M. Novel liquid precursor-based facile synthesis of large-area continuous, single, and few-layer graphene films. *Chem. Mater.* **2010**, *22*, 3457-3461.

[51]. Chen, S.; Ji, H.; Chou, H.; Li, Q.; Li, H.; Suk, J. W.; Piner, R.; Liao, L.; Cai, W.; Ruoff, R. S. Millimeter-size single-crystal graphene by suppressing evaporative loss of Cu during low pressure chemical vapor deposition. *Adv. Mater.* **2013**, *25*, 2062-2065.

[52]. Wei, D.; Liu, Y.; Wang, Y.; Zhang, H.; Huang, L.; Yu, G. Synthesis of N-Doped Graphene by Chemical Vapor Deposition and Its Electrical Properties. *Nano Lett.* **2009**, *9*, 1752-1758.

[53]. Agnoli, S.; Favaro, M. Doping graphene with boron: a review of synthesis methods, physicochemical characterization, and emerging applications. *Journal of Materials Chemistry A* **2016**, *4*, 5002-5025.

- [54]. Hui, G.; Zheng, L.; Li, S.; Wenhua, G.; Wei, G.; Lijie, C.; Amrita, R.; Weijin, Q.; Robert, V.; Pulickel, M. A. Synthesis of S-doped graphene by liquid precursor. *Nanotechnology* **2012**, *23*, 275605.
- [55]. Zhang, C.; Mahmood, N.; Yin, H.; Liu, F.; Hou, Y. Synthesis of phosphorus-doped graphene and its multifunctional applications for oxygen reduction reaction and lithium ion batteries. *Adv. Mater.* **2013**, *25*, 4932-4937.
- [56]. Wang, X.; Sun, G.; Routh, P.; Kim, D.-H.; Huang, W.; Chen, P. Heteroatom-doped graphene materials: syntheses, properties and applications. *Chem. Soc. Rev.* **2014**, *43*, 7067-7098.
- [57]. Chen, J.; Shi, T.; Cai, T.; Xu, T.; Sun, L.; Wu, X.; Yu, D. Self healing of defected graphene. *Appl. Phys. Lett.* **2013**, *102*, 103107.
- [58]. Zhang, X.; Hsu, A.; Wang, H.; Song, Y.; Kong, J.; Dresselhaus, M. S.; Palacios, T. Impact of Chlorine Functionalization on High-Mobility Chemical Vapor Deposition Grown Graphene. *ACS Nano* **2013**, *7*, 7262-7270.
- [59]. Chua, C. K.; Sofer, Z.; Khezri, B.; Webster, R. D.; Pumera, M. Ball-milled sulfur-doped graphene materials contain metallic impurities originating from ball-milling apparatus: their influence on the catalytic properties. *PCCP* **2016**, *18*, 17875-17880.
- [60]. Campos-Delgado, J.; Botello-Méndez, A. R.; Algara-Siller, G.; Hackens, B.; Pardoén, T.; Kaiser, U.; Dresselhaus, M. S.; Charlier, J.-C.;

Raskin, J.-P. CVD synthesis of mono- and few-layer graphene using alcohols at low hydrogen concentration and atmospheric pressure. *Chem. Phys. Lett.* **2013**, *584*, 142-146.

[61]. Dong, X.; Wang, P.; Fang, W.; Su, C.-Y.; Chen, Y.-H.; Li, L.-J.; Huang, W.; Chen, P. Growth of large-sized graphene thin-films by liquid precursor-based chemical vapor deposition under atmospheric pressure. *Carbon* **2011**, *49*, 3672-3678.

[62]. Bhaviripudi, S.; Jia, X.; Dresselhaus, M. S.; Kong, J. Role of Kinetic Factors in Chemical Vapor Deposition Synthesis of Uniform Large Area Graphene Using Copper Catalyst. *Nano Lett.* **2010**, *10*, 4128-4133.

[63]. Ong, S.-E.; Zhang, S.; Du, H.; Sun, D. Relationship between bonding structure and mechanical properties of amorphous carbon containing silicon. *Diamond Relat. Mater.* **2007**, *16*, 1628-1635.

[64]. Xue, Y.; Wu, B.; Jiang, L.; Guo, Y.; Huang, L.; Chen, J.; Tan, J.; Geng, D.; Luo, B.; Hu, W. Low temperature growth of highly nitrogen-doped single crystal graphene arrays by chemical vapor deposition. *J. Am. Chem. Soc.* **2012**, *134*, 11060-11063.

[65]. Zhang, J.; Li, J.; Wang, Z.; Wang, X.; Feng, W.; Zheng, W.; Cao, W.; Hu, P. Low-temperature growth of large-area heteroatom-doped graphene film. *Chem. Mater.* **2014**, *26*, 2460-2466.

[66]. Ferrari, A. C.; Basko, D. M. Raman spectroscopy as a versatile tool for studying the properties of graphene. *Nature Nanotech.* **2013**, *8*, 235-246.

[67]. Venezuela, P.; Lazzeri, M.; Mauri, F. Theory of double-resonant Raman spectra in graphene: intensity and line shape of defect-induced and two-phonon bands. *Phys. Rev. B.* **2011**, *84*, 035433.

[68]. Basko, D.; Piscanec, S.; Ferrari, A. Electron-electron interactions and doping dependence of the two-phonon Raman intensity in graphene. *Phys. Rev. B.* **2009**, *80*, 165413.

[69]. Zafar, Z.; Ni, Z. H.; Wu, X.; Shi, Z. X.; Nan, H. Y.; Bai, J.; Sun, L. T. Evolution of Raman spectra in nitrogen doped graphene. *Carbon* **2013**, *61*, 57-62.

[70]. Ferrari, A. C. Raman spectroscopy of graphene and graphite: disorder, electron-phonon coupling, doping and nonadiabatic effects. *Solid State Commun.* **2007**, *143*, 47-57.

[71]. Eckmann, A.; Felten, A.; Mishchenko, A.; Britnell, L.; Krupke, R.; Novoselov, K. S.; Casiraghi, C. Probing the nature of defects in graphene by Raman spectroscopy. *Nano Lett.* **2012**, *12*, 3925-3930.

[72]. Wang, Z.; Chen, Y.; Li, P.; He, J.; Zhang, W.; Guo, Z.; Li, Y.; Dong, M. Synthesis of silicon-doped reduced graphene oxide and its applications in dye-sensitive solar cells and supercapacitors. *RSC Adv.* **2016**, *6*, 15080-15086.

[73]. Lai, S.; Kyu Jang, S.; Jae Song, Y.; Lee, S. Probing graphene defects and estimating graphene quality with optical microscopy. *Appl. Phys. Lett.* **2014**, *104*, 043101.

[74]. Chen, S.; Moore, A. L.; Cai, W.; Suk, J. W.; An, J.; Mishra, C.; Amos, C.; Magnuson, C. W.; Kang, J.; Shi, L. Raman measurements of thermal transport in suspended monolayer graphene of variable sizes in vacuum and gaseous environments. *ACS Nano* **2010**, *5*, 321-328.

[75]. Sullivan, S.; Vallabhaneni, A.; Kholmanov, I.; Ruan, X.; Murthy, J.; Shi, L. Optical Generation and Detection of Local Nonequilibrium Phonons in Suspended Graphene. *Nano Lett.* **2017**, *17*, 2049-2056.

[76]. Vallabhaneni, A. K.; Singh, D.; Bao, H.; Murthy, J.; Ruan, X. Reliability of Raman measurements of thermal conductivity of single-layer graphene due to selective electron-phonon coupling: A first-principles study. *Phys. Rev. B.* **2016**, *93*, 125432.

[77]. Nair, R. R.; Blake, P.; Grigorenko, A. N.; Novoselov, K. S.; Booth, T. J.; Stauber, T.; Peres, N. M.; Geim, A. K. Fine structure constant defines visual transparency of graphene. *Science* **2008**, *320*, 1308-1308.

[78]. Crowther, A. C.; Ghassaei, A.; Jung, N.; Brus, L. E. Strong charge-transfer doping of 1 to 10 layer graphene by NO₂. *ACS Nano* **2012**, *6*, 1865-1875.

- [79]. Santoso, I.; Singh, R. S.; Gogoi, P. K.; Asmara, T. C.; Wei, D.; Chen, W.; Wee, A. T.; Pereira, V. M.; Rusydi, A. Tunable optical absorption and interactions in graphene via oxygen plasma. *Phys. Rev. B.* **2014**, *89*, 075134.
- [80]. Gao, L.; Lemarchand, F.; Lequime, M. Refractive index determination of SiO₂ layer in the UV/Vis/NIR range: spectrophotometric reverse engineering on single and bi-layer designs. *J. Europ. Opt. Soc. Rap. Public.* **2013**, *8*, 13010.
- [81]. Judek, J.; Gertych, A. P.; Świniarski, M.; Łapińska, A.; Dużyńska, A.; Zdrojek, M. High accuracy determination of the thermal properties of supported 2D materials. *Sci. Rep.* **2015**, *5*.
- [82]. Bergman, T. L. *Introduction to heat transfer*, John Wiley & Sons, **2011**.
- [83]. Persson, B.; Ueba, H. Heat transfer between graphene and amorphous SiO₂. *J. Phys.: Condens. Matter* **2010**, *22*, 462201.
- [84]. Ager, J. W.; Haller, E. E. Isotopically engineered semiconductors: from the bulk to nanostructures. *physica status solidi (a)* **2006**, *203*, 3550-3558.
- [85]. Adamyan, V.; Zavalniuk, V. Lattice thermal conductivity of graphene with conventionally isotopic defects. *J. Phys.: Condens. Matter* **2012**, *24*, 415401.
- [86]. Bae, M.-H.; Li, Z.; Aksamija, Z.; Martin, P. N.; Xiong, F.; Ong, Z.-Y.; Knezevic, I.; Pop, E. Ballistic to diffusive crossover of heat flow in graphene

ribbons. *Nat. Commun.* **2013**, *4*, 1734.

[87]. Lindsay, L.; Broido, D.; Mingo, N. Flexural phonons and thermal transport in graphene. *Phys. Rev. B.* **2010**, *82*, 115427.

[88]. Alam, H.; Ramakrishna, S. A review on the enhancement of figure of merit from bulk to nano-thermoelectric materials. *Nano Energy* **2013**, *2*, 190-212.

[89]. Philippe, D.; Viet Hung, N.; Jérôme, S.-M. Thermoelectric effects in graphene nanostructures. *J. Phys.: Condens. Matter* **2015**, *27*, 133204.

[90]. Mazzamuto, F.; Hung Nguyen, V.; Apertet, Y.; Caër, C.; Chassat, C.; Saint-Martin, J.; Dollfus, P. Enhanced thermoelectric properties in graphene nanoribbons by resonant tunneling of electrons. *Phys. Rev. B.* **2011**, *83*, 235426.

[91]. Zhao, W.; Guo, Z. X.; Cao, J. X.; Ding, J. W. Enhanced thermoelectric properties of armchair graphene nanoribbons with defects and magnetic field. *AIP Advances* **2011**, *1*, 042135.

[92]. Tran, V.-T.; Saint-Martin, J.; Dollfus, P.; Volz, S. Optimizing the thermoelectric performance of graphene nano-ribbons without degrading the electronic properties. *Sci. Rep.* **2017**, *7*, 2313.

[93]. Lu, Y.-F.; Lo, S.-T.; Lin, J.-C.; Zhang, W.; Lu, J.-Y.; Liu, F.-H.; Tseng, C.-M.; Lee, Y.-H.; Liang, C.-T.; Li, L.-J. Nitrogen-Doped Graphene Sheets

Grown by Chemical Vapor Deposition: Synthesis and Influence of Nitrogen Impurities on Carrier Transport. *ACS Nano* **2013**, *7*, 6522-6532.

[94]. Li, J.; Lin, L.; Rui, D.; Li, Q.; Zhang, J.; Kang, N.; Zhang, Y.; Peng, H.; Liu, Z.; Xu, H. Q. Electron–Hole Symmetry Breaking in Charge Transport in Nitrogen-Doped Graphene. *ACS Nano* **2017**, *11*, 4641-4650.

[95]. Chen, J.-H.; Cullen, W. G.; Jang, C.; Fuhrer, M. S.; Williams, E. D. Defect Scattering in Graphene. *Phys. Rev. Lett.* **2009**, *102*, 236805.

[96]. Wang, H.; Zhou, Y.; Wu, D.; Liao, L.; Zhao, S.; Peng, H.; Liu, Z. Synthesis of Boron-Doped Graphene Monolayers Using the Sole Solid Feedstock by Chemical Vapor Deposition. *Small* **2013**, *9*, 1316-1320.

[97]. Wang, Z.; Li, P.; Chen, Y.; Liu, J.; Tian, H.; Zhou, J.; Zhang, W.; Li, Y. Synthesis of nitrogen-doped graphene by chemical vapour deposition using melamine as the sole solid source of carbon and nitrogen. *J. Mater. Chem. C* **2014**, *2*, 7396-7401.

[98]. Gibbs, Z. M.; Kim, H.-S.; Wang, H.; Snyder, G. J. Band gap estimation from temperature dependent Seebeck measurement—Deviations from the $2e|S|_{\max}T_{\max}$ relation. *Appl. Phys. Lett.* **2015**, *106*, 022112.

[99]. Xiao, N.; Dong, X.; Song, L.; Liu, D.; Tay, Y.; Wu, S.; Li, L.-J.; Zhao, Y.; Yu, T.; Zhang, H. Enhanced thermopower of graphene films with oxygen plasma treatment. *Acs Nano* **2011**, *5*, 2749-2755.

실리콘 치환 도핑이 그래핀의 열물성에 미치는 영향

서울대학교 대학원
기계항공공학부
기계공학전공
이 우 림

초 록

원자 한층 두께의 그래핀은 열전도도가 $k = 2000 \sim 5000 \text{ W/mK}$ 으로 매우 높지만 격자 내의 결함으로 인해 상당히 감소되는 것으로 알려져 있다. 여러 종류의 결함 중에서, 치환 도핑되는 결함은 평면 방향으로의 열전도도를 효과적으로 낮추지만, 그래핀의 특별한 육각형 구조를 잘 유지할 수 있어 광학적 투명성과 같은 그래핀의 다른 우수한 성질들을 유지할 수 있는 가능성이 있다. 이차 섭동 이론(second-order perturbation theory)에 따르면, 치환 도핑되는 원소로 인한 포논 산란율은 일반적으로 치환 도핑되는

원소와 그래핀의 탄소 ($M = 12$) 원자 사이의 원자량 차이의 제공에 비례하는 것으로 알려져 있다. 하지만 기존의 치환 도핑 그래핀 관련 연구들은 탄소와의 원자량 차이가 작은 질소 (N), 보론 (B), 또는 탄소 동위원소 (^{13}C) 등으로 인한 열전도도 감소를 이론적으로만 연구하였다. 치환 도핑되는 원소가 탄소와의 원자량 차이가 매우 크다면, 그래핀의 열물성을 보다 효과적으로 조절할 수 있으며, 10배 이상의 열전도도 감소를 나타낼 가능성도 있다.

이러한 내용에 근거하여, 본 연구에서는 실리콘 치환 도핑으로 인한 그래핀의 열물성 변화에 초점을 맞추고 있으며, 이는 기존의 연구에 비해 탄소와의 원자량 차이가 가장 큰 치환 도핑 원소이다. 본 연구에서는 MTMS와 Hexane의 액체 전구체를 바탕으로 저압 화학 증기 증착법을 이용하여 실리콘 치환 도핑 그래핀을 합성하였다. 저압 증기 증착법은 탄소 내부의 격자 결함을 최소화하여 실리콘 원자의 효과를 보다 정확히 관측할 수 있도록 한다. 또한 합성 온도와 압력을 조절하여 실리콘 치환 도핑 농도 ($\sim I(D)/I(G)$)를 조절하였으며, 이를 바탕으로 치환 도핑 농도에 따른 열물성 변화를 계측하였다.

열물성 계측을 위해 합성된 실리콘 치환 도핑 그래핀을 8

나노미터 두께의 이산화규소 기판 위에 전사하였으며, 광열 라만 기법을 통해 열전도도를 측정하였다. 실리콘 치환 도핑 농도가 1.41 % 에서 3.13 %로 변하는 범위에서, 순수 그래핀의 열전도도 $k = 645.6 \sim 900.2 \text{ W/m}\cdot\text{K}$ 에 비해 자리수가 하나 감소된 $k_{SiG} = 46.7 \sim 79.5 \text{ W/m}\cdot\text{K}$ 의 값을 나타내었다. 이 값은 매달린 상태의 순수 그래핀의 열전도도 $k = 2662.5 \text{ W/m}\cdot\text{K}$ 에 비해 자리수가 2개 감소되는 결과이다. 관측된 열전도도 감소는 치환 도핑된 실리콘 원자와 탄소 원자 사이의 큰 원자량 차이로 인해 매우 높은 포논 산란을 때문인 것으로 이해할 수 있다. 또한 진공상태에서의 열처리된 그래핀과 기판 사이의 거리를 보다 짧게 하고, 기판으로 인한 포논 산란을 증가시키기 때문에 열전도도 값을 더 감소시킨다는 사실을 실험적으로 확인하였다. 또 다른 열적 특성인 열전도도의 온도 의존성과 포논간의 열적 비평형 상태가 실리콘 치환 도핑으로 인한 포논 산란을 증가와 기판의 효과로 인해 감소될 수 있음을 실험적으로 확인하였다.

마지막으로 측정된 열전도도 감소에 비해 실리콘 치환 도핑 농도로 인한 전기전도도 감소는 미비함을 확인하였다. 측정 결과, 2.6% 실리콘 치환 도핑의 경우 열전도도가 전기전도도에 비해

최대 8배 가량 더 감소하는 것을 확인하였다. 이는 실리콘 원자와 탄소 원자가 서로 최외각 전자 수가 같은 14족 원소에 속하기 때문인 것으로 추측된다. 따라서 무거운 실리콘 원자를 그래핀에 치환도핑하는 방법은 그래핀의 열전도도를 효과적으로 저감시키고, 열전 효율을 향상시킬 수 있는 가능성이 있다.

주요어 : 그래핀, 지지된 그래핀, 도핑된 그래핀, 실리콘 치환 도핑 그래핀, 열전도도, 광열라만기법, 전기전도도, 전자이동성, 열전 효율

학번 : 2016-33514